HISTIDINE FOLDING SWITCH IN EFFECTOR PROTEIN AVRPTO REGULATES ITS TRANSPORT THROUGH THE BACTERIAL TYPE III SECRETION SYSTEM, AS DETERMINED BY NMR, FLUORESCENCE, CIRCULAR DICHROISM SPECTROSCOPIES AND TRANSLOCATION ASSAYS

A Dissertation

Presented to the Faculty of the Graduate School

of Cornell University

In Partial Fulfillment of the Requirements for the Degree of

Doctor of Philosophy

by

Jolita Seckute

January 2011

HISTIDINE FOLDING SWITCH IN EFFECTOR PROTEIN AVRPTO REGULATES ITS TRANSPORT THROUGH THE BACTERIAL TYPE III SECRETION SYSTEM, AS DETERMINED BY NMR, FLUORESCENCE, CIRCULAR DICHROISM SPECTROSCOPIES AND TRANSLOCATION ASSAYS

Jolita Seckute, Ph. D.

Cornell University 2011

Bacteria have evolved several secretion systems as direct conduits into host cell cytoplasm for bacterial effector protein trafficking to further their symbiotic or pathogenic goals, while avoiding detection and host immune responses. Gram-negative bacterium *Pseudomonas syringae* uses the type III secretion system that spans bacterial membranes and extends with a needle-like protrusion to open up through the host cell membrane. There are structural constraints to passage through this conduit, where the inner channel diameter of 2–3 nm prevents effector protein export in the folded form. The requirement for transient unfolding places unique restrictions on the stability thresholds for effector structure and function, essential for bacterial pathogenicity. Effector tertiary structure is typically needed for function in the host, as has been shown for one of the most widely studied effectors, AvrPto.

AvrPto is an 18-kDa protein with a helical core of low stability and disordered N- and C-termini, secreted by the plant pathogen *Pseudomonas syringae*. AvrPto features a single amino acid folding switch governed by histidine 87 that acts in the moderately acidic pH range expected in the

biological environment of the bacterium. At neutral plant host cytosol of pH ~7.4 AvrPto is predominantly in the folded form. We disabled the His 87-encoded pH switch by the H87Y mutation and observed a slight increase in stability and a dramatic shift in the acid denaturation into the more acidic pH. This mutation significantly affected the translocation efficiency of AvrPto during the initial hours of *Pseudomonas syringae* infection at different temperatures.

Through direct comparison of *in vivo* data with *in vitro* AvrPto stability trends we conclude that the amount of available cytoplasmic unfolded AvrPto is a factor regulating AvrPto translocation, and favors an acidic bacterial cytosol. Preliminary ratiometric GFP fluorescence data predicts bacterial intracellular pH of < 6, in agreement with this prediction. Taken together, a mechanism for effector transport emerges that depends on destabilized effector pools for the T3SS as a significant factor in effector translocation hierarchy and the overall infection process.

BIOGRAPHICAL SKETCH

Jolita is originally from Netoniai, Lietuva. She graduated from high school in 2000 at the Kaunas University of Technology Gymnasium (KTUG) in Kaunas, Lithuania and continued at Truman State University (Kirksville, MO) where she received her B.S. in Chemistry. Then she came to Cornell to study macromolecular structure of enzymes by x-ray crystallography in Steven E. Ealick's lab in the Department of Chemistry and Chemical Biology. After the Master's degree she completed her Ph.D. while investigating the mechanism of folding of a model bacterial protein involved in pathogenesis.

ACKNOWLEDGMENTS

I am thankful for the opportunity to have studied with the guidance of many direct research advisors. My undergraduate research experience started with Eric Patterson at Truman State University in computational chemistry, and continued through summer research grants and projects with Paul Hergenrother at the University of Illinois at Urbana–Champaign in organic chemistry synthesis, and Steve Granick at UIUC in materials science. In my graduate career I had the opportunity to learn X-ray crystallography alongside Steve Ealick and an exceptional group of students, and later I explored the field of biophysics under the supervision of Linda Nicholson in her lab.

This work was supported by NSF grant MCB-0641582.

TABLE OF CONTENTS

LIST OF FIGURES

LIST OF TABLES

CHAPTER 1
INTRODUCTION

Bacterial pathogens employ secretion systems for host invasion

Bacteria-host interactions have coevolved repeatedly in the course of evolution. Bacterial habitat expansion into an intracellular and extracellular spaces of multicellular organisms in the plant and animal kingdom provided a significant environmental niche and resulted in the emergence of pathogens and symbionts (Corsaro et al., 1999). Bacteria may even be viewed as catalysts of eukaryotic evolution, since they are generally genetically more diverse and confer new metabolic traits or elaborate defense mechanisms on their hosts (Steinert et al., 2000). As pathogens and hosts coevolve, in cases where the pathogen maintains its virulence the host is forced to react by investing heavily in its defense and pathogen recognition. In this evolutionary arms race, bacteria have achieved extraordinary engineering feats in their secretion pathways that interact with their environment in a way beneficial to the pathogen while ensuring their survival within the host.

While all bacteria are capable of protein transport through their membranes, some developed specialized ways of interacting through direct extracellular contact with the host and trafficking their proteins directly into the neighboring target cell (Nickerson and Schurr, 2006). Ever since the initial discoveries of the bacterial secretion systems in 1980s (Felmlee et al., 1985; Salmond and Reeves, 1993), there has been a continued interest in understanding the critical importance of bacterial-host mutualistic or pathogenic interactions (Büttner and Bonas, 2006; Dale et al., 2002; Deakin and

Broughton, 2009; Marchetti et al., 2010). Symbiotic survival and proliferation of rhizobia in plant roots is aided by a bacterial secretion system (type III secretion system, T3SS) that blocks innate plant defenses and ensures bacterial survival (Bartsev et al., 2004). A recently discovered endosymbiont *Sodalis glossinidius* that contains T3SS invasion genes does not seem to confer benefit or significant harm to the host tsetse fly, *Glossina* spp. (Dale et al., 2001). On the other end of the spectrum, various Gram-negative bacteria pathogenic to humans, other animals, and plants employ secretion systems in order to disarm the host defenses and usurp the invaded cell to facilitate bacterial nutrition for persistence and proliferation (Abramovitch et al., 2006).

Out of the seven known Gram-negative bacterial secretion systems to-date, that provide routes for protein passage across an entire cell envelope, there are 4 types that assemble surface structures, proceed through direct host cellular contact, and share structural similarities: type III (depicted in Chapter 2), IV, V and VI secretion systems (Hayes et al., 2010). The least complex T5SS depends on the general secretory pathway (Sec) to deliver autotransporter proteins through the inner membrane into the periplasm. Autotransporters then catalyze their export through the outer membrane via the T5SS by self-catalysis. In the target contact-dependent scenario, host growth inhibition is achieved by *Escherichia coli* using T5SS to export a β-barrel protein CdiA to the cell surface where it extends into the extracellular space and contacts the host membrane receptor BamA initiating signal transfer that results in target growth inhibition (Hayes et al., 2010).

A more aggressive T6SS is similar to bacteriophage DNA injection mechanism. T6SS base is assembled through the inner membrane and anchors a tube-like structure that protrudes through the outer membrane and

essentially impales the host by inserting through the plasma membrane to allow effector protein delivery into the host cytoplasm in an ATP-dependent manner. Similarly, a T4SS is used by pathogenic bacteria to deliver effectors into the eukaryotic host cells. T4SS features cell surface adhesins that are responsible for cell-cell contact, a secretion channel through the bacterial and host membranes, and a coupling protein that is the substrate receptor at the channel entrance (Hayes et al., 2010).

The focus of this work is effector transport through the T3S, a Sec-independent system that is related to the flagellum in its syringe-like structure and a requirement for specific ATPase activity and proton motive force (PMF) for assembly and effector delivery (Desvaux et al., 2006). T3SS is widely employed by Gram-negative plant (Büttner and He, 2009) and animal (Sherman et al., 2010) pathogens and features a conserved structure and diverse arrays of translocated effectors (Ghosh, 2004). This supramolecular assembly proceeds in a stepwise manner, where the inner membrane ring with an associated ATPase and the outer membrane ring are assembled separately, then joined together to form a cylindrical basal body that anchors the subsequent assembly of the needle substructure (Galán and Wolf-Watz, 2006). Once the needle, also termed the pilus, extends through several nanometers and touches the host membrane, another conformational switch recruits the translocon pore proteins, which complete the assembly by inserting through the host's plasma membrane and establishing the connection between the two cells. The final switch in T3SS substrate recognition makes it competent for effector secretion (Büttner and Bonas, 2006).

Pseudomonas syringae effector AvrPto has virulence and avirulence roles in the plant host

Pseudomonas syringae is a fluorescent pseudomonad that belongs to a large and diverse family of Gram-negative bacteria (Rehm, 2008). Its pathovars are pathogenic to several plant species and rely on the expression of the T3SS for pathogenesis (Büttner and He, 2009; Rudolph et al., 1997) *P. syringae* pv tomato DC3000 (*Pst*) causes bacterial speck disease in susceptible tomato and *Arabidopsis* plants (Rehm, 2008). *Pst* pathogenesis is initiated by the delivery of up to 30 known effector proteins into the host plant cell (Alfano and Collmer; Cunnac et al., 2009). Since several *Pst* effectors were discovered by their avirulence roles in resistant host or non-host plants, they were annotated as *avr* genes (Ronald et al., 1992).

An example *Pst* effector, AvrPto, has been studied as a model protein with previously solved apo and complex structures (Wulf et al., 2004; Xing et al., 2007). AvrPto adopts a low-stability ($\Delta G_{F\rightarrow U} = 4.3 \pm 0.5$ at pD 7.2, Chapter 3) structured core of three amphipathic α-helices with a centrally buried aromatic Tyr69–Trp116–Tyr73 cluster, where the aromatic planes are positioned at ~70–80° (Figure 1.1). Tyrosines are separated in sequence by 3 residues along α-helix 3 and their hydroxyls are not involved in π-OH interactions, but Tyr 69 hydroxyl group is solvent-exposed, and Tyr 73 weakly hydrogen-bonds to Ala 47 mainchain that ends α-helix 1. An edge-to-face aromatic ring arrangement in AvrPto is strongly preferred in Trp-Tyr sidechain interactions, where the Tyr face is positioned against the Trp edge (Samanta et al., 1999). Since an aromatic Tyr sidechain pair that is partially or completely buried is expected to contribute 0.6–1.3 kcal/mol in stability

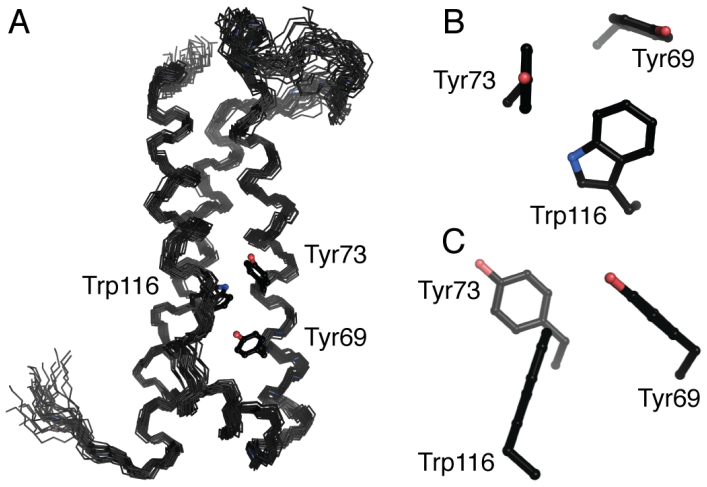

Figure 1.1. *Pst* effector AvrPto structure. (A) Truncated AvrPto structure comprised of residues 29–133, with disordered N- and C-termini removed. Structure was solved by NMR (PDB ID 1R5E), and all states are shown. Tyr 69, Tyr 73, and Trp 116 in the hydrophobic core are indicated with carbon atoms in black, oxygens in red and nitrogens in blue. (B) and (C) show relative ring positions in the aromatic cluster to be in the preferred edge-to-face configuration.

(Burley and Petsko, 1985), this network provides significant energy stabilization to the tertiary structure.

Upon delivery into the host cell, AvrPto is post-translationally modified for its virulence role. AvrPto is phosphorylated at multiple sites, and the N-terminal domain is myristoylated for membrane-targeting. Phosphorylation occurs at the disordered C-terminus (Yeam et al., 2010). Host kinase-mediated phosphorylation contributes independently to AvrPto virulence, thus acting on different virulence functions. Myristoylated AvrPto localizes at the host plasma membrane (Shan et al., 2000), where the effector interacts with the surface-localized pattern-recognition receptor (PRR) kinase FLS2 (Xiang et al., 2010), through binding at the omega loop. This way an initial plant detection of the neighboring pathogen-associated molecular patterns (PAMPs) is compromised at the PAMP-triggered immunity (PTI) level.

A more specific layer of plant defense is effector-triggered immunity (ETI) that depends on host resistance (R) protein-bacterial effector recognition and binding. In resistant plant species, N-myristoylated AvrPto is recognized by a decoy kinase Pto that recognizes the omega loop and binds AvrPto (Xing et al., 2007). AvrPto-Pto binding event alters Pto's co-regulatory interaction with the associated host R protein Prf (Salmeron et al., 1996). Activated Prf initiates a downstream signaling cascade resulting in the hypersensitive response (HR), a localized host cell death, as a response to *Pst* invasion (Mucyn et al., 2006).

Intriguingly, AvrPto sequence that just precedes the C-terminal domain at positions 146–164 with known phosphorylation sites, features a PPSP motif at 134–137. Since the structured region ends with an α-helix 4 and the unstructured sequence begins at histidine 130, the PPSP sequence may have

C-terminal domain specific functions. C-terminal PxxP motif is implicated in the activity of the pituitary tumor transforming gene (PTTG) that carries a PPSP sequence in its C-terminus, the transcriptional activating domain (Wang and Melmed, 2000). Transcriptional activating domains typically feature C-termini enriched in prolines and/or glutamates, and while AvrPto does not share the Glu enrichment, the 134–164 residue region with 6 Pro is 20% Pro, while the remainder 1–133 region with 5 Pro residues is at 3.8%, close to the overall average in proteins in nature of ~5% (Creighton, 1993). AvrPto functions that may make use of this sequence motif are not known, but this suggests a possibly more diverse involvement of AvrPto in the *Pst* pathogenesis during target cell takeover and altering of the host secreted metabolite pool (Kaffarnik et al., 2009).

AvrPto export through the T3SS channel enforces effector transient unfolding

An important aspect in the effector function is the ability to pass through a 2–3 nm diameter channel along the extended T3SS structure of variable length (Hoiczyk and Blobel, 2001). During this step, effectors must be at least partially unfolded (Feldman et al., 2002). Some effectors depend on the action of known specific bacterial chaperones that function to target their cargo for T3SS export by interacting with the T3SS ATPase, keep bound effectors in the unfolded state, and protect from degradation by proteases (Stebbins and Galán, 2001).

Since AvrPto does not have a known chaperone, the unfolding step for T3SS passage followed by refolding in the host cytoplasm requires specific

structural features encoded within the primary sequence and locked by the tertiary arrangement of the AvrPto structure itself. It is possible to engineer a transport-incapable structure with an attached N-terminal signal sequence targeting it for T3SS and clog the channel (Akeda and Galán, 2005), therefore, evolution has selected for effector structures that streamline the process of infection by the bacterial secretion systems.

Elucidating the mechanism of AvrPto adaptation to its varying environmental conditions as it passes between two cells in this dynamic interkingdom system will help in the general understanding of the effector transport regulation as well as factors determining transport timeline and efficiency requirements, and effector hierarchy among the pool of sequences being transported. While there are no known AvrPto homologs by sequence, scarce effector structural information prevents accurate estimates of how conserved their three-dimensional features may be.

The following chapters characterize AvrPto stability as a function of environmental signals like pH and temperature. AvrPto encodes a pH-sensing desolvated histidine residue (Chapter 2) that modulates AvrPto pH-sensitivity in the mildly acidic *in vitro* conditions. Next, the effect of the removal of this pH-sensor by a His-to-Tyr mutation is explored *in vitro* and *in vivo* by *Pst*-plant translocation assays (Chapter 3). A non-host domestic tobacco *Nicotiana tabacum* is used for *in planta* experiments. The advantage of this plant environment is the established use of tobacco as a model plant for infection and resistance studies (Goodin et al., 2008), its availability and relatively large leaves that enable large timescale AvrPto translocation experiments. Intracellular *Pst* acidification would benefit AvrPto unfolding and translocation, and a preliminary study to measure *Pst* cytosolic pH is

described (Chapter 4). We used a GFP variant that is ratiometric to pH by emission, called E^{1}GFP, that is derived from EGFP, is too stable to unfold for secretion and would remain in the cytoplasm (Akeda and Galán, 2005; Serresi et al., 2009). *Pst* intracellular pH was measured in the *N tabacum* apoplast by confocal microscopy and the initial data points to a pH of 5.4 ± 0.1. However, proper controls need to be established before this experiment can be finalized.

Acknowledgements

Work presented in the following chapters was made possible by access to instruments from several research groups at Cornell University. Circular dichroism spectrometer data was collected in Prof. Brian Crane's laboratory. A Varian Cary Eclipse spectrophotometer in Prof. Colin Parrish's laboratory was used in tryptophan fluorescence temperature denaturation and fluorescence scans. A fluorescence plate reader in the Protein Facility with Dr. Cynthia Kinsland's supervision was used to measure AvrPto equilibrium unfolding data. Zeiss confocal microscope access and training was provided by Carol Bayles at the Microscopy and Imaging Facility.

N. tabacum plants were provided by Prof. Alan Collmer's laboratory. Translocation assays were performed at the Gutterman Greenhouse Facility growth chambers. Collected plant samples were processed in Prof. Collmer's laboratory, OD at 595 nm checked by spectrophotometer (Molecular Devices) access at the Plant Science Building, and analyzed in Prof. Samuel Cartinhour's laboratory by using a Beckman Coultier LD 400 plate reader.

BIBLIOGRAPHY

Abramovitch, R.B., Anderson, J.C., and Martin, G.B. (2006). Bacterial elicitation and evasion of plant innate immunity. Nature Reviews Molecular Cell Biology *7*, 601-611.

Akeda, Y., and Galán, J.E. (2005). Chaperone release and unfolding of substrates in type III secretion. Nature *437*, 911-915.

Alfano, J.R., and Collmer, A. (2004). Type III secretion system effector proteins: double agents in bacterial disease and plant defense. Annu Rev Phytopathol *42*, 385-414.

Bartsev, A.V., Deakin, W.J., Boukli, N.M., McAlvin, C.B., Stacey, G., Malnoë, P., Broughton, W.J., and Staehelin, C. (2004). NopL, an effector protein of Rhizobium sp. NGR234, thwarts activation of plant defense reactions. Plant Physiol *134*, 871-879.

Burley, S.K., and Petsko, G.A. (1985). Aromatic-aromatic interaction: a mechanism of protein structure stabilization. Science *229*, 23-28.

Büttner, D., and Bonas, U. (2006). Who comes first? How plant pathogenic bacteria orchestrate type III secretion. Curr Opin Microbiol *9*, 193-200.

Büttner, D., and He, S.Y. (2009). Type III protein secretion in plant pathogenic bacteria. PLANT PHYSIOLOGY *150*, 1656-1664.

Corsaro, D., Venditti, D., Padula, M., and Valassina, M. (1999). Intracellular life. Crit Rev Microbiol *25*, 39-79.

Creighton, T.E. (1993). Proteins: Structure and Molecular Properties. W H Freeman and Co, New York.

Cunnac, S., Lindeberg, M., and Collmer, A. (2009). Pseudomonas syringae type III secretion system effectors: repertoires in search of functions. Curr Opin Microbiol *12*, 53-60.

Dale, C., Plague, G.R., Wang, B., Ochman, H., and Moran, N.A. (2002). Type III secretion systems and the evolution of mutualistic endosymbiosis. Proceedings of the National Academy of Sciences of the United States of America *99*, 12397-12402.

Dale, C., Young, S.A., Haydon, D.T., and Welburn, S.C. (2001). The insect endosymbiont Sodalis glossinidius utilizes a type III secretion system for cell invasion. Proceedings of the National Academy of Sciences of the United States of America *98*, 1883-1888.

Deakin, W.J., and Broughton, W.J. (2009). Symbiotic use of pathogenic strategies: rhizobial protein secretion systems. Nat Rev Microbiol *7*, 312-320.

Desvaux, M., Hébraud, M., Henderson, I.R., and Pallen, M.J. (2006). Type III secretion: what's in a name? Trends Microbiol *14*, 157-160.

Feldman, M.F., Müller, S., Wüest, E., and Cornelis, G.R. (2002). SycE allows secretion of YopE-DHFR hybrids by the Yersinia enterocolitica type III Ysc system. Molecular Microbiology *46*, 1183-1197.

Felmlee, T., Pellett, S., Lee, E.Y., and Welch, R.A. (1985). Escherichia coli hemolysin is released extracellularly without cleavage of a signal peptide. J Bacteriol *163*, 88-93.

Galán, J.E., and Wolf-Watz, H. (2006). Protein delivery into eukaryotic cells by type III secretion machines. Nature *444*, 567-573.

Ghosh, P. (2004). Process of protein transport by the type III secretion system. Microbiol Mol Biol Rev *68*, 771-795.

Goodin, M.M., Zaitlin, D., Naidu, R.A., and Lommel, S.A. (2008). Nicotiana benthamiana: its history and future as a model for plant-pathogen interactions. Molecular Plant-Microbe Interactions *21*, 1015-1026.

Hayes, C.S., Aoki, S.K., and Low, D.A. (2010). Bacterial contact-dependent delivery systems. Annu Rev Genet *44*, 71-90.

Hoiczyk, E., and Blobel, G. (2001). Polymerization of a single protein of the pathogen Yersinia enterocolitica into needles punctures eukaryotic cells. Proceedings of the National Academy of Sciences of the United States of America *98*, 4669-4674.

Kaffarnik, F.A.R., Jones, A.M.E., Rathjen, J.P., and Peck, S.C. (2009). Effector proteins of the bacterial pathogen Pseudomonas syringae alter the extracellular proteome of the host plant, Arabidopsis thaliana. Mol Cell Proteomics *8*, 145-156.

Marchetti, M., Capela, D., Glew, M., Cruveiller, S., Chane-Woon-Ming, B., Gris, C., Timmers, T., Poinsot, V., Gilbert, L.B., Heeb, P., *et al.* (2010). Experimental evolution of a plant pathogen into a legume symbiont. PLoS Biol *8*, e1000280.

Mucyn, T.S., Clemente, A., Andriotis, V.M.E., Balmuth, A.L., Oldroyd, G.E.D., Staskawicz, B.J., and Rathjen, J.P. (2006). The tomato NBARC-LRR protein Prf interacts with Pto kinase in vivo to regulate specific plant immunity. The Plant Cell *18*, 2792-2806.

Nickerson, C., and Schurr, M. (2006). Molecular Paradigms of Infectious Disease. Springer, New York, NY.

Rehm, B. (2008). Pseudomonas: model organism, pathogen, cell factory. Wiley-VCH, Weinheim, Germany.

Ronald, P.C., Salmeron, J.M., Carland, F.M., and Staskawicz, B.J. (1992). The cloned avirulence gene avrPto induces disease resistance in tomato cultivars containing the Pto resistance gene. Journal of Bacteriology *174*, 1604-1611.

Rudolph, K., Burr, T.J., Mansfield, J.W., Stead, D., Vivian, A., and von Kietzell, J. (1997). Pseudomonas syringae pathovars and related pathogens. Kluwer Academic Publishers, Norwell, MA.

Salmeron, J.M., Oldroyd, G.E., Rommens, C.M., Scofield, S.R., Kim, H.S., Lavelle, D.T., Dahlbeck, D., and Staskawicz, B.J. (1996). Tomato Prf is a member of the leucine-rich repeat class of plant disease resistance genes and lies embedded within the Pto kinase gene cluster. Cell *86*, 123-133.

Salmond, G.P., and Reeves, P.J. (1993). Membrane traffic wardens and protein secretion in gram-negative bacteria. Trends Biochem Sci *18*, 7-12.

Samanta, U., Pal, D., and Chakrabarti, P. (1999). Packing of aromatic rings against tryptophan residues in proteins. Acta Crystallogr D Biol Crystallogr *55*, 1421-1427.

Serresi, M., Bizzarri, R., Cardarelli, F., and Beltram, F. (2009). Real-time measurement of endosomal acidification by a novel genetically encoded biosensor. Analytical and bioanalytical chemistry *393*, 1123-1133.

Shan, L., Thara, V.K., Martin, G.B., Zhou, J.M., and Tang, X. (2000). The pseudomonas AvrPto protein is differentially recognized by tomato and tobacco and is localized to the plant plasma membrane. The Plant Cell *12*, 2323-2338.

Sherman, P.M., Ossa, J.C., and Wine, E. (2010). Bacterial infections: new and emerging enteric pathogens. Curr Opin Gastroenterol *26*, 1-4.

Stebbins, C.E., and Galán, J.E. (2001). Maintenance of an unfolded polypeptide by a cognate chaperone in bacterial type III secretion. Nature *414*, 77-81.

Steinert, M., Hentschel, U., and Hacker, J. (2000). Symbiosis and pathogenesis: evolution of the microbe-host interaction. Naturwissenschaften *87*, 1-11.

Wang, Z., and Melmed, S. (2000). Pituitary tumor transforming gene (PTTG) transforming and transactivation activity. J Biol Chem *275*, 7459-7461.

Wulf, J., Pascuzzi, P.E., Fahmy, A., Martin, G.B., and Nicholson, L.K. (2004). The solution structure of type III effector protein AvrPto reveals conformational and dynamic features important for plant pathogenesis. Structure *12*, 1257-1268.

Xiang, T., Zong, N., Zhang, J., Chen, J., Chen, M., and Zhou, J. (2010). FLS2, but not BAK1, is a target of the Pseudomonas syringae effector AvrPto. Molecular plant-microbe interactions.

Xing, W., Zou, Y., Liu, Q., Liu, J., Luo, X., Huang, Q., Chen, S., Zhu, L., Bi, R., Hao, Q., *et al.* (2007). The structural basis for activation of plant immunity by bacterial effector protein AvrPto. Nature *449*, 243-247.

Yeam, I., Nguyen, H.P., and Martin, G.B. (2010). Phosphorylation of the Pseudomonas syringae effector AvrPto is required for FLS2/BAK1-independent virulence activity and recognition by tobacco. Plant J *61*, 16-24.

CHAPTER 2

ELUCIDATION OF A PH-REGULATED HISTIDINE FOLDING SWITCH IN THE *PSEUDOMONAS SYRINGAE* EFFECTOR PROTEIN AVRPTO[*]

Introduction

Gram-negative bacteria have evolved supramolecular type III secretion machinery that joins the bacterial and host cytoplasms through a nanosyringe-like assembly anchored by the basal body spanning the bacterial membranes and the tip complex incorporated in the host cell wall (Alfano and Collmer, 2004). This complex is tuned for regulated assembly upon host cell contact, followed by injection of targeted bacterial proteins (effectors) into the host cell for specific virulence functions (Figure 2.1A illustration). Typically, effectors function in the host cell to (i) subvert host basal and pathogen-specific defenses, (ii) change gene expression profiles, and (iii) target host proteins and modify their cellular functions (Grant et al., 2006). One well-studied model pathogen, *Pseudomonas syringae*, employs type III secretion system (T3SS) with an arsenal of about 30 effectors to exploit plant cells for nutrient access. Understanding *P. syringae* pathogenicity important in crop disease resistance studies (Abramovitch et al., 2006), as well as within the broader context of functional adaptation in the race of the invading bacterium and the defending host organisms.

---

[*] Dawson, J.E.[1]; Šečkutė, J.[1]; De, S.; Schueler, S. A.; Oswald, A. B.; Nicholson, L. K. Elucidation of a pH-folding switch in the Pseudomonas syringae effector protein AvrPto. Proc Natl Acad Sci USA (2009) vol. 106 (21) pp. 8543-8.
[1] Equal-contribution authors

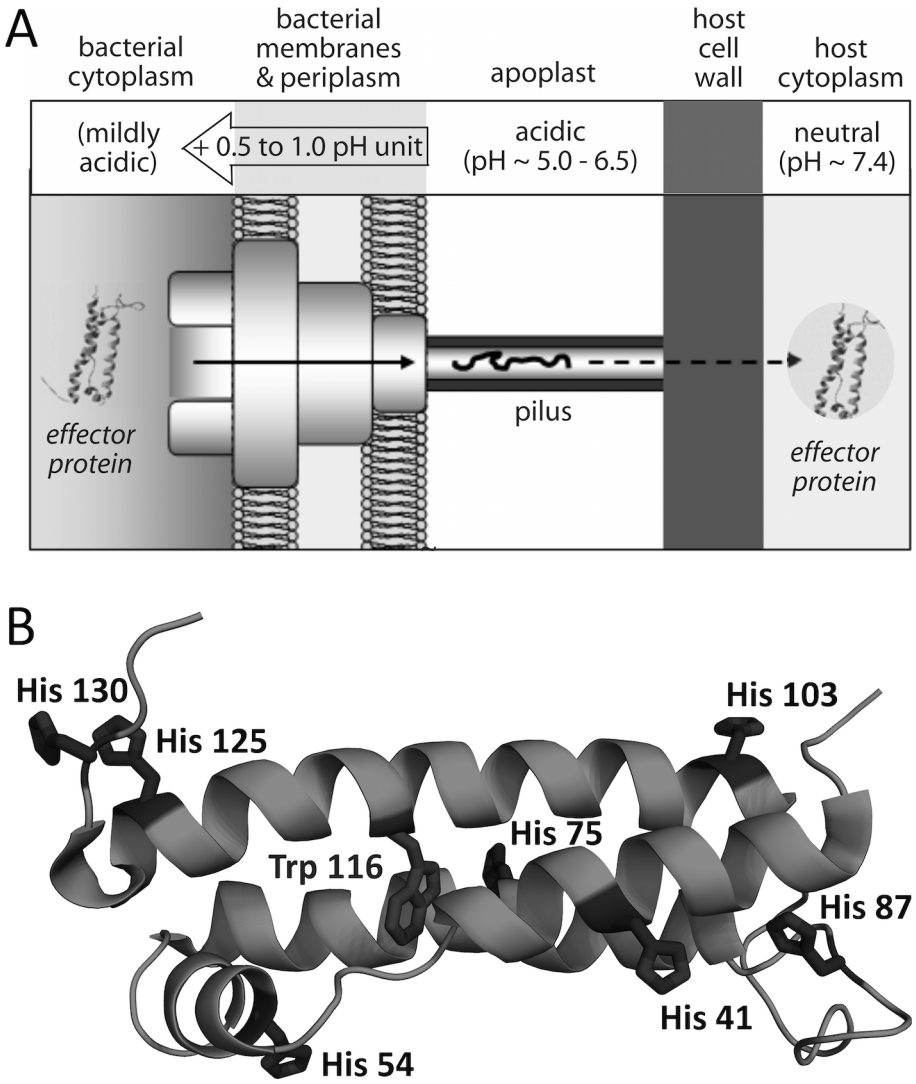

Figure 2.1. *P. syringae* effectors are predicted to be exposed to a range of environmental pH and to be functionally adapted to such variation. (A) T3SS assembly spans both bacterial membranes, protrudes into the extracellular space by the syringe-like extension, the pilus, and incorporates into the host cell membrane to open up for effector delivery into the host cytoplasm. (B) Helical TrAvrPto structural core incorporates seven His residues whose individual pKa values were determined by NMR, and a central buried Trp 116 that enabled unfolding studies by tryptophan fluorescence.

When faced with adapted bacterial invaders, plant hosts have coevolved two levels of pathogen resistance. First, the basal response is elicited by the pathogen-associated molecular pattern (PAMP)-triggered immunity (PTI) at the cell wall (Hématy et al., 2009). Second, specific effector-triggered immunity (ETI) is dependent on the direct detection of effector proteins inside the host cell by gene-for-gene interactions with host resistance (R) genes (Zhang et al., 2010). Many bacterial virulence genes were discovered by their ability to trigger the ETI defense and were classified avirulence (Avr) genes (Keen, 1990). ETI results in the production of reactive oxygen species, induction of defense genes and localized cell death as a hypersensitive response (HR) that functions to limit pathogen growth (Klement and Goodman, 1967). One example of such Avr effector recognition occurs in plants carrying decoy kinase Pto (Ronald et al., 1992) that directly binds to *P. syringae* effectors AvrPto and AvrPtoB, releasing the Pto-associated Prf protein that initiates a downstream signaling cascade resulting in HR (Salmeron et al., 1996).

AvrPto is a well-studied relatively small 164 amino acid 18.3 kDa effector with a known structure of a central 3-helix bundle with an additional 6-residue orthogonal helix, an omega loop of 20 residues, and disordered termini (Wulf et al., 2004; Xing et al., 2007). AvrPto is delivered into the host cell in a T3SS-dependent manner (van Dijk et al., 1999) that requires effector unfolding to pass through its needle-like extension (pilus) of an inner diameter of 2-3 nm (Figure 2.1B) (Daniell et al., 2003; Hoiczyk and Blobel, 2001). AvrPto virulence function upon delivery is membrane kinase binding and prevention of PTI. In the host cell AvrPto is posttranslationally modified by multi-phosphorylation (Yeam et al., 2010) and N-terminal myristoylation

(Shan et al., 2000b) that targets it to the plasma membrane. AvrPto is known to directly bind to FLS2, thus preventing its association with BAK1 kinase upon recognition of bacterial flagellar peptide flg22, and preventing downstream PTI responses (Xiang et al., 2010). AvrPto recognition for virulence and avirulence functions are separate, as shown by point mutations in the omega loop (a.a. 84-102) that impede AvrPto avirulence without affecting its virulence function (Shan et al., 2000a).

Here we report the structural requirements that enable a model effector AvrPto to function within the T3SS that requires effector unfolding for translocation into the host cell, while maintaining sufficient structured population before and after translocation in order to minimize unfavorable active degradation in the bacterial cell and to carry out its function by forming complexes with its binding partners in the host cell. We determined the mechanism of folding control in AvrPto that is governed by a pH-sensitive folding switch encoded in a single buried residue, histidine 87. Wildtype AvrPto unfolds at pH 6 and below, while the removal of this folding switch by a point mutation shifts the acid denaturation curve into a significantly more acidic pH ~3.5 range. We predict that this effector can sense pH changes in different cellular environments and respond with shifts in its folding/unfolding equilibrium. It remains to be determined if this mode of effector regulation may be applied to other translocated structures.

Results

Truncated AvrPto adopts a low stability helical structure in vitro. NMR, circular dichroism (CD) and tryptophan fluorescence (Fl) were used to

determine *in vitro* the acid denaturation curve of a truncated structured core of AvrPto (TrAvrPto, residues 29–133 encompassing α-helices 1–4) with disordered N- and C-termini removed. The solution structure of TrAvrPto was determined previously, and was shown to be unaffected by the termini truncations while allowing minimization of NMR spectral overlap (Wulf et al., 2004). Likewise, AvrPto-Pto complex structure, determined by x-ray crystallography, maintains the same AvrPto fold as the apo TrAvrPto structure, suggesting that substrate recognition and binding in the host cell do not result in altered AvrPto conformation (Xing et al., 2007). Therefore, we focused on TrAvrPto acid denaturation behavior as a function of pH as reported by the individual-residue folded (F) and unfolded (U) populations determined by NMR at the level of individual-residue amide signals, by the loss of secondary helical structure as determined by CD, and by the loss of centrally-buried tryptophan fluorescence signal with unfolding. Care was taken to maintain the citrate/phosphate buffer solution system at a constant ionic strength of 230 mM throughout the *in vitro* experiments (McIlvaine, 1921).

The two-dimensional ^{15}N-^{1}H fast-HSQC (fHSQC, heteronuclear single quantum coherence) NMR experiment gives rise to signal peaks in frequency space of amide groups of protein residues that are sensitive to the local residue environment. Two populations of peaks in slow exchange on the experimental timescale, corresponding to the folded and unfolded form of TrAvrPto, were measured for samples in the pH range 2.8–7.1. The presence of equilibrium F and U peaks for a representative residue Gly 95 backbone amide in the loop region of TrAvrPto is shown across all pH time points in Figure 2.2A. A total of 12 backbone amide F and U peaks were used for the

population-weighted average as the overall folded population value (p_F) at each pH: A47, G48, A61 (loop regions), S64, T76 (α-helix 3), T91, G92, S94, G95, G99 (loop), A112, and G128 (α-helix 4), as well as one W116 side chain indole group (α-helix 4). These 13 data points reflecting the unfolding equilibrium at various positions throughout the structure yielded average p_F values with small standard deviations, as shown in Figure 2.2B.

TrAvrPto acid denaturation behavior was further studied by thermal denaturation by Fl and CD that report on the unfolding event from independent perspectives of Trp unfolding and loss of helical content, respectively. While concentrated purified protein samples at 0.4-0.8 mM were used in the NMR experiments, for Fl and CD the concentration was lowered by up to 10-fold to 80 μM to be in the optimum range for such experiments and in order to account for any possible NMR result bias from aggregation at higher concentrations. WT TrAvrPto samples were buffer-exchanged into McIlvaine's buffer at pH in the range of 4-8 and were individually reversibly denatured by temperature (Figure 2.2C, reversibility not shown). Folded protein population values were calculated from the signal at the NMR experimental temperature of 26.6 °C (gray vertical line in Figure 2.2C) by taking the ratio of the linearly extrapolated fully folded and unfolded signal levels to that temperature. In both Fl and CD experimental setups the samples were measured in small temperature increments assuming full equilibration at each point. Representative data agreement between Fl and CD is shown for sample pH points from pH 4.0 to 8.0 with calculated p_F values plotted in Figure 2.2C.

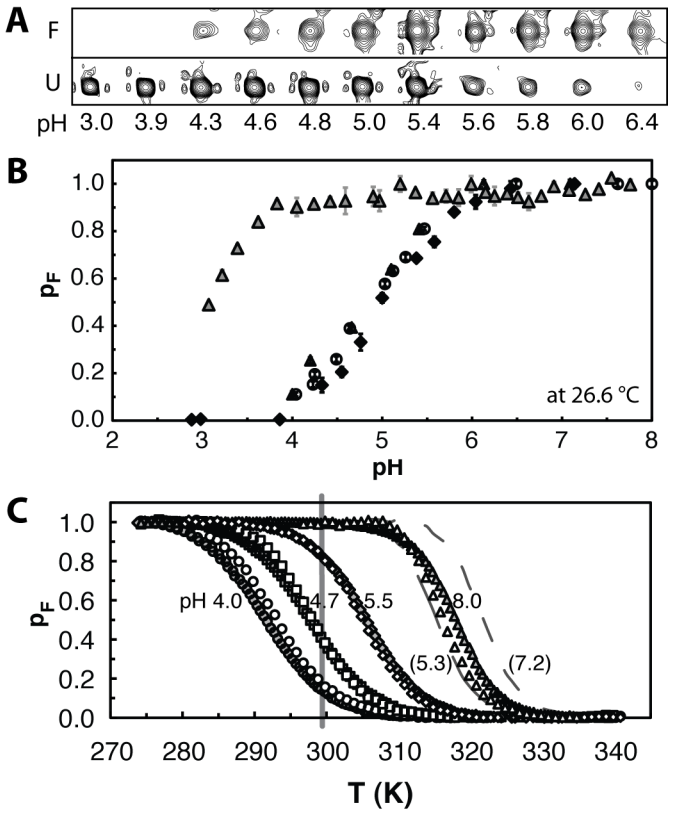

Figure 2.2. Unfolding behavior of WT and H87Y TrAvrPto. (A) Folded (F) and Unfolded (U) NMR peaks at the same contour level for a representative residue Gly 95 illustrates the data used to generate the TrAvrPto acid denaturation profile over pH. (B) TrAvrPto folded state (p_F) population as a function of pH, as determined for WT protein by NMR (◆), Fl (△), and CD (○), and for H87Y mutant by Fl at equilibrium in solution (▲). (C) Fl and CD thermal denaturation data for WT and H87Y TrAvrPto illustrating the unfolding trend shown at pH intervals. WT CD at pH 4.0 (●), 4.6 (■), 5.5 (◆), and 8.0 (▲), Fl at pH 4.0 (○), 4.7 (□), 5.4 (◇), and 7.1 (△). H87Y Fl thermal denaturation shift is indicated at pH 5.3 (value in parentheses, long-dash line) and 7.2 (value in parenthesis, short-dash line). Vertical solid line at 26.6 °C designates NMR experiment temperature.

Our results were additionally confirmed to be protein concentration-independent by comparing the full NMR data set against another fHSQC NMR experiment using diluted 80 μM TrAvrPto at pH 5.0, at the steepest region at about the midpoint of the unfolding curve. Example peak overlay for two representative residues Gly 95 (in the omega loop) and Gly 125 (α-helix 4) shows no significant difference between the results (Figure 2.3). Calculated overall p_F value averages for this comparison at pH 5.0 were 0.52 ± 0.02 for both 420 μM and 80 μM WT TrAvrPto samples (individual residue data shown in Table 2.1).

Table 2.1. Calculated individual p_F values for ^{15}N-^{1}H fHSQC data collected at 420 μM and 80 μM to confirm concentration independence of the NMR data.

p_F at [sample]	**A47**	**G48**	**A61**	**T76**	**T91**	**G92**	**G95**	**G99**	**L101**	**E104**	**A112**	**W116**	**G128**
420 μM	0.523	0.514	0.555	0.510	0.516	0.524	0.517	0.542	0.539	0.509	0.493	0.525	0.500
80 μM	0.515	0.515	0.543	0.505	0.508	0.506	0.524	0.543	0.559	0.508	0.486	0.525	0.482

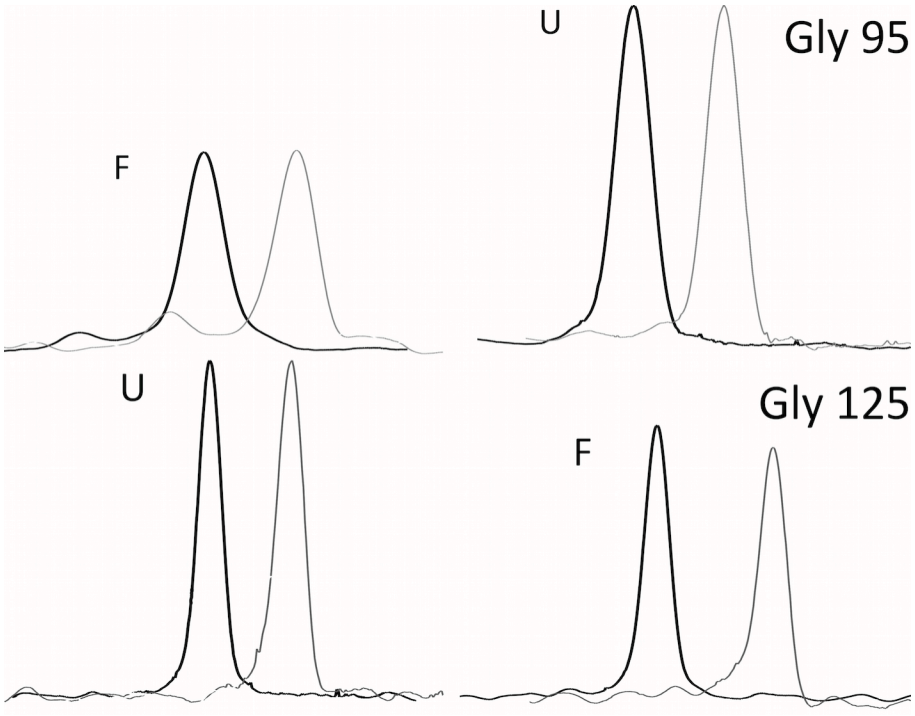

Figure 2.3. Comparison of ^{15}N-^{1}H fHSQC data at 420 μM and 80 μM. Offset overlay of 1-dimensional slices through peaks in ^{15}N-^{1}H fHSQC spectra of WT TrAvrPto corresponding to the folded (F) and unfolded (U) states of residues Gly 95 (loop region) and Gly 125 (α-helix 4) in pH 5.0 samples at protein concentrations of 420 μM (black lines) and 80 μM (gray lines offset for clarity). (B) Individual p_F values calculated at 420 μM and 80 μM.

Buried histidine 87 has a depressed pK_a. Protein cellular and subcellular localization correlates with pH-dependent adaptation (Garcia-Moreno, 2009). Protein stability, solubility or interactions may depend on the tightly regulated pH of the living systems. Since AvrPto is exposed to different cellular environments, the distribution of AvrPto stability as a function of pH must follow its functional requirements. WT TrAvrPto is stable at neutral pH and starts to unfold at around pH 6, the predicted environment in the bacterial cell (see Discussion, below). Protein pH-dependence of folding free energy is due to the ionizable groups, therefore we focused on histidine titration as the possible driving force in the unfolding process and determined individual histidine side chain pK_a values.

Heteronuclear multiple-quantum coherence (HMQC) NMR experiments on uniformly-labeled ^{15}N WT TrAvrPto samples at a range of pH values were performed to determine individual His pK_a and tautomeric state. These experiments were optimized for two-bond scalar-coupled $^{15}N(\delta1/\varepsilon2)$-$C(\varepsilon1/\delta2)$-$^{1}H$ and allowed the assignments of signals that reflect His Nδ1 and Nε2 local environments (Figure 2.4A) (Pelton et al., 1993). The tautomeric state of each His sidechain were found to be primarily in the Nε2-Hε2 state (Figure 2.4B). The other possible Nδ1-Hδ1 tautomers were experimentally visible at low levels (as shown in Figure 2.4A) with the exception of His 130 that gave rise to only one preferred tautomer signal. The other histidines were either in fast (H41, H54, H75, H125) or intermediate (H87, H103) tautomer exchange at neutral pH.

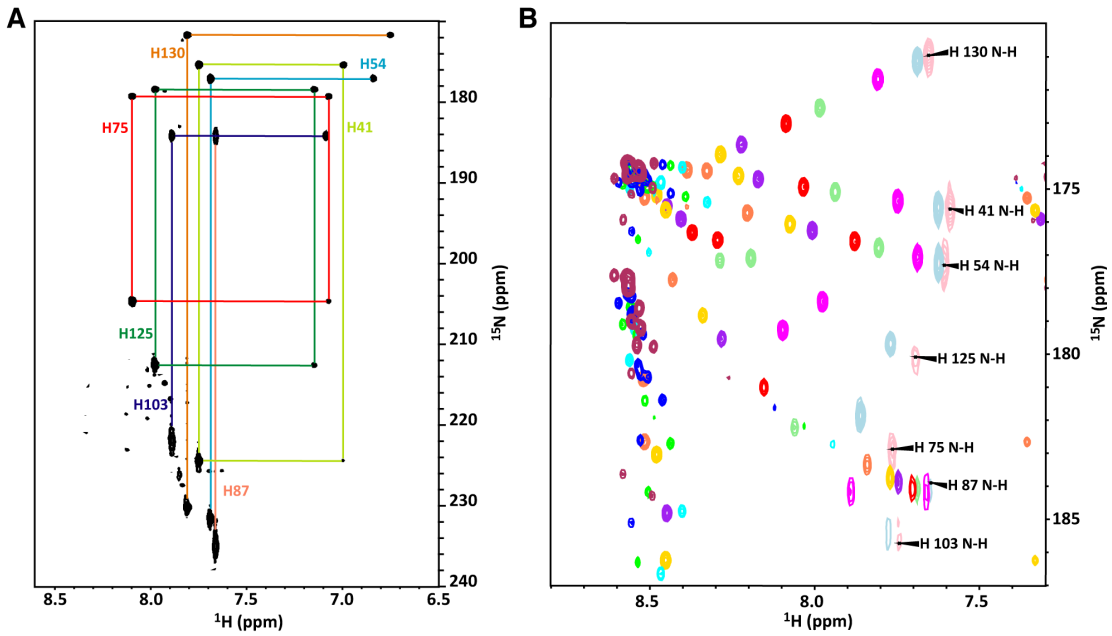

Figure 2.4. Histidine pK_a values indicate the functional significance of His 87. (A) ^{15}N-^{1}H HMQC spectrum of TrAvrPto at pH 7.0. The peak patterns indicate that each side chain is predominantly in the Nε2-H tautomeric state. (B) Expanded region (corresponding to the $^{15}N\varepsilon2$-$^{1}H\varepsilon1$ peak region) of ^{15}N–^{1}H HMQC spectra of WT TrAvrPto at pH 4.85 (maroon), 5.05 (blue), 5.20 (green), 5.39 (cyan), 5.63 (coral), 5.90 (gold), 6.02 (purple), 6.32 (red), 6.58 (light green), 6.93 (magenta), 7.51 (light blue), and 7.83 (pink). In the absence of tautomer exchange, as one ^{15}N is protonated, its peak should shift to higher ^{15}N frequency (downfield), whereas the other ^{15}N peak moves to lower frequency (upfield). This is precisely what is observed for H130, with the protonating $^{15}N\varepsilon2$ shifting to higher ^{15}N frequency. Conversely, fast and intermediate tautomer exchange typically causes the protonated ^{15}N peak to move downfield with increase in pH. The remaining 6 histidines of TrAvrPto display this behavior. Additionally, the line widths of H87 and H103 broaden in the ^{15}N dimension as pH is increased, consistent with the intermediate exchange with neutral tautomers. The side chains H41, H54, H75, and H125 display little to no line broadening, indicating that the tautomerization rates of these side chains are faster than those of H87 and H103.

Histidine side chain NMR peak shifts were tracked over sample pH and fit to obtain individual residue pK_a (Figure 2.5A). Fitting of individual chemical shift data points was done using Equation 2.6 and the resulting pK_a values can be separated into three categories: solvent-exposed around 6.3-6.5, elevated above 6.5 or depressed below 6.3 (Table 2.2) (Thurlkill et al., 2006). Most of the pK_a values show small variations, with a His 87 most significantly depressed by a ΔpK_a of -1.7. The local His 87 protein interior environment features a weak hydrogen bond to Ser 33 backbone and a generally desolvated buried side chain (Figure 2.5B). Other downshifted pK_a values may indicate hydrogen-bonding networks within the protein (polar Ser 54, Glu 55, Tyr 69, Asn 70 groups surrounding His 54), and upshifted pK_a values indicate negative environment influence (Asp 108 close to His 75; Glu 121 in the vicinity of His 130).

Table 2.2. Individually-determined pK_a values for every histidine in TrAvrPto, grouped by their deviation from the solvent-exposed value of ~ 6.5 (Thurlkill et al., 2006). Difference in each pK_a value from 6.5 is shown ($\Delta pK_a = pK_a - 6.5$).

	Residue	**pK_a**	**ΔpK_a**
Solvent-exposed pK_a values	His 41	6.32 ± 0.04	-0.18
	His 103	6.28 ± 0.02	-0.22
	His 130	6.28 ± 0.03	-0.22
Elevated pK_a values	His 75	6.89 ± 0.01	0.39
	His 125	6.65 ± 0.01	0.15
Depressed pK_a values	His 54	5.88 ± 0.01	-0.62
	His 87	**4.8 ± 0.1**	**-1.7**

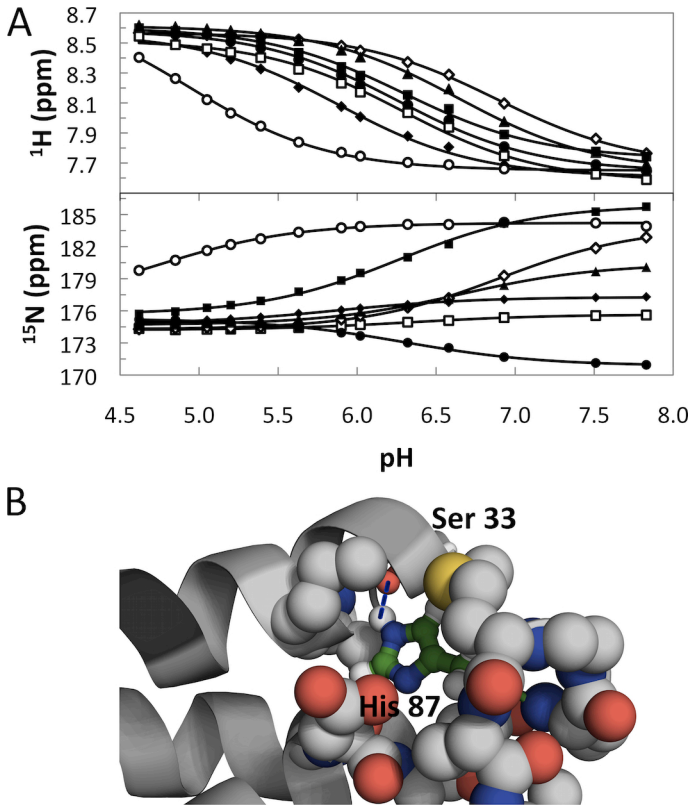

Figure 2.5. Individual histidine pK_a determination reveals the importance of the His 87 buried environment. (A) ^{15}Nε2 and ^{1}Hε1 chemical shift changes over pH are shown. They were fit to yield pK_a values for His 41 (□), His 54 (⬧), His 75 (◇), His 87 (○), His 103 (■), His 125 (▲), His 130 (●). Data points are connected by a best fit line calculated using Equation 2.6. (B) His 87 is predicted to be hydrogen-bonded through its Nε2-Hε2 donor to the Ser 33 backbone carbonyl oxygen acceptor. His 87 protonation disfavors this desolvated local environment.

Histidine 87 drives WT TrAvrPto acid denaturation. Since protein electrostatics is the driving force in pH-dependent unfolding, we focused on the role of His 87 in this process. His 87 is the least solvent-exposed residue among the seven histidines in TrAvrPto among the eight total in AvrPto (Table 2.3). One additional histidine (His 13) is in the disordered N-terminus that was truncated from the TrAvrPto construct to minimize NMR spectral overlap. The most buried His 87 with the significantly downshifted pK_a value indicates that it drives the acid-induced unfolding of TrAvrPto by destabilizing the structure with an introduction of a positive charge in the His 87 cavity at low pH.

Table 2.3. Exposed surface area of the histidine residues in TrAvrPto. Residues are listed in increasing surface area (in $Å^2$), calculated based on the averaged NMR structure, PDB ID 1R5E. Surface area was calculated using CCP4 6.1.2 program AREAIMOL using the probe solvent molecule of radius 1.4 Å and sampling 10 surface points per $Å^2$. Hydrogen atoms were excluded from the calculation. Total accessible surface area of the chain is given in parentheses next to the protein name. The most highly buried His 87 is highlighted in bold.

Protein construct (total surface area, $Å^2$)	**Residue**	**No.**	**Surface area ($Å^2$)**
TrAvrPto (7,036.3 $Å^2$)	**His**	**87**	**4.3**
	His	103	74.1
	His	41	76.4
	His	54	91.4
	His	125	92.4
	His	75	95.4
	His	130	143.9

In order to demonstrate that His 87 functions as a pH sensor in the AvrPto folding switch, we introduced a mutation in TrAvrPto whereby the His 87 folding switch was substituted with Tyr (H87Y mutant). Tryptophan fluorescence (Fl) data was collected on H87Y TrAvrPto dilute protein samples equilibrated at the McIlvaine's buffer across the pH range of 3.07–7.76. Folded population was estimated as a signal fraction between average fully folded signal and the averaged fully unfolded value of the WT protein obtained from the same experiment using WT TrAvrPto (data not shown). H87Y TrAvrPto Fl data shows a clear shift into a more acidic unfolding region and no unfolded population at the WT unfolding region within experimental error (Figure 2.2B). This data was supported by the shift in Fl thermal denaturation observed for H87Y TrAvrPto (Figure 2.2C). H87Y TrAvrPto requires an increase in temperature to unfold, as shown for pH 5 and 7 data, indicating a mutant structure that is slightly stabilized with respect to WT at neutral pH where both structures are primarily folded at room temperature (RT). In the pH 5 range there is a more pronounced destabilization effect of His 87 as the WT has a significant unfolded population at RT while H87Y is mostly folded.

Discussion

We present here the characterization of a bacterial effector protein AvrPto in terms of its thermodynamic adaptation to the environment of the biological system. There are unique structural requirements exerted on the effectors passing through the T3SS, and AvrPto is a model example of a cytoplasmic protein that is targeted to the T3SS export without the action of chaperones that would maintain their cargo effectors in the protected T3S-competent

unfolded form. As most of *P. syringae* effectors don't have known chaperones, our focus on AvrPto may have broader implications in effector structural requirements.

AvrPto adopts a structured core of marginal stability of -2 kcal/mol (WT TrAvrPto $\Delta G_{U\rightarrow F}$) at pH 7 (Dawson and Nicholson, 2008). We determined the equilibrium unfolded population of AvrPto across pH range 3-8 and observed no evidence for intermediate structures. Since AvrPto unfolds in a single step, we conclude that it is translocated in the fully unfolded form without retaining any secondary structure.

The folded AvrPto form predominates at neutral pH, maximizing the impact of the effector that is folded upon delivery inside host cells. For comparison, at pH 6 the unfolded population increases to $8 \pm 3\%$ (NMR fHSQC data point), providing the unfolded AvrPto capable of translocation while minimizing the potential for aggregation or degradation, particularly by Lon protease (Losada and Hutcheson, 2005). Since the half-life of WT AvrPto is known to be approximately 8 min in *P. syringae* pv tomato DC3000 WT cells (Losada and Hutcheson, 2005), and its unfolding rate *in vitro* has been determined at pH 6.1 by NMR to be $0.33\ s^{-1}$ (Dawson and Nicholson, 2008), our *in vitro* data confirms that an unfolded pool of AvrPto can be maintained for secretion in midly acidic pH (lower than the predicted pH ~6.5, below).

It is known that pH of protein maximal stability correlates with intracellular localization pH (Chan et al., 2006). Since AvrPto is most stable at neutral and higher pH, it has likely evolved for the primary function in the host cell cytoplasm of about pH 7.4. Proteins typically carry a net charge in their subcellular locations, consistent with solubility requirements in crowded cellular environments. AvrPto, with a pI of 6.52, is negatively charged in the

pH-neutral host cell, and it can be inferred that *P. syringae* intracellular pH would be below AvrPto's pI in order to maintain solubility and a sufficient unfolded AvrPto population available for translocation. Also, given the predicted negative electrostatics in the bacterial membrane and the T3SS channel surface that effectors are exposed to during translocation, it would be energetically favorable to translocate AvrPto while it has a net positive charge in acidic pH below its pI of 6.52 (Rathinavelan et al., 2010).

Given this predicted physiological pH of the system of below pH 6.5 changing in one step to above pH 7, AvrPto is uniquely adapted for function through a pH sensor, encoded in a buried His 87. The role of histidine residues has been implicated in biological processes that have strong correlation with structural pH sensitivity. The solvent-exposed intrinsic histidine side chain pK_a of approximately pH 6.3–6.5 is in the range of the physiological conditions in a wide array of intracellular environments (Thurlkill et al., 2006). Histidine protonation state determines its interaction preferences within the protein structure. Histidine is the second least common residue with an ionizable sidechain in protein sequences (2.2% across all three kingdoms of life) and is typically likely to be buried in the interior of protein structures (72% buried) (Pace et al., 2009). Given the 4.9% histidine content in AvrPto (7.2% abundance within the structured 33–129 residue core) and only one buried histidine (amounting to only 12.5% buried in 8 AvrPto histidines), there may be an evolutionary trend towards the specific functional incorporation of histidines in this structure that deviate from the average histidine distribution found in nature.

We confirmed the importance of WT TrAvrPto seven histidine residues by first determining their individual pK_a values by HMQC NMR. Given the

biological range of broadly 6.0–6.5 for histidine pK_a, most of the AvrPto histidine sidechains fall in the predicted water-exposed value range. The highest elevated value of relatively solvent-exposed His 125 (6.89 ± 0.01, Table 2.2) indicates a negative C-terminal environment at the end of α-helix 4 where a positively charged histidine is preferred. However, neighboring His 130 in the disordered C-terminus affording more conformational degrees of freedom with a somewhat depressed pK_a of 6.28 ± 0.03 does not maintain the trend. On the other end of the pK_a range is His 54 in the small orthogonal α-helix 2 that has a depressed value of 5.88 ± 0.01 consistent with polar or negative surroundings. On the opposing end of the WT TrAvrPto structure, the most important outlier is His 87 (lowest pK_a 4.8 ± 0.1) in the loop joining α-helices 3 and 4 with a buried sidechain pointing towards α-helix 1 and hydrogen-bonding at its Nε2 with the backbone of Ser 33 in α-helix 1. The structured environment around His 87 sidechain affords little direct exposure to solvent (Table 2.3) and does not accommodate a charge in the folded form. We predict that electrostatic destabilization afforded by the His 87 protonation event drives acid denaturation of WT AvrPto.

Initial data for the confirmation of the His 87 role in driving pH-dependent unfolding sensitivity is illustrated by H87Y TrAvrPto mutation. Fl equilibrium unfolding fluorescence in Figure 2.2B shows a significant shift in the unfolded protein population relative to WT into the acidic range by about pH 1.5, and likewise the Fl temperature stability of H87Y TrAvrPto indicates a more stable folded form (Figure 2.2C). While further characterization of H87Y mutation follows (Chapter 3), our current unfolding data on TrAvrPto elucidates the presence of a pH-modulated folding switch in an effector

protein for the first time and signify a role of a single residue protonation rather a global pH effect on the structure.

Other evolutionarily-independent histidine folding switches have been implicated in protein structural rearrangements in unrelated pathogenic contexts. Pore-forming toxin aerolysin in Gram-negative pathogen *Aeromonas hydrophila* is known to undergo a critical oligomerization step into ring-like structures at the host cell plasma membrane prior to incorporation into the membrane and the resulting pores (Fivaz et al., 2001). Transition into a constructive membrane protein requires a conformational rearrangement in aerolysin that is initiated by a histidine (His 132) protonation event in order to destabilize the monomeric β-sheet form, and nucleate oligomerization (Buckley et al., 1995). This step is pH-dependent and is inhibited at pH above the elevated His 132 apparent pK_a of 7.8 (Buckley et al., 1995). Similarly, pore-forming anthrax toxin protective antigen (PA) component also undergoes soluble prepore to membrane-pore conformational change through the action of histidine protonation in the acidic environment (pH ~ 5–6) of host endosomes (Wimalasena et al., 2010). Upon acidification and PA histidine protonation prepore sustains β-strand unfolding to form a membrane pore (Wimalasena et al., 2010). Example of helical structure destabilization by histidine protonation is the diphtheria toxin translocation (T) domain, where His 257 acts as a component of the pH-dependent conformational switch that destabilizes the folded conformation at endocomal pH and promotes initial endosomal membrane insertion (Rodnin et al., 2010). In addition to toxins that rely on endosomal entry and soluble form to membrane-bound conformational changes that employ histidine ionizable side chain protonation change, other examples include depressed pK_a values of apomyoglobin (Yang

and Honig, 1994) histidine and staphylococcal nuclease (Fitch et al., 2006) carboxylic acid side chains that drive protein unfolding in acidic pH.

In conclusion, various individual residue protonation events are employed as pH-sensors in macromolecular structures in nature, with several cases involving histidine side chains. Here we add another example of the presence of a specific histidine pH-folding switch that enables a bacterial effector protein to be delivered and refolded into the host for remote host cellular control. Since such detailed mechanistic studies are lacking for the other known effector structures in *P. syringae* or indeed other T3SS-capable Gram-negative bacteria, it is unknown how widespread the involvement of histidine residues might be in the translocation process.

Materials and Methods

Mutagenesis. H87Y mutant was obtained by modifying WT TrAvrPto in the original pQE9 (Qiagen) vector (Dawson and Nicholson, 2008). Primers 5′-(GGCGGACATGCAG**TAT**AGGTACATGACGGGAGCG)-3′ and 3′-(CGCTCCCGTCATGTACCT**ATA**CTGCATGTCCGCC)-5′ (mutation site highlighted) were used as a sense and antisense primers in a PCR reaction performed with the QuickChange II Site-Directed Mutagenesis kit (Stratagene) following the manufacturer's procedure.

Protein expression and purification. *Escherischia coli* M15 (pREP4) cells (Qiagen) containing the WT or H87Y plasmids were grown in a 10-mL starter culture in enriched LB media (containing 0.5% wt/vol D-glucose, 2 mM $MgSO_4$, 0.1 mM $CaCl_2$, 0.05 mM $FeSO_4$) with 100 μg/mL ampicillin (sodium

salt) and 40 μg/mL kanamycin monosulfate at 37 °C for ~ 10 h. The cells were pelleted by 10 min 2,700×g centrifugation, resuspended and inoculated into 50 mL of M9 media, enriched in a similar manner with additional 19 mM $^{15}NH_4Cl$ and 1 mM thiamine HCl, for an overnight growth. The resulting cell culture was again gently pelleted, resuspended, and added to a final 1-L M9 minimal media prepared in the same way and grown to an OD at 600 nm of 0.8–1.0, at which point the media was transferred to a shaker equilibrated at 15 °C, and protein overexpression was induced with 0.8 mM isopropyl β-D-1-thiogalactopyranoside for 24 h. Natural abundance protein samples were prepared in a similar fashion by growing one 10-mL enriched LB culture starter overnight and then inoculating into a 1-L enriched LB media. Cells were harvested by centrifugation, resuspended in the lysis buffer of 50 mM NaH_2PO_4, 300 mM NaCl, and 0.2 mM phenylmethanesulphonylfluoride, and frozen at -80 °C for at least overnight.

The cells were defrosted, prelysed with 1 mg/mL lysozyme for 30 min at 4 °C while rocking, and lysed using a Cell Disruptor model W-375 (Ultrasonics). Upon centrifugation, the protein was purified using a 3-mL Ni-NTA (Qiagen) column, eluted upon N-terminal $(His)_6$ tag cleavage with protease 3C prom a picornavirus (3CPro) and dialyzed against the final pH 7 McIlvaine's citric acid-phosphate buffer (McIlvaine, 1921) with 5 mM sodium azide, prepared at the ionic strength of 230 mM. Concentrated protein solution was stored at 4 °C for the duration of the experiments. Buffer ionic strength was maintained at 230 mM throughout the experiments by buffer-exchanging the stock protein solution into the buffer where pH was adjusted by varying the amounts of 230 mM ionic strength component solutions of 38.3 mM citric

acid and 76.7 mM disodium phosphate, both containing 5 mM sodium azide as an antibacterial preservative.

CD spectroscopy. The CD experiments were performed using an Aviv Biochemical Circular Dichroism Spectrometer, model 202-01. The thermal denaturation of 80 μM TrAvrPto solutions of varying pH were quantified by monitoring the CD signal at 220 nm as a function of temperature (Figure 2.6A) over the range of 1–80 °C from pH 4.04 to 8.00 for a total of 12 pH samples. CD 260–190 nm scan spectra were collected at 25 °C and representative scans are shown (Figure 2.6B). Additionally, pH 4.04 sample scan was recorded at 1 °C where the protein is folded, in order to confirm no difference in secondary structure (Figure 2.6B). Quartz cuvette with 0.1-cm path-length was used. Scan data is shown in the 260–202 nm range due to the interference of the solvent signal in the 200–190 nm range. Mean-residue CD extinction coefficient $\Delta\varepsilon_{MRW}$ was calculated as:

$$\Delta\varepsilon_{MRW} = \frac{S \times MRW}{32,980 \times C_{mg/mL} \times L}, \qquad 2.1$$

where S is the observed CD signal in millidegrees, MRW is the mean residue weight (calculated by using 12,029.3 kDa and 107 residues for WT TrAvrPto), L is the path-length in cm, and $C_{mg/mL}$ is the protein concentration in mg/mL (Martin and Schilstra, 2008).

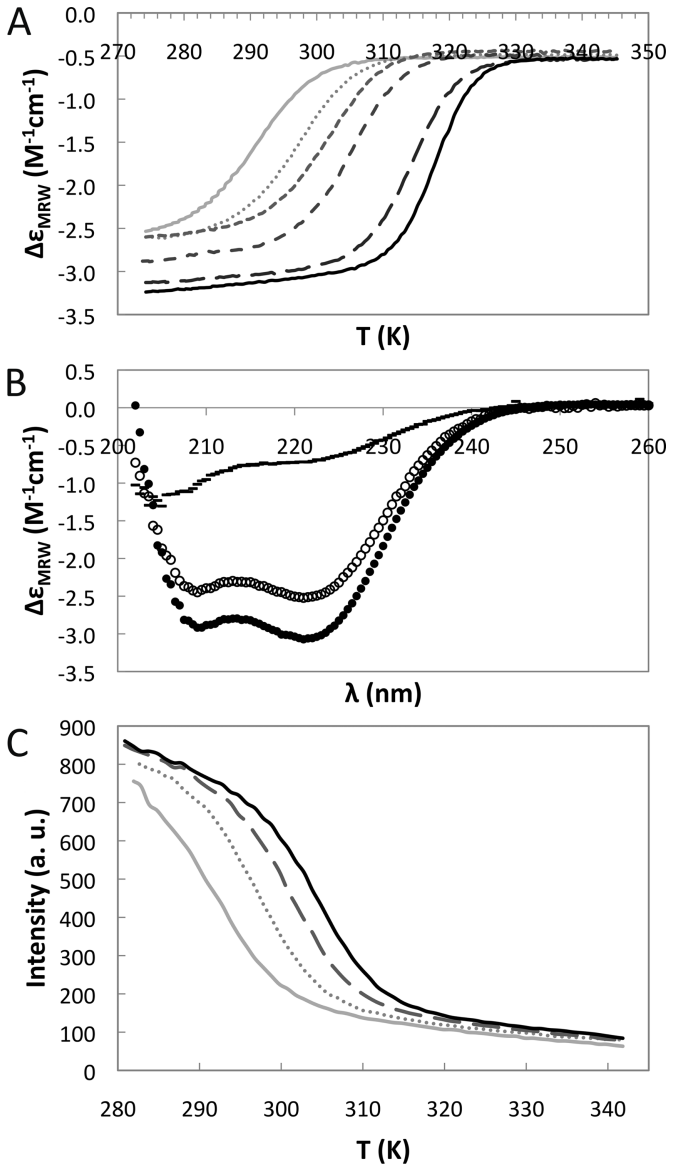

Figure 2.6. WT TrAvrPto CD and Fl data. (A) Mean-residue CD extinction coefficient $\Delta\varepsilon_{MFW}$ shown for the temperature denaturation curves at pH 4.04 (solid light-gray line), 4.46 (dotted light-gray line), 5.12, 5.47, 6.49 (dashed gray lines in creasing dash length), and pH 8.00 (solid black line). (B) Scans of WT TrAvrPto showing mean-residue CD extinction coefficient over 202–260 nm range at pH 4.04 at 25 °C (dashes), pH 4.04 at 1 °C (open circles), and pH 8.00 at 25 °C (filled circles). (C) Fl temperature denaturation curves for WT TrAvrPto at pH 4.00 (the lighest solid gray line), 4.66 (dotted gray line), 5.10 (dashed gray line) and 5.41 (black solid line).

Determination of p_F from temperature denaturation curves was done using a standard fitting analysis as described (Greenfield, 2006). Briefly, p_F was obtained at a given temperature point by:

$$p_F = \frac{y_{obs} - y_F}{y_U - y_F}, \qquad 2.2$$

where y is $\Delta\varepsilon_{MRW}$ for the CD experiments, and $\Delta\varepsilon_{MRW,F}$ and $\Delta\varepsilon_{MRW,U}$ were extrapolated from the linear fits of the regions where the data gives either the fully folded or unfolded protein signal.

Errors in thermal denaturation measurements were predicted to be dominated by the temperature uncertainty. Uncertainty in temperature includes variation in the temperature calibration of the different instruments used (approximately ± 0.1 °C), incomplete equilibration between data points (approximated at ± 0.05 °C), and temperature measurement error (~ ± 0.05 °C), and was estimated to be a total of ± 0.2 °C. This temperature error was propagated via the linear relationship between temperature and p_F to yield the uncertainty in p_F.

Tryptophan fluorescence (Fl) spectroscopy. The Fl temperature denaturation measurements were performed using a Cary Eclipse Fluorescence Spectrophotometer (Varian Instruments). The thermal denaturation of 80 μM TrAvrPto was quantified from pH 4.00 to 7.09 for a total of seven pH values over the temperature range of 7–80 °C (Figure 2.6C). Fl was measured at 343 nm emission upon excitation of the centrally-buried Trp 116 (Figure 2.1B) at 295 nm. Fluorescence scans in the range of 300–400 nm were taken to confirm the emission peak maximum of ~343 nm for most samples. The p_F values were obtained from the Fl signal using Equation 2.2,

where in this case y denotes the measured intensity. Errors in p_F were estimated from the temperature uncertainty as described above for CD experiments.

The acid denaturation by Fl was measured using a Synergy HT 96-well plate reader (BioTek). Data were acquired in a time-resolved Fl mode using an excitation filter of 286 ± 5 nm and an emission filter at 360 ± 20 nm. Scans were measured in triplicate to obtain the average values and their intensities. The p_F was calculated from Equation 2.2, with y_{obs} denoting the observed intensity, and the folded (y_F) and unfolded (y_U) limits of Fl signal taken as the average of the 8 highest pH points for y_F and as the lowest Fl signal from the unfolded WT data for y_U.

NMR spectroscopy. All NMR data were collected using a Varian Inova 600-MHz spectrometer (Varian Instruments). Temperature was kept constant at a 25 °C setting, which was later measured to correspond to 26.6 °C via a methanol standard calibration. The fHSQC spectra (Mulder et al., 1996) were acquired with a recycle delay of 5 s on 0.3–0.6 mM samples at pH 2.88–7.14 for a total of 13 pH values. To correct for the differences in relaxation rates of the F and U states during forward and reverse INEPT steps, the fHSQC experiments were also performed with a recycle delay of 1 s and J_{NH} set to 95 and 32 Hz to obtain peak volumes at INEPT delays of $1/(4J)$ and $3/(4J)$, respectively. The average transverse relaxation of the in-phase and anti-phase ^{1}H magnetizations during INEPT transfer steps, R_{2H}^{avg}, was obtained for each residue from the fHSQC data with varied INEPT delays as:

$$R_2^j = \frac{\ln(I_j^{\tau 1} - I_j^{\tau 2})}{4\tau_2 - 4\tau_1}, \qquad 2.3$$

using peak intensities I from the 2 measurements at $\tau_1 = 1/(4J)$ and $\tau_2 = 3/(4J)$ to calculate R_2 for each residue j. The same peak pairs were monitored at pH 5.05–6.02 range in a total of 6 pH steps.

Reported p_F values of each pH sample were measured as:

$$p_F = \frac{V_F/A_F}{V_F/A_F - V_U/A_U}, \qquad 2.4$$

where the values for F and U peak volumes V were obtained from the fHSQC with a long recycle delay (5 s) to ensure full relaxation of magnetization (Tollinger et al., 2001). Applied correction factors A for each individual residue accounted for the different relaxation rates of the F and U states during the INEPT transfer. The correction factors were then obtained by calculated the resulting effect of R_2 relaxation for the total INEPT delay times $[4\tau = 4 \times 1/(4J) = 1/J]$:

$$A^j = \exp(R_2^j \times 1 / J), \qquad 2.5$$

where $J = 95$ Hz for the fHSQC experiment with a recycle delay of 5 s.

Histidine sidechain pK_a values were quantified via a series of HMQC NMR experiments at pH 4.62–7.83 in a total of 13 pH steps (pH 4.85–7.83 shown in Figure 2.7). A J coupling of 20 Hz was found empirically to yield the optimal spectra, compensating for spin relaxation during the experiment. The desired resonances were recorded by using a 10,000-Hz (8,507-Hz) sweep widths centered at 4.75 ppm (230 ppm) in the ^1H (^{15}N) dimension. A recycle delay of 1 s was used for all spectra.

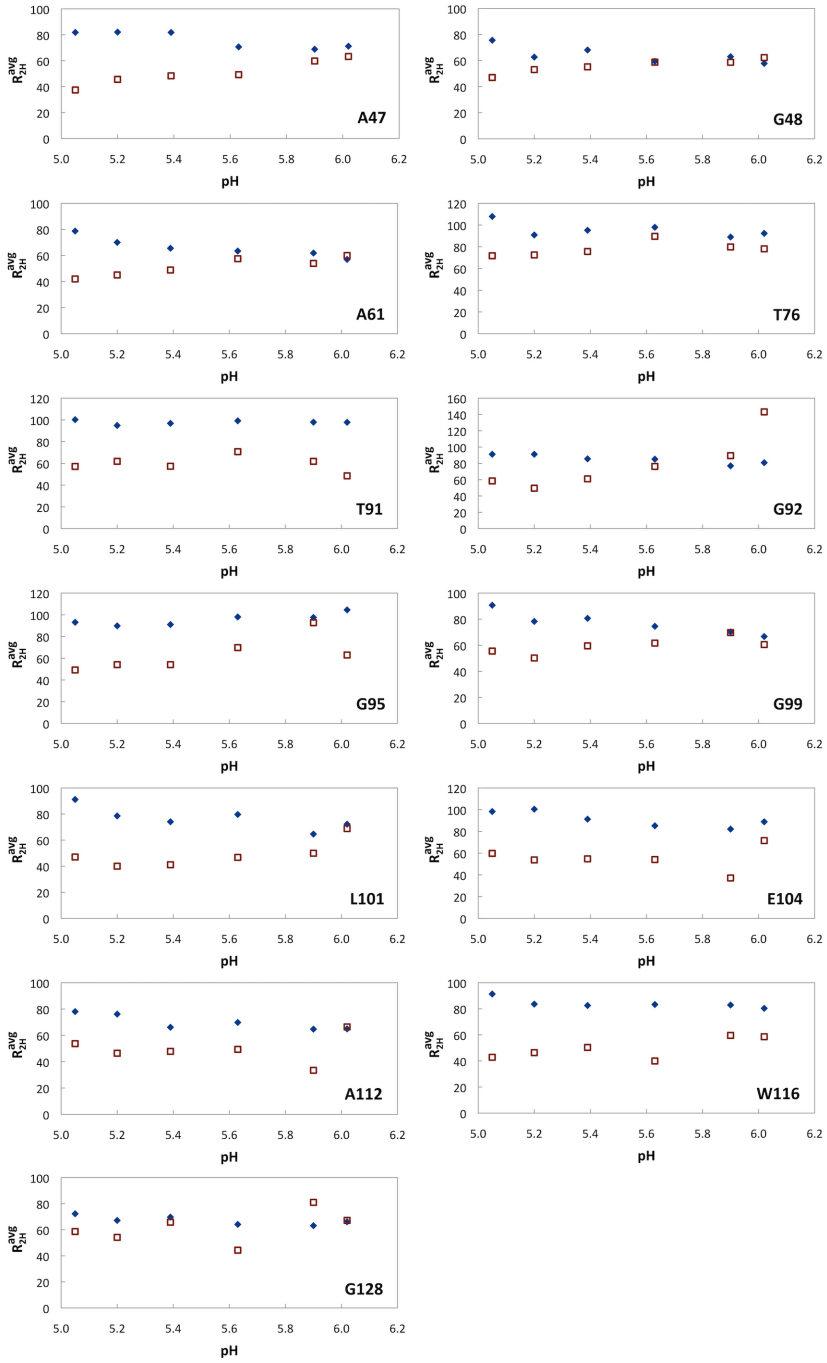

Figure 2.7. Average proton transfer relaxation rates, R_{2H}^{avg} (s^{-1}), for the folded (filled diamonds) and unfolded (open squares) peaks of the analyzed residues plotted over the experimental pH values.

HMQC chemical shift data ω(pH) were fit to:

$$\omega(\mathrm{pH}) = \frac{\omega_{\mathrm{His}^+} + \omega_{\mathrm{His}^0} \times 10^{\mathrm{pH}-\mathrm{pK_a}}}{1 + 10^{\mathrm{pH}-\mathrm{pK_a}}}, \qquad 2.6$$

where ω_{His+} and ω_{His0} are the chemical shifts for the charged histidine signal (His^+) and the neutral form signal (His^0), respectively, and pK_a is the pH at which half of the histidines are protonated (His^+). The ^{15}N and ^{1}H chemical shifts were fitted separately, with the average values and the corresponding standard deviation reported as the final pK_a values for His 41, 54, 75, 87, 103, 125, and 130 in WT TrAvrPto. Fitting of the data was done with Excel Solver 12.1.1 (Frontline Systems).

All NMR data were processed using NMRPipe and NMRDraw (Delaglio et al., 1995). Spectra were visualized, and peak volumes determined using Sparky 3.1 (Goddard and Kneller). Integration settings assumed a Gaussian line shape with allowed peak motions and adjustment of line widths.

BIBLIOGRAPHY

Abramovitch, R.B., Anderson, J.C., and Martin, G.B. (2006). Bacterial elicitation and evasion of plant innate immunity. Nature Reviews Molecular Cell Biology *7*, 601-611.

Alfano, J.R., and Collmer, A. (2004). Type III secretion system effector proteins: double agents in bacterial disease and plant defense. Annu Rev Phytopathol *42*, 385-414.

Buckley, J.T., Wilmsen, H.U., Lesieur, C., Schulze, A., Pattus, F., Parker, M.W., and van der Goot, F.G. (1995). Protonation of histidine-132 promotes oligomerization of the channel-forming toxin aerolysin. Biochemistry *34*, 16450-16455.

Chan, P., Lovrić, J., and Warwicker, J. (2006). Subcellular pH and predicted pH-dependent features of proteins. Proteomics *6*, 3494-3501.

Daniell, S.J., Kocsis, E., Morris, E., Knutton, S., Booy, F.P., and Frankel, G. (2003). 3D structure of EspA filaments from enteropathogenic Escherichia coli. Molecular Microbiology *49*, 301-308.

Dawson, J.E., and Nicholson, L.K. (2008). Folding kinetics and thermodynamics of Pseudomonas syringae effector protein AvrPto provide insight into translocation via the type III secretion system. Protein Sci *17*, 1109-1119.

Delaglio, F., Grzesiek, S., Vuister, G.W., Zhu, G., Pfeifer, J., and Bax, A. (1995). NMRPipe: a multidimensional spectral processing system based on UNIX pipes. J Biomol NMR *6*, 277-293.

Fitch, C.A., Whitten, S.T., Hilser, V.J., and García-Moreno E, B. (2006). Molecular mechanisms of pH-driven conformational transitions of proteins: insights from continuum electrostatics calculations of acid unfolding. Proteins *63*, 113-126.

Fivaz, M., Abrami, L., Tsitrin, Y., and van der Goot, F.G. (2001). Not as simple as just punching a hole. Toxicon *39*, 1637-1645.

Garcia-Moreno, B. (2009). Adaptations of proteins to cellular and subcellular pH. Journal of Biology *8*, 98.

Goddard, T.D., and Kneller, D.G. SPARKY 3. University of California, San Francisco.

Grant, S.R., Fisher, E.J., Chang, J.H., Mole, B.M., and Dangl, J.L. (2006). Subterfuge and manipulation: type III effector proteins of phytopathogenic bacteria. Annu Rev Microbiol *60*, 425-449.

Greenfield, N.J. (2006). Determination of the folding of proteins as a function of denaturants, osmolytes or ligands using circular dichroism. Nat Protoc *1*, 2733-2741.

Hématy, K., Cherk, C., and Somerville, S. (2009). Host-pathogen warfare at the plant cell wall. Curr Opin Plant Biol *12*, 406-413.

Hoiczyk, E., and Blobel, G. (2001). Polymerization of a single protein of the pathogen Yersinia enterocolitica into needles punctures eukaryotic cells. Proceedings of the National Academy of Sciences of the United States of America *98*, 4669-4674.

Keen, N.T. (1990). Gene-for-gene complementarity in plant-pathogen interactions. Annu Rev Genet *24*, 447-463.

Klement, Z., and Goodman, R. (1967). The hypersensitive reaction to infection by bacterial plant pathogens. Annu Rev Phytopathol *5*, 17-44.

Losada, L.C., and Hutcheson, S.W. (2005). Type III secretion chaperones of Pseudomonas syringae protect effectors from Lon-associated degradation. Molecular Microbiology *55*, 941-953.

Martin, S.R., and Schilstra, M.J. (2008). Circular dichroism and its application to the study of biomolecules. Methods Cell Biol *84*, 263-293.

McIlvaine, T. (1921). A buffer solution for colorimetric comparison. Journal of Biological Chemistry *49*, 183-186.

Mulder, F., Spronk, C., Slijper, M., Kaptein, R., and Boelens, R. (1996). Improved HSQC experiments for the observation of exchange broadened signals. J Biomol NMR *8*, 223-228.

Pace, C.N., Grimsley, G.R., and Scholtz, J.M. (2009). Protein ionizable groups: pK values and their contribution to protein stability and solubility. J Biol Chem *284*, 13285-13289.

Pelton, J.G., Torchia, D.A., Meadow, N.D., and Roseman, S. (1993). Tautomeric states of the active-site histidines of phosphorylated and unphosphorylated IIIGlc, a signal-transducing protein from Escherichia coli, using two-dimensional heteronuclear NMR techniques. Protein Sci *2*, 543-558.

Rathinavelan, T., Zhang, L., Picking, W.L., Weis, D.D., De Guzman, R.N., and Im, W. (2010). A repulsive electrostatic mechanism for protein export through the type III secretion apparatus. Biophys J *98*, 452-461.

Rodnin, M.V., Kyrychenko, A., Kienker, P., Sharma, O., Posokhov, Y.O., Collier, R.J., Finkelstein, A., and Ladokhin, A.S. (2010). Conformational switching of the diphtheria toxin T domain. Journal of Molecular Biology *402*, 1-7.

Ronald, P.C., Salmeron, J.M., Carland, F.M., and Staskawicz, B.J. (1992). The cloned avirulence gene avrPto induces disease resistance in tomato cultivars containing the Pto resistance gene. Journal of Bacteriology *174*, 1604-1611.

Salmeron, J.M., Oldroyd, G.E., Rommens, C.M., Scofield, S.R., Kim, H.S., Lavelle, D.T., Dahlbeck, D., and Staskawicz, B.J. (1996). Tomato Prf is a member of the leucine-rich repeat class of plant disease resistance genes and lies embedded within the Pto kinase gene cluster. Cell *86*, 123-133.

Shan, L., He, P., Zhou, J.M., and Tang, X. (2000a). A cluster of mutations disrupt the avirulence but not the virulence function of AvrPto. Molecular Plant-Microbe Interactions *13*, 592-598.

Shan, L., Thara, V.K., Martin, G.B., Zhou, J.M., and Tang, X. (2000b). The pseudomonas AvrPto protein is differentially recognized by tomato and tobacco and is localized to the plant plasma membrane. The Plant Cell *12*, 2323-2338.

Thurlkill, R.L., Grimsley, G.R., Scholtz, J.M., and Pace, C.N. (2006). pK values of the ionizable groups of proteins. Protein Sci *15*, 1214-1218.

Tollinger, M., Skrynnikov, N.R., Mulder, F.A., Forman-Kay, J.D., and Kay, L.E. (2001). Slow dynamics in folded and unfolded states of an SH3 domain. J Am Chem Soc *123*, 11341-11352.

van Dijk, K., Fouts, D.E., Rehm, A.H., Hill, A.R., Collmer, A., and Alfano, J.R. (1999). The Avr (effector) proteins HrmA (HopPsyA) and AvrPto are secreted in culture from Pseudomonas syringae pathovars via the Hrp (type III) protein secretion system in a temperature- and pH-sensitive manner. J Bacteriol *181*, 4790-4797.

Wimalasena, D.S., Janowiak, B.E., Lovell, S., Miyagi, M., Sun, J., Zhou, H., Hajduch, J., Pooput, C., Kirk, K.L., Battaile, K.P., *et al.* (2010). Evidence that histidine protonation of receptor-bound anthrax protective antigen is a trigger for pore formation. Biochemistry *49*, 6973-6983.

Wulf, J., Pascuzzi, P.E., Fahmy, A., Martin, G.B., and Nicholson, L.K. (2004). The solution structure of type III effector protein AvrPto reveals conformational and dynamic features important for plant pathogenesis. Structure *12*, 1257-1268.

Xiang, T., Zong, N., Zhang, J., Chen, J., Chen, M., and Zhou, J. (2010). FLS2, but not BAK1, is a target of the Pseudomonas syringae effector AvrPto. Molecular plant-microbe interactions.

Xing, W., Zou, Y., Liu, Q., Liu, J., Luo, X., Huang, Q., Chen, S., Zhu, L., Bi, R., Hao, Q., *et al.* (2007). The structural basis for activation of plant immunity by bacterial effector protein AvrPto. Nature *449*, 243-247.

Yang, A.S., and Honig, B. (1994). Structural origins of pH and ionic strength effects on protein stability. Acid denaturation of sperm whale apomyoglobin. Journal of Molecular Biology *237*, 602-614.

Yeam, I., Nguyen, H.P., and Martin, G.B. (2010). Phosphorylation of the Pseudomonas syringae effector AvrPto is required for FLS2/BAK1-independent virulence activity and recognition by tobacco. Plant J *61*, 16-24.

Zhang, J., Lu, H., Li, X., Li, Y., Cui, H., Wen, C.-K., Tang, X., Su, Z., and Zhou, J.-M. (2010). Effector-triggered and pathogen-associated molecular pattern-triggered immunity differentially contribute to basal resistance to Pseudomonas syringae. Molecular plant-microbe interactions : MPMI *23*, 940-948.

CHAPTER 3

A PH-REGULATED FOLDING SWITCH IN *PSEUDOMONAS SYRINGAE* EFFECTOR PROTEIN AVRPTO MODULATES ITS TRANSLOCATION VIA THE TYPE III SECRETION SYSTEM·

Introduction

Gram-negative phytopathogenic bacteria have evolved the type III secretion system (T3SS) as a major virulence determinant. The T3SS enables pathogens to subvert host cell functions while remaining extracellular and thereby suppress the first level of the eukaryotic host cell defense, pathogen-associated molecular pattern (PAMP)-triggered innate immunity (PTI) (Galán and Wolf-Watz, 2006). The T3SS spans both bacterial membranes, extends through the extracellular space via a needle-like protrusion (pilus) that is tipped with a host membrane translocon, and thus provides a direct conduit for bacterial effector protein delivery. Once translocated into the host cytoplasm through the T3SS, bacterial effectors carry out virulence functions for the benefit of the bacterium. The inner diameter of the T3SS nanosyringe is approximately 2–3 nm based on electron microscopy data, necessitating at least a partial unfolding of the passing effectors (Daniell et al., 2003; Hoiczyk and Blobel, 2001). Due to its requirement for ATPase activity, T3SS function requires a transmembrane proton gradient, resulting in a variation in the pH environment experienced by the translocated proteins (Alder and Theg, 2003).

· Šečkutė, J.; Dawson, J.E.; Sosa, M.; Kvitko, B.H.; Collmer, A.; Nicholson, L.K. A pH-regulated folding switch in *Pseudomonas syringae* effector protein AvrPto modulates its translocation via the Type III Secretion System. *Manuscript in submission.*

The plant host cell is expected to maintain its intracellular pH at ~7.4, while the plant apoplast is acidic at as low as pH 5 (Grignon and Sentenac, 1991). Work in *Yersinia* has shown the proton motive force requirement for the T3SS function (Wilharm et al., 2007). However, the dependence of T3S effector translocation on intracellular bacterial pH is not known. Variation in pH between the bacterial and host cell cytoplasms may select for low stability effector protein structures capable of unfolding at a mildly acidic pH threshold inside the bacterium to facilitate T3SS-dependent delivery, and refolding at neutral pH inside the host cell where tertiary structure is required for function.

One well-studied effector protein that is translocated via the T3SS is a *Pseudomonas syringae* effector AvrPto, an 18-kDa protein with a folded core at neutral pH (Wulf et al., 2004; Xing et al., 2007). The virulence role of AvrPto lies in its interaction with plant receptor kinases at the plasma membrane and prevention of PTI (Dodds and Rathjen, 2010; Hauck et al., 2003), as well as unknown C-terminal phosphorylation-dependent interactions (Yeam et al., 2010). AvrPto has been shown to bind the kinase domain of FLS2, inhibiting the formation of FLS2-BAK1 complex which is required for the initiation of PTI (Xiang et al., 2010). In resistant plants, AvrPto is recognized by the avirulence role mediated by its recognition by the plant serine/threonine kinase Pto (Scofield et al., 1996; Tang et al., 1996). Pto is a molecular decoy for AvrPto according to the "guard" hypothesis, where plant resistance is imparted through the indirect activation of the resistance (R) protein Prf following Pto's association with AvrPto (Van der Biezen and Jones, 1998; van der Hoorn and Kamoun, 2008; Xing et al., 2007). Direct binding of Pto to AvrPto releases the negative Pto regulation on Prf, an associated plant

nucleotide-binding leucine-rich repeat R protein that initiates the downstream resistance pathways.

AvrPto adopts a structured core of three amphipathic α-helices with a small orthogonal α-helix and an omega loop that forms critical interactions with Pto (Wulf et al., 2004; Xing et al., 2007). The hydrophobic core at the helical interface is networked by the single centrally-buried tryptophan, flanked by two tyrosine rings and aliphatic side chains to form an aromatic network. AvrPto features low stability and possesses a specialized capacity to unfold during translocation and subsequently refold in the host by the action of a single buried histidine (His 87) out of its total of eight dispersed histidine residues (Figure 3.1A) (Dawson and Nicholson, 2008; Dawson et al., 2009). This folding switch, encoded in the structure of AvrPto by the placement of a single residue, acts in the pH range expected for the biological system and is predicted to govern AvrPto translocation efficiency (Chapter 2).

We present here the thermodynamic and functional consequences, in terms of both folding energy and T3SS translocation and secretion efficiency, of the removal of the His 87 folding switch in AvrPto. The pH-dependence of thermal denaturation is compared for WT and H87Y mutant constructs of the truncated helical core of AvrPto (TrAvrPto, a.a. 29–133). The fold stability at neutral pH was determined for both WT and H87Y AvrPto by hydrogen-deuterium exchange (HDX), demonstrating that the H87Y substitution imparts a small stabilization relative to WT TrAvrPto when H87 is deprotonated. Translocation efficiencies from *Pseudomonas syringae* pv tomato (*Pst*) DC3000 into domestic tobacco *Nicotiana tabacum* during the initial time course (first 5.5 hours) of infection were compared for WT and H87Y in full-length AvrPto fused to the adenylase cyclase (Cya) reporter protein.

Comparative efficiencies of WT and H87Y AvrPto-Cya expression in DC3000 are similar to those of WT and H87Y AvrPto (lacking the C-terminal Cya fusion partner), demonstrating that Cya does not alter the amount of effector available for passage through the T3SS. Our results show that removal of the pH folding switch from AvrPto both shifts the acid denaturation to lower pH *in vitro* and decreases translocation efficiency *in planta*.

Results

The H87Y mutant of AvrPto stabilizes the AvrPto fold in a pH-dependent manner. Preservation of the TrAvrPto fold in the H87Y mutant is indicated by the minimal changes observed in the ^{15}N-^{1}H fHSQC spectrum (Figure 3.1B). WT and H87Y TrAvrPto stabilities were first measured using HDX at pD 7.2, where the His 87 is predominantly in the neutral form (99.6% neutral given its pK_a of 4.8). This pH value was chosen to avoid free energy contribution from His 87 titration, thereby providing a direct comparison of fold stability. For both WT and H87Y TrAvrPto, the decay of peak intensities as a function of time were fit to yield individual observed exchange rates (k_{ex}^{obs}) (Figure 3.1C-D), yielding residue-specific protection factors and the corresponding free energies.

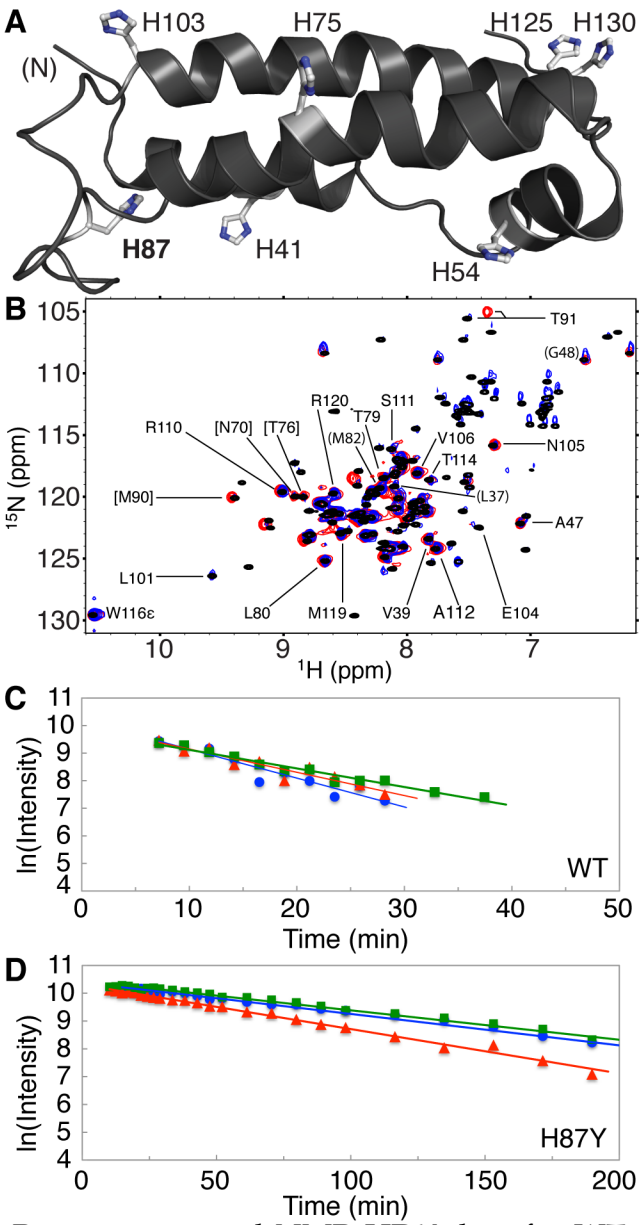

Figure 3.1. TrAvrPto structure and NMR HDX data for WT and H87Y at pD 7.2. (A) WT TrAvrPto structure ribbon diagram (PDB ID 1R5E, averaged with AREAIMOL), showing seven His in ball-and-stick representation. Buried His 87 is highlighted in bold and N- and C-termini are indicated in parenthesis. (B) Overlay of WT TrAvrPto ^{15}N-^{1}H fHSQC spectrum at pH 7.0 (black), and H87Y TrAvrPto at pD 7.2 HDX ^{15}N-^{1}H fHSQC spectrum at 16.52 min (blue). Peaks used in $\Delta G_{F\rightarrow U}$ determination are labeled (peaks used for WT only in parentheses, H87Y only in square brackets). (C) Linear decay of representative peaks in WT TrAvrPto pD 7.2 HDX experiment, shown as ln(intensity) over elapsed time. Intensities were adjusted for spectra with longer nt values. Shown peaks: L80 (blue circles), V106 (red triangles), and R110 (green squares). Linear fits are shown as lines. (D) Linear decay of corresponding peaks in H87Y pD 7.2 (V106 decayed until 244.90 min, R110 until 366.65 min).

Residues that participate in hydrogen-bonding in the TrAvrPto structure, predominantly in α-helices, were the most protected and yielded similar free energies in WT TrAvrPto (4.3 ± 0.5 kcal/mol), showing that the HDX for these residues reflects global unfolding. Residues used in the free energy calculation (Equation 3.1) in WT TrAvrPto were L37, V39, A47 (α-helix 1), G48 (loop), T79, L80, M82 (α-helix 2), M90, T91 (turn), L101, N105, V106, R110, S111, A112, T114, W116 εN-H, M119, R120 (α-helix 2). Intrinsic k_{ex} value (k_{ex}^{int}) for the well-resolved Trp 116 indole amine (Figure 3.1B) was taken as a known free peptide rate constant at 278 K and used without extrapolation (Bai et al., 1993).

Likewise, the most protected residues in H87Y TrAvrPto displayed free energies similar to each other (5.1 ± 0.6 kcal/mol), but higher than for WT TrAvrPto. Residues used in the free energy determination of H87Y TrAvrPto were the same as for WT except L37, G48, and M82 were not used due to spectral overlap, and N70, T76, and M90 were included. These results demonstrate that the overall fold stabilization imparted by the H87Y mutation at pD 7.2, 0.8 ± 0.8 kcal/mol, is relatively small.

The relative denaturation free energies of WT and H87Y TrAvrPto were also determined at a slightly acidic pH. H87Y TrAvrPto was denatured with guanidine hydrochloride (GuHCl) at pH 6.2 and 22 °C (Figure 3.2). H87Y TrAvrPto was unfolded with the midpoint of stability (where $\Delta G_{F\rightarrow U} = 0$) of 1.4 M GuHCl, with the resultant $\Delta G_{F\rightarrow U}$ of 3.9 kcal/mol. This $\Delta G_{F\rightarrow U}$ was calculated by extrapolation from the intercept of the denaturing region to native conditions where [GuHCl] = 0 M and the protein is fully loaded (Figure 3.2A). WT TrAvrPto $\Delta G_{F\rightarrow Ucalc}$ at 6.2 and 22 °C was determined to be 1.6 kcal/mol (calculated from the

fitted acid denaturation curve in Figure 3.2C), resulting in an increase in stability of 2.3 kcal/mol imparted by the removal of buried His 87, at slightly acidic conditions.

To further investigate the pH-dependent stability of H87Y TrAvrPto at different temperatures, the thermal denaturation of this mutant was measured using Trp fluorescence (Fl) at pH 2.6–7.1 (Figure 3.2B). The population of unfolded protein (p_U) was also measured in this pH range at 26.6 °C using ^{15}N-^{1}H fHSQC NMR (Figure 3.2C), confirming the global 2-state unfolding of the H87Y mutant. The Fl thermal denaturation data spanning ~5–70 °C allows the acid denaturation plot (p_U versus pH) to be constructed at any temperature in the measured range, and thereby provides insight into pH-dependence of p_U at a given temperature. Construction of this plot at 26.6 °C agrees well with the acid denaturation curve obtained by NMR (Figure 3.2C). Acid denaturation plots were also constructed in this manner for both WT and H87Y at 15, 22, and 30 °C for comparison with *in planta* translocation assays carried out at these temperatures as described below.

Figure 3.2. TrAvrPto denaturation curves, and the resulting p_U over pH from Fl and NMR experiments. (A) GuHCl equilibrium denaturation experiment data at pH 6.2, indicating the calculated p_U values as a function of the denaturant concentration, and the corresponding free energy of unfolding values in the unfolding transition region. Data trendline was used to extrapolate the $\Delta G_{F \rightarrow U}$ in the absence of GuHCl. (B) TrAvrPto temperature unfolding, as reported by the W116, shifts to higher temperatures as a function of pH. WT and H87Y temperature unfolding behavior is compared, where black circles are pH 4.40 and 4.32, respectively. Red circles are shown to compare pH 5.41 and 5.35, respectively, and black triangles are WT pH 7.09 and H87Y pH 7.14. The rest of the data is shown, in the case of WT Fl, for pH 4.00 (in orange), 4.20 (brown), 4.85 (blue), and 6.13 (green). H87Y Fl experiments are shown for pH 2.62 (in purple), 2.76 (teal), 3.08 (light blue), 3.14 (orange), 3.34 (brown), 3.48 (blue), and 6.15 (green). (C) TrAvrPto p_U versus pH shows a shift of the acid denaturation curve by almost 2 pH units to lower pH for the H87Y mutant relative to WT. NMR data for H87Y (black circles) and WT (gray) represent averages over multiple residues as described in Material and Methods. Error bars are the standard deviation in p_U as determined for each residue, and are in general smaller than the data point symbols. The WT data fit is shown as a line, emphasizing the shift in the unfolding pH region induced by the mutation (Chapter 2). H87Y Fl p_U values at the NMR temperature of 26.6 °C is plotted as horizontal bars with the standard deviation calculated from an estimate for the temperature error during the experiment of 0.2 °C, and subsequent error propagation in the calculation of p_U.

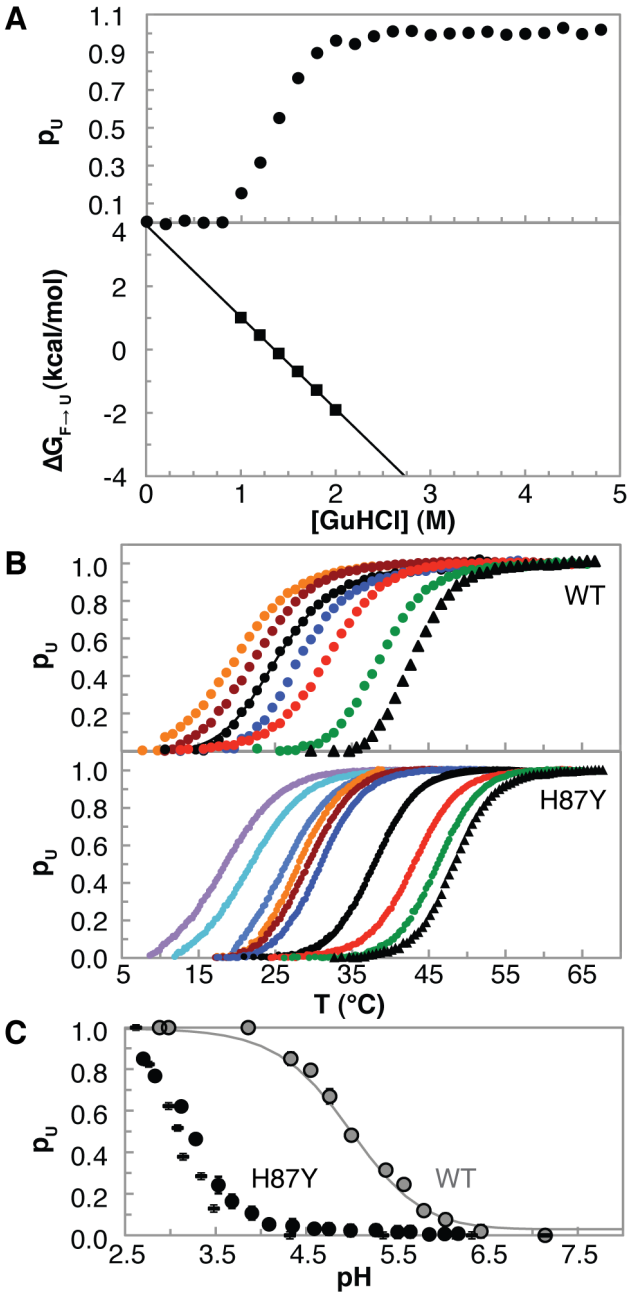
A
1.1
0.9
0.7
0.5
0.3
0.1
p_U
4
2
0
-2
-4
$\Delta G_{F\rightarrow U}$ (kcal/mol)
0
1
2
3
4
5
[GuHCl] (M)
B
1.0
0.8
0.6
0.4
0.2
p_U
WT
1.0
0.8
0.6
0.4
0.2
0.0
p_U
H87Y
5
15
25
35
45
55
65
T (°C)
C
1.0
0.8
0.6
0.4
0.2
0.0
p_U
H87Y
WT
2.5
3.5
4.5
5.5
6.5
7.5
pH

***AvrPto structural stability directly correlates with translocation efficiency* in planta**. In a time-resolved study in enteropathogenic *Escherichia coli*, effectors show distinctive T3SS-dependent translocation profiles and order, indicating that effector delivery into host cells is regulated in terms of timing and amount (Mills et al., 2008). In order to measure the initiation of AvrPto translocation and effector levels in plant cells over time, we used a Cya reporter assay. CyaA from *Bordetella pertussis* was fused to full-length AvrPto in a broad host range plasmid and transformed into DC3000 cells that were used to infiltrate the leaves of *N. tabacum*, a non-host of *P. syringae* pv tomato that exhibits a hypersensitive response, visible in ~24 h (data not shown). C-terminal Cya fusion does not inhibit translocation into *N. tabacum* cells, where upon delivery cAMP is produced by calmodulin-dependent cyclization of AMP (Figure 3.3) (Sory and Cornelis, 1994). Lacking a bacterial source of calmodulin, the detection of cAMP reporter in this assay directly correlates with the translocated amount of AvrPto-Cya construct, and has been successfully used to detect effector translocation (Mukaihara and Tamura, 2009; Schechter et al., 2004; Schechter et al., 2006).

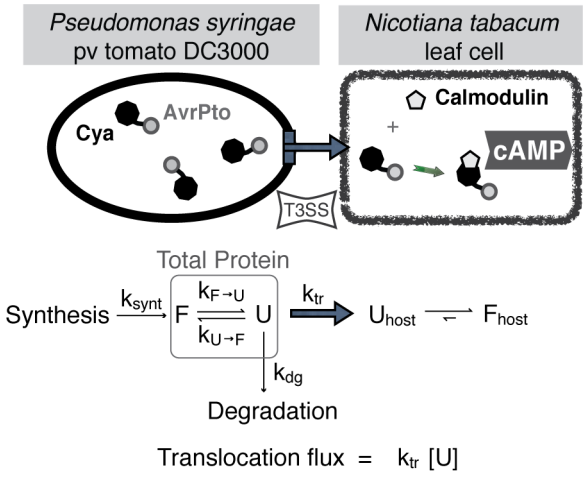

Figure 3.3. Full-length AvrPto *in planta* translocation scheme. AvrPto-Cya protein fusion is translocated into the infected plant cell via the T3SS machinery, where, in the presence of calmodulin, molecules of cAMP are produced over time. The fate of AvrPto depends on the rate of its synthesis (k_{synth}), the equilibrium between the folded (F) and unfolded (U) forms, and the resulting degradation (k_{dg}) of U or translocation (k_{tr}) into the host cell with subsequent refolding and function. Therefore, the translocated protein flux is a product of the rate of translocation and the concentration of U in the bacterial cell. Total protein present in the bacterial cell (F + U in equilibrium) is highlighted.

In order to investigate the comparative translocation efficiencies of WT and H87Y AvrPto-Cya, corresponding plasmids were transformed into DC3000wt, DC3000Δ*avrPto*Δ*avrPtoB* and the negative control strain CUCPB5112 (DC3000 Δ*hrcC*:*Kan*^{R}:*Rif*^{R}). The DC3000 CUCPB5112 lacks the conserved core T3SS structural component, the outer membrane secretin protein HrcC, resulting in a non-functional T3SS (Schechter et al., 2004). To confirm consistently similar levels of WT and H87Y AvrPto-Cya fusion proteins independent of endogenous AvrPto and AvrPtoB, immunoblot analysis was used. DC3000 cells were separated on an SDS-PAGE gel after growth in *hrp*-derepressing minimal medium and visualized with anti-AvrPto antibody. At 22 °C, similar amounts of WT and H87Y AvrPto-Cya were expressed at both early and late time points (Figure 3.4A,B). Furthermore, the relative expression levels of WT and H87Y AvrPto-Cya are insensitive to a moderate increase in temperature, with comparable total protein amounts of WT and H87Y at 30 °C (Figure 3.4C). As expected, levels of both WT and H87Y build up in the cell over time, as visualized at 2.5 and 5.5 h (Figure 3.4B). WT AvrPto-Cya was present in the negative control strain CUCPB5112 (Figure 3.4A), validating its use as a negative control strain *in planta* where no Cya was detected in the plant cells at the CUCPB5112 inoculation sites. Anti-Cya antibody was used to confirm the detection of AvrPto-Cya fusion product (data not shown). These results demonstrate that any significant differences in the translocation efficiency observed between WT and H87Y AvrPto-Cya are not due to different expression levels of the two proteins.

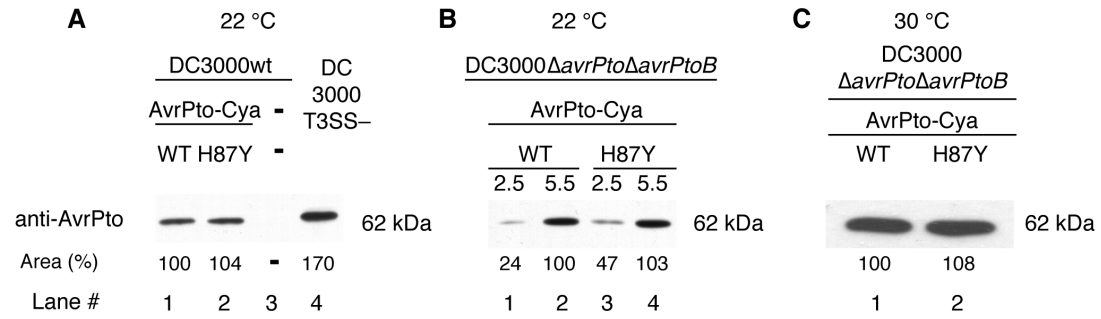

Figure 3.4. WT and H87Y AvrPto-Cya construct expression level comparison in DC3000 in minimal medium. Immunoblot analysis was performed on DC3000 cells grown under *hrp*-derepressing minimal medium conditions. Cultures were grown for 6 h unless indicated otherwise. This amount of time was selected to provide direct comparison to AvrPto-Cya expression during translocation, which was monitored for up to 5.5 h. Cultures were centrifuged to pellet the cellular fractions. The amount of cells in each set of experiments was normalized by OD_{600}. OD_{600}-based cell amount adjustment was confirmed by probing the same gels with anti-NPTII antibody (29 kDa lanes, data not shown). No AvrPto-Cya or indication of cell lysis by NPTII was observed in the supernatant fractions at this timeframe (data not shown). The cellular fractions were successfully imaged using anti-AvrPto antibody (and confirmed with probing with anti-Cya antibody, data not shown). The corresponding molecular weights are indicated by each section. Resulting images were analyzed using ImajeJ 1.43. (A) DC3000wt cells containing plasmid pCPP5811 expressing AvrPto-Cya (62 kDa lanes 1, 2), not containing pCPP5811 (lane 3) were grown at 22 °C. CUCPB5112 strain containing the pCPP5811 WT AvrPto-Cya plasmid was used as a negative secretion control (lane 4). ImageJ-analyzed area of each band (lane 1: 1002 pixels [px], 2: 1040 px, 4: 1699 px) is denoted as % WT amount from lane 1. (B) DC3000Δ*avrPto*Δ*avrPtoB* cells were used at 22 °C as in (A), and OD_{600}-adjusted cellular fraction samples show AvrPto levels at 2.2 and 5.5 h. The increase in the protein amount was calculated using ImageJ (lane 1: 316 px, 2: 1314 px, 3: 618 px, 4: 1350 px) and is shown as % of WT amount from lane 2. (C) Similarly, DC3000Δ*avrPto*Δ*avrPtoB* cells were grown at 30 °C for 6 h and cellular band areas were calculated for lane 1: 4839 px, 2: 5206 px.

Measurements of cAMP levels in inoculated plant leaf samples over time were done in parallel for WT and H87Y AvrPto-Cya in DC3000wt and for WT AvrPto-Cya in CUCPB5112. Both constructs were delivered into eukaryotic host cells in a T3SS-dependent manner, as the presence of cAMP was absent in the negative control strain and detected typically ~2 h postinoculation with DC3000 carrying AvrPto-Cya. Levels of cAMP were monitored every 0.5 h for the following 3.5 h when the biggest increases in the cAMP reporter levels were observed in DC3000wt in the temperature range studied (Figure 3.5A). For the CUCPB5112 carrying WT AvrPto-Cya, cAMP levels were consistently below ~1 pmol cAMP/μg protein level and was measured at 5.5 h endpoint for each experiment (data not shown). Since AvrPto-Cya expression in CUCPB5112 was unimpaired (Figure 3.4A), these results confirm that the measured cAMP levels in secretion-competent DC3000 were in direct relationship to the amount of translocated protein of interest.

Translocated WT and H87Y AvrPto-Cya levels are sensitive to temperature, but to a different extent. Previously, the highest AvrPto levels secreted into culture medium were measured at 22 °C, and no secretion at 30 °C was observed by immunoblotting, while AvrPto was present in the bacterial cells (van Dijk et al., 1999). Likewise, our results show the highest overall levels of translocated AvrPto-Cya (above 150 pmol cAMP/μg protein) at 22 °C (Figure 3.5A). However, we detected significant cAMP levels in translocation assays at 30 °C, in contrast to the previously published secretion data in *hrp*-derepressing minimal medium, which involved a different strain, *P. syringae* pv *syringae* 61 (van Dijk et al., 1999). This increase in cAMP levels is expected given the increase in p_U as a function of temperature that drives the translocated protein flux, assuming a constant translocation rate, k_{tr} (Figure 3.3), for both WT and H87Y AvrPto. At all three

temperatures studied, 15, 22, and 30 °C, WT exceeded H87Y AvrPto-Cya translocated protein levels, with the largest difference at 30 °C that decreased with temperature (Figure 3.5B).

Overall AvrPto-Cya levels increased for up to ~5 h post inoculation at 15 and 22 °C for both WT and H87Y constructs. At 30 °C the measurements were more variable but did not show an increasing trend past the initial 3 h post inoculation. This increased variability may be the result of the temperature-affected plant responses, like the increased stress on the plants, a non-uniform change in plant immune response, affected area wound response after sample harvesting at each time point, or possible wounding influence on intracellular calmodulin and calcium levels (required for calmodulin binding to Cya) (Hong-Bo et al., 2008; Shen et al., 2002).

Figure 3.5. Unfolded protein fraction variation with pH *in vitro* correlate with AvrPto translocation efficiency *in planta*. (A) Full-length AvrPto translocation data obtained from plant samples fully equilibrated to 15, 22, and 30 °C shows the differences in the translocation efficiency of AvrPto WT and H87Y at early infection time course. Standard deviation is shown from the experiments done in triplicate, reflecting the data averaging over two leaves on two different plants. (B) Differences in full-length AvrPto translocation efficiency at 15, 22, and 30 °C experiments are expressed as the difference between the WT and H87Y measurements, summed over each time point shown in (A). (C) Unfolded protein (p_U) Fl data for WT and H87Y TrAvrPto extracted from the temperature denaturation curves (Figure 3.2B) at three temperature values: 15, 22, and 30 °C. Unfolded fractions were calculated at each temperature by linear extrapolation between the two closest collected data points in each Fl denaturation curve. Actual data is shown for WT as black-lined open diamonds, and H87Y as black circles. Corresponding curves are Hill-equation fits to each dataset in order to better illustrate the differences in the pH regions of protein unfolding. (D) Differences between the amount of unfolded TrAvrPto WT and H87Y vary over the pH range of unfolding. Actual data points, collected around pH values of 6.1, 5.4, and 4.4 were used to calculate Δp_U between WT and H87Y Fl data in (C). The fraction of the difference in p_U is shown normalized to the 30 °C data at pH 5.4. No significant difference in the unfolding of TrAvrPto WT or H87Y above pH 6 is observed.

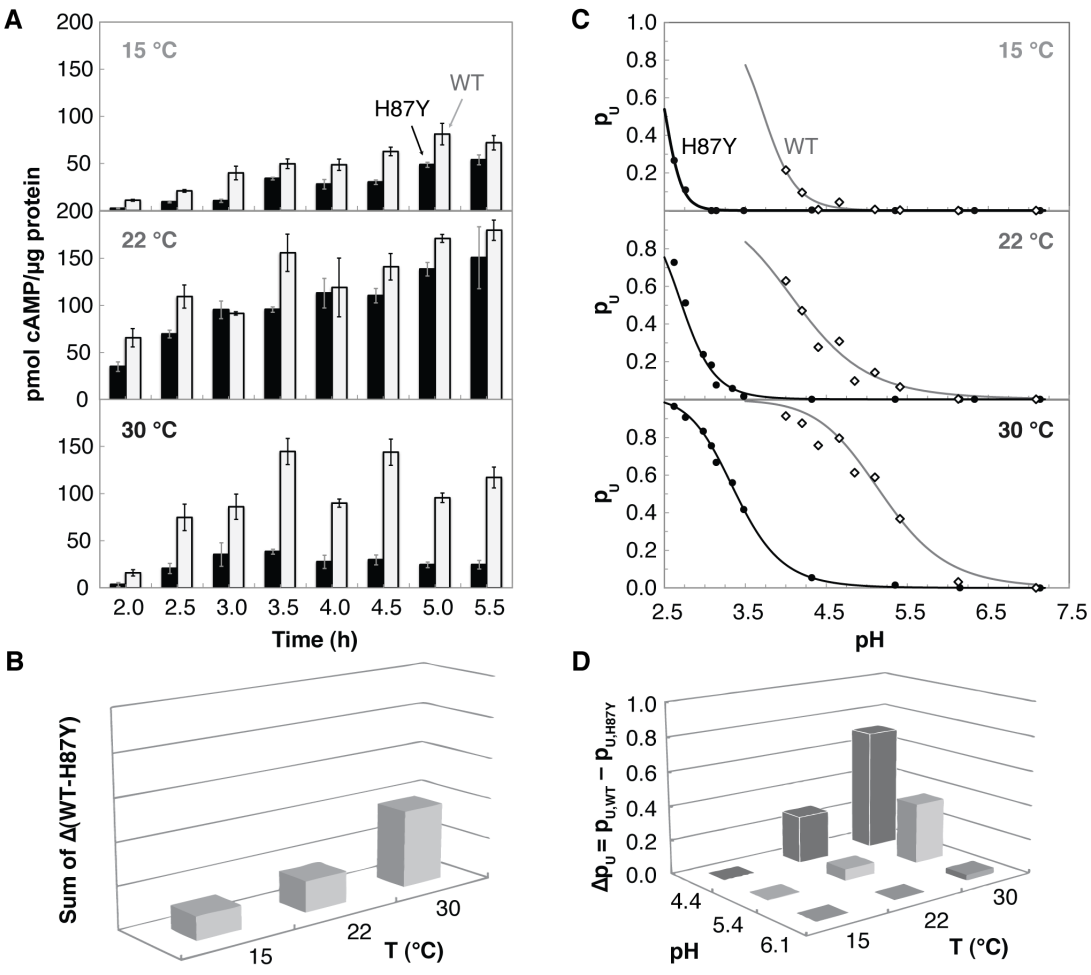
A
15 °C
22 °C
30 °C
H87Y
WT
pmol cAMP/µg protein
Time (h)
B
Sum of Δ(WT-H87Y)
T (°C)
C
15 °C
22 °C
30 °C
H87Y
WT
pH
D
pH
T (°C)

Thermal denaturation characteristics and* in planta *translocation efficiencies of WT versus H87Y AvrPto, taken together, suggest an upper limit of bacterial intracellular pH. Full-length AvrPto translocation studies enabled a direct measure of the impact of the His87-governed pH-folding switch on the delivery of AvrPto. Since AvrPto is translocated in its unfolded form due to T3SS channel restrictions (Feldman et al., 2002; Schechter et al., 2004), and does not have a known chaperone (Losada and Hutcheson, 2005), the equilibrium amount of unfolded AvrPto present in the bacterial cell at a given pH should drive the translocation process as long as the rate of AvrPto unfolding is not rate-limiting (Figure 3.3). Given the half-life of AvrPto in DC3000wt of 8 min (Losada and Hutcheson, 2005) and the TrAvrPto unfolding rate at pH 6.1 of 0.33 s^{-1} (Dawson and Nicholson, 2008), the unfolded intracellular population of AvrPto in DC3000wt is expected to be accumulating in mildly acidic conditions (as seen in Figure 3.4B). Therefore, the differences in the translocation efficiency between the WT AvrPto and H87Y mutant reported here directly reflect the equilibrium amounts of the unfolded protein available for translocation at the temperature and pH of the cell environment.

The unfolding behavior of AvrPto is determined by the stabilizing forces of its structured core of three parallel helices with connecting loops and a small orthogonal helix. This structured region of AvrPto corresponds to the central two thirds of the total protein sequence (residues 29–133), and is flanked by disordered N- (28 residues) and C-termini (31 residues). Therefore, it is reasonable to compare the differences in WT and H87Y TrAvrPto unfolded populations (measured *in vitro* by NMR and Fl) with the differences in translocation efficiencies of full-length WT and H87Y AvrPto-Cya

(measured *in planta* using the cAMP assay), in terms of the equilibrium amounts of unfolded protein at a given temperature and pH.

The temperature denaturation profiles obtained for WT and H87Y TrAvrPto in different pH buffers allow the acid unfolding curve for each protein to be constructed at a chosen temperature, as described above. Construction of such plots for 15, 22, and 30 °C shows that the difference in the amount of unfolded protein between WT and H87Y varies widely, with high dependence on both pH and temperature (Figure 3.5C). This difference between the two proteins is dominated by variations in the unfolded population of WT, since H87Y is predominantly folded at all three temperatures in mildly acidic or higher pH values (pH ≥ ~5.5). Assuming the bacterial intracellular pH is temperature-independent between 15–30 °C, significant differences in the amounts of unfolded WT versus H87Y TrAvrPto occur at pH values below ~6. Using Fl data points closest to three representative pH values (actual pH 4.5, 5.4, and 6.1), differences in the unfolded population were obtained (Figure 3.5D).

Similarly, the effect of H87Y mutation on translocation efficiency was estimated from the difference in cAMP levels between WT and H87Y AvrPto-Cya, summed over all time points at a given temperature. The temperature-dependent differences in translocation of the two proteins can be correlated with the increasing difference in p_U with increasing temperature. Our results show no significant variation in p_U between WT and H87Y above pH 6, while below pH 6 (as seen for pH 5.4 data in Figure 3.5D) changes in p_U with temperature can account for the translocation level variability. This suggests that the upper limit of the bacterial intracellular pH during T3SS-dependent

translocation from *Pst* DC3000 is pH ~6 in order to allow for efficient AvrPto translocation.

Discussion

Our results correlate the *in vitro* unfolding free energy modulated by His 87 and *in planta* translocation to study the influence of an effector's stability on the T3SS trafficking process. Plant-pathogen interactions are strongly affected by environmental factors like pH and temperature that can modulate pathogenicity levels as well as the host response (Garrett et al., 2006). Thermosensing is important in eubacteria, for example *P. syringae* pv glycinea PG4180 uses a temperature-sensitive histidine protein kinase to regulate the production of phytotoxin coronate (Schumann, 2007; Smirnova et al., 2008). Among the many facets of plant-pathogen interactions affected by temperature, which includes host defense (Wang et al., 2009), effector stability and translocation efficiency have received little attention. We report here a decrease in the amount of one translocated effector, AvrPto, monitored at the onset of bacterial invasion, due to an increase in stability and altered acid-denaturation behavior imparted by the H87Y mutation. Differences in translocation efficiency among the pool of effectors during translocation have been observed previously (Mills et al., 2008). Our results add to the possible factors influencing overall regulation of translocation efficiency, which is strongly influenced by the stability of the individual effector structure. Since effector functions in the host cell may be coordinated, the hierarchy during translocation is an important mechanism leading to the success of pathogen survival (Ghosh, 2004).

The reduced translocation of the H87Y mutant correlates with increased fold stability and suggests that effector unfolding is not a rate-limiting step in translocation. Even though a small amount of unfolded H87Y is present at the putative intracellular bacterial pH (0.58% at 22 °C and pH 6.2, given $\Delta G_{F \rightarrow U}$ of 3.9 kcal/mol), this mutant is still translocated relatively well. WT AvrPto is estimated to be 6.0% unfolded and is translocated more readily during the same timeframe (given $\Delta G_{F \rightarrow U}$ of 1.6 kcal/mol at pH 6.2). Hence, even a small amount of unfolded protein will compete for T3SS entry and is readily replenished to maintain flux into the host cell. However, as p_U is directly proportional to the translocation flux, a larger pool of unfolded protein results in higher translocated protein levels (Figure 3.3). This indicates that the unfolding rate of the mutant is faster than the translocation rate, i.e. the rate-limiting step in the overall translocation process is not the unfolding rate of the WT or H87Y AvrPto.

AvrPto is an example of a protein where the unfolded form is a functional state that relies on the specifically tuned histidine properties. Histidine sidechains respond to the flux of H^+ ions by changing their protonation state in the mildly acidic pH region, making them suitable for generating conformationally distinct functional bias in macromolecular structures. Histidine protonation is affected by the imidazole ring packing and coordination with surrounding groups in its neutral and imidazolium states (Fernández-Recio et al., 1997). We observed a range of histidine pK_a values in AvrPto, where the most significant outlier His 87 imparts the pH-folding switch, important in furthering the efficiency of effector delivery into the host cells. Various structural pH-induced switches that are mediated by histidine protonation have been reported. An example of a distinct yet similarly

governed histidine role is hypothesized to be involved in cell protection in the context of ion gate closing in acidic pH upon histidine protonation (Yildiz et al., 2006). Two conformations of an outer membrane porin OmpG from *E. coli* have been characterized by X-ray crystallography and show a rearrangement of a loop that closes the aqueous pore in acidic pH through the repulsive action of two neighboring protonated histidines that results in hydrogen-bond breakages and loop extension. This possible mechanism of ion gating does not appear to be conserved among other outer membrane porin families (Törnroth-Horsefield and Neutze, 2008). Yet another channel acidity sensor that is encoded by titratable histidines acts to close ROMK channels at mildly acidic pH or increased CO_2 concentrations (Chanchevalap et al., 2000).

Another distinct example of the role of functional histidine protonation is the release of delivered low density lipoprotein receptors (LDLR) by receptor-associated protein (RAP) into the acidic *medial*-Golgi (pH ~6) upon delivery from pH-neutral ER (Chan et al., 2006), that does not require the typical participation of LDLR β-propeller domain (Fisher et al., 2006; Lee et al., 2006). This step in receptor recycling and LDLR trafficking and protection from degradation or premature association with other binding partners relies on RAP histidine sidechains at the binding interface (Lee et al., 2006). Also, RAP D3 domain reversibly denatures below pH 6, consistent with the single buried histidine in the structure (Table 3.1), in direct analogy to the role of buried histidine in AvrPto (Table 2.3). Key histidine residues have been implicated in the regulation of ligand release following endocytosis in several cases (Doi et al., 1994; Wragg and Drickamer, 1999; Yamamoto et al., 2008). It is intriguing to consider how histidine-dependent pH-sensing functionality seems to have coevolved independently to enable uniquely adapted

specialized transformations while utilizing the general thermodynamic principles of histidine charge tuning.

Table 3.1. Accessible surface area of histidine residues in a structurally-homologous RAP (PDB ID 2FTU, chain A) that contains similarly high number of His (9 residues out of 118, 7.6%) as AvrPto, with no sequence similarity. RAP and TrAvrPto share a similar helical bundle arrangement with the RMSD of 11.1 Å of backbone atoms (calculated with PyMol). RAP residue surface area was calculated as for TrAvrPto (Table 2.3). Briefly, CCP4 6.1 program AREAIMOL was used with probe solvent molecule of radius 1.4 Å and sampling 10 surface points per $Å^2$, with hydrogen atoms excluded. Total accessible surface area for comparison is given in parentheses. The most highly buried His 52 is highlighted, and histidines are arranged in order of increasing solvent-accessible surface area.

Protein construct (total surface area, $Å^2$)	**Residue**	**No.**	**Surface area ($Å^2$)**
RAP (8,671.9 $Å^2$)	**His**	**52**	**2.7**
	His	85	39.3
	His	63	66.7
	His	102	73.5
	His	115	89.7
	His	54	112.4
	His	68	116.4
	His	44	139.0
	His	4	149.2

Interestingly, it has been shown that plant host defenses are suppressed at moderately high temperatures at both basal and R-gene resistance levels (Wang et al., 2009). The authors report lower *Pst* DC3000 growth density at 28 °C versus the optimal temperature of 22 °C, evident after approximately 20 hours of growth. Hypersensitive response (HR) was present in *Nicotiana benthamiana* (wild tobacco plants) at 22 °C and was slow or not present at 28 and 30 °C. This optimization of plant resistance at 22 °C might reflect coevolution with pathogens that have adapted to translocated effector proteins at the highest levels around 22 °C, as seen in our results.

We correlated the variation in unfolded protein population over temperature between WT and H87Y AvrPto with their T3SS translocation in order to deduce the relationship between protein stability and translocation efficiency. Our results point to bacterial intracellular conditions maintained at or below pH 6 in order to account for observed temperature dependence of the differences between translocated WT and H87Y AvrPto levels. We note that the optimal translocation temperature of 22 °C correlates well with the previously reported highest host defense responses at that temperature (Wang et al., 2009). In this study, we used heat as an environmental variable to investigate the intracellular pH conditions that facilitate effector traffic through the T3SS, and we utilized a pH-governed folding switch in the AvrPto effector as a way to approximate the bacterial cytoplasmic pH. These results implicate protein stability as an important regulating aspect of effector translocation hierarchy and efficiency, which is necessary for the success of the bacterial invasion and proliferation.

Materials and Methods

Plasmids, cell strains and media conditions. TrAvrPto plasmids were constructed in pQE-9 vector (Qiagen) carrying the ampicillin resistance cassette and an N-terminal His_6 tag, followed by a 3cPro protease from a picornavirus cleavage site with the recognition sequence EVLFQ|GP (cleavage site indicated with a vertical dash). H87Y mutagenesis was carried out previously (see Chapter 2). Cell strain for growth and overexpression of pQE-9 plasmids was *E. coli* M15 (Qiagen). Full-length WT AvrPto-Cya and H87Y AvrPto-Cya constitutively-expressed plasmids using NPTII promoter were constructed by Gateway LR recombination (Invitrogen), as previously described (Schechter et al., 2004). Briefly, pENTR-SD/D-TOPO (Invitrogen) entry clones carrying full-length WT or H87Y *avrPto* were LR-recombined with pCPP5811, a pBBRMCS-5 derived Gateway Destination vector for making P_{nptII} expressed C-terminal Cya fusions. AvrPto-Cya expression vectors were transformed into *Pst* DC3000wt (Rif^R), DC3000Δ*avrPto*Δ*avrPtoB* (Rif^R,Kan^R,$Spec^R$), and into *Pst* DC3000 T3SS-deficient negative control strain CUCPB5112 (Rif^R,Kan^R). *Pst* strains were grown on KB medium (King et al., 1954). Corresponding antibiotics were used in the following concentrations: 100 μg/mL ampicillin sodium salt, 50 μg/mL kanamycin, 10 μg/mL gentamicin sulfate, and 50 μg/mL rifampicin.

Protein overexpression and purification. TrAvrPto for NMR experiments was overexpressed in M9 minimal medium (Sambrook et al., 1989) supplemented with $^{15}NH_4Cl$ and 100 μg/mL ampicillin, and purified using Ni-NTA affinity chromatography column (Qiagen) as described

previously (Chapter 2). Unlabeled WT and H87Y TrAvrPto for Fl experiments were overexpressed in Luria Broth (LB) supplemented with glucose and metal salts with appropriate antibiotics and purified in the same way (Chapter 2). Protein samples for *in vitro* experiments were prepared in McIlvaine's buffer at 230 mM ionic strength, consisting of citric acid and dibasic sodium phosphate components (McIlvaine, 1921) with 5 mM sodium azide (Chapter 2).

NMR spectroscopy. NMR data was collected using Varian Inova 600-MHz spectrometer (Varian Instruments). The fHSQC spectra were acquired in order to obtain the unfolded population data for H87Y TrAvrPto, as described previously (Chapter 2). Residue-specific p_U values obtained from fHSQC spectral analysis were averaged for the resulting overall unfolded protein population, with small standard deviations indicating a uniform global unfolding process (Figure 3.2C). Protein samples were prepared at 0.2–1.2 mM concentration in the McIlvaine's buffer with a range of sample pH of 2.70–6.18. Data was processed using NMRPipe 5.2 (Delaglio et al., 1995) and analyzed using SPARKY 3.1 (Goddard and Kneller).

HDX measurements. Uniformly-^{15}N-labeled TrAvrPto samples in aqueous McIlvaine's buffer at pH 7 were buffer-exchanged into fully deuterated McIlvaine's buffer at pD 7.2 (pD was calculated by adjusting the pH value measured with glass electrode by +0.40) (Glasoe and Long, 1960). Zeba desalting columns (Pierce Biotechnology) were used for buffer exchange according to the manufacturer's directions, resulting in a lag time of ~5 min before the start of HDX data collection. Buffer pD stayed constant throughout

the experiment, and was checked upon experiment completion. A series of ^{15}N-^{1}H fHSQC spectra were collected at 25 °C with 2048 and 64 complex points in the t1 and t2 dimensions, respectively, while the number of transients (nt) was increased from 4 (initial 10 collected spectra) to succeeding 8, 16, 32, and 64 (last spectrum). Data was continuously collected over a total of 10 h 47 min. All spectra were processed using NMRPipe, peak intensities were obtained using SPARKY and scaled appropriately to account for different nt values. Peak intensities were fit to a straight line in the decay region as a function of time since the start of the exchange (taken as the midpoint of each experiment) in order to obtain the observed rate constant, k_{ex}^{obs}. EX2 biomolecular exchange regime was assumed, where $k_{ex}^{int} \ll k_{cl}$, the closing rate into an exchange-incompetent state, as is typical for proteins in this pH range (Bai et al., 1995; Krishna et al., 2004). Unfolding free energy $\Delta G_{F\rightarrow U}$ was calculated using the observed k_{ex}^{obs} and intrinsic k_{ex}^{int} for each residue:

$$\Delta G_{F\rightarrow U} = RT \cdot \ln\left(\frac{k_{ex}^{int}}{k_{ex}^{obs}}\right), \qquad 3.1$$

where $k_{ex}^{int}/k_{ex}^{obs}$ ratio gives a residue-specific protection factor. Individual-residue $\Delta G_{F\rightarrow U}$ values were averaged for the final overall protection value.

Tryptophan fluorescence spectroscopy. Fl data was collected using Cary Eclipse Fl Spectrophotometer (Varian Instruments). Temperature denaturation experiment samples were at about 80 μM protein concentration in McIlvaine's buffer pH range of 4.00–7.09 for TrAvrPto WT and pH range of 2.62–7.14 for TrAvrPto H87Y. Experimental setup was maintained as described previously (Chapter 2).

Guanidine hydrochloride denaturation. TrAvrPto H87Y stability was measured using guanidine hydrochloride (GuHCl) denaturation experiment by monitoring Fl emission signal in 40 μM isotopically-unlabeled TrAvrPto H87Y samples in McIlvaine's buffer at pH 6.2 with increasing GuHCl from 0 to 6 M in 0.2 M steps. GuHCl stock solution of 8 M was prepared in McIlvaine's buffer adjusted to the final pH 6.2. Total 200 μL samples were prepared in a 96-well plate, equilibrated for 1 h and measured in triplicate using Synergy HT plate reader (BioTek) with excitation set to 295 ± 5 nm and the emission filter at 340 ± 15 nm. Data in triplicate were averaged for the following calculations. Signal from a control plate of buffer and GuHCl, prepared in the same way, was subtracted from the sample plate.

For $\Delta G_{F\rightarrow U}$ calculation, the equilibrium constant of unfolding, K, was first calculated at each measured Fl data point y by:

$$K = \frac{y - y_F}{y_U - y}, \tag{3.2}$$

where y_F and y_U are the fully folded and fully unfolded protein signals, respectively, calculated for each measured GuHCl concentration. The fully folded protein signal was linearly extrapolated from the slope and intercept of the 0–0.8 M GuHCl range data, and the fully unfolded protein line from the 2.4–4.0 M GuHCl range. Equilibrium constants, calculated using Equation 3.2, were used to get $\Delta G_{F\rightarrow U}$ values:

$$\Delta G_{F\rightarrow U} = RT \cdot \ln K. \tag{3.3}$$

$\Delta G_{F\rightarrow U}$ was calculated in the GuHCl unfolding range of 1.0–2.0 M. Resulting linear equation was extrapolated to GuHCl = 0 M for the resulting $\Delta G_{F\rightarrow U}$ value. Measurements were performed at the ambient room temperature of 25 °C.

Adenylase cyclase translocation assays. For cAMP level measurements, *N. tabacum* leaves were infected with *Pst* DC3000 carrying constitutively-expressed full-length AvrPto-Cya fusion plasmids, as described previously (Schechter et al., 2004). Briefly, cells were grown into a lawn overnight at room temperature on KB plates with appropriate antibiotics, suspended at an optical density at 600 nm (OD_{600}) of 0.3, corresponding to approximately 3×10^8 CFU/mL (colony-forming units), in 5 mM 2-(*N*-morpholino)ethanesulfonic acid (MES) buffer at pH 6.5, and inoculated into plant leaves. *N. tabacum* plants used were 3–4 weeks old, and equilibrated for 2 days in a growth chamber set to 16 h daylight time and constant temperature. Relative humidity was maintained at ~80%. Leaf samples were collected with a 0.6-cm diameter cork borer, flash-frozen in liquid nitrogen and stored at -80 °C. Two samples were collected from a leaf at each time point, from each of the two plants used for an experiment.

Adenylase cyclase assay was carried out on ground leaf samples while frozen, then resuspended in 250 μL 0.1 M HCl for cell lysis. Cyclic AMP levels were assayed by following the Direct Cyclic AMP Enzyme Immunoassay Kit (Assay Designs) by following the manufacturer's directions.

Secretion assays of AvrPto-Cya in* Pst *DC3000. *Pst* DC3000 strains carrying AvrPto-Cya plasmids were grown on KB plates with appropriate antibiotics overnight to form lawns, then gently scraped off into a primary stock solution of 5 mM *hrp*-derepressing minimal medium, *hrp*MM, consisting of 40 mM potassium phosphate monobasic, 6.5 mM potassium phosphate dibasic, 7.5 mM ammonium sulfate, 1.7 mM magnesium chloride, 1.7 mM sodium chloride, with 0.2% w/w fructose, 0.18% w/w mannitol as carbon

sources, and supplemented with 50 μM iron citrate (Huynh et al., 1989). Medium pH was adjusted to 6.0 prior to the addition of antibiotics and subsequent use. Small volumes of the resulting primary high OD_{600} stock solutions were added to 100 mL *hrp*MM with appropriate antibiotics n 250-mL baffled flasks in order to start the culture growth at OD_{600} of 0.4. Cells were grown at a set incubator temperature with shaking at 225 rpm for 6 h and final OD_{600} was measured. Cell fractions were pelleted from 1.8 mL culture samples and resuspended in 200 μL sodium dodecyl sulfate (SDS) protein sample buffer containing 6 mM dithiothreitol (DTT) (Boston Bioproducts). SDS buffer amount was slightly adjusted in order to account for the final OD_{600} differences between grown culture samples. For time-resolved experiments, cellular fractions were obtained in the same fashion, and resuspended in SDS buffer adjusted according to the OD_{600} measurements at that timepoint.

Supernatant samples were obtained by centrifuging 43 mL of culture at 3,716×g for 30 min in order to separate out cellular material, and then the top 36 mL of media was centrifuged at 10,800×g for 60 min and top 30 mL supernatant was kept as the extracellular fractions, from which secreted proteins were precipitated by adding 200 μg aprotinin as a carrier protein and 3 mL trichloroacetic acid (TCA) and kept at 4 °C overnight. The resulting protein precipitants were pelleted by centrifugation at 10,800×g for 30 min, washed with cold acetone to get rid of any remaining TCA and repelleted. Final pellets were resuspended in 90 μL SDS sample buffer.

Immunoblot analysis of AvrPto-Cya expression levels in* Pst *DC3000. Protein samples were separated on 12.5% SDS-PAGE gels, electrotransferred to polyvinylidene fluoride membranes (Perkin Elmer) for ~4 h at 4 °C in Tris-

glycine buffer and blocked with Tris-buffered saline and 0.1% Tween 20 (TBST) containing 5% non-fat milk for > 1 h at room temperature. Membranes were rinsed and incubated with primary antibodies diluted in TBST containing 0.3% bovine serum albumin (BSA) for ~16 h at 4 °C at the following dilutions: rabbit polyclonal anti-AvrPto immunoglobulin G (IgG) at 1:5,000, anti-Cya 3D1 mouse monoclonal anti-AvrPto IgG at 1:2,000 (Santa Cruz Biotechnology), anti-NPTII rabbit polyclonal IgG at 1:5,000 (United States Biological). Blots were washed and probed for 2 h with either horseradish peroxidase-conjugated anti-rabbit or anti-mouse IgG at 1:10,000 dilution (Jackson ImmunoResearch Laboratories) diluted with TBST-BSA. Blots were visualized by enhanced chemiluminescence using Western Lightning kit (Perkin Elmer) according to the manufacturer's instructions and imaged using Kodak scientific imaging film.

Acknowledgements

This work was made possible by the help of Nick van Eck for the use of Cornell's Guterman Bioclimatic Laboratory growth chambers and Gary Oltz from the Ecology and Evolutionary Biology machine shop for providing the cork borers. *Pst* DC3000Δ*avrPto*Δ*avrPtoB* (Rif^R,Kan^R,$Spec^R$) strain was generously provided by Dr. Gregory Martin. Dr. Cynthia Kinsland from the Department of Chemistry and Chemical Biology provided access to the plate reader for GuHCl denaturation experiments, and Dr. Colin Parrish at the Baker Institute kindly let us use their Cary Eclipse spectrophotometer for Fl temperature unfolding studies. Ross Resnick performed the Immunoblot probing and imaging.

BIBLIOGRAPHY

Alder, N.N., and Theg, S.M. (2003). Energy use by biological protein transport pathways. Trends Biochem Sci *28*, 442-451.

Bai, Y., Milne, J.S., Mayne, L., and Englander, S.W. (1993). Primary structure effects on peptide group hydrogen exchange. Proteins *17*, 75-86.

Bai, Y., Sosnick, T.R., Mayne, L., and Englander, S.W. (1995). Protein folding intermediates: native-state hydrogen exchange. Science *269*, 192-197.

Chan, P., Lovrić, J., and Warwicker, J. (2006). Subcellular pH and predicted pH-dependent features of proteins. Proteomics *6*, 3494-3501.

Chanchevalap, S., Yang, Z., Cui, N., Qu, Z., Zhu, G., Liu, C., Giwa, L.R., Abdulkadir, L., and Jiang, C. (2000). Involvement of histidine residues in proton sensing of ROMK1 channel. J Biol Chem *275*, 7811-7817.

Daniell, S.J., Kocsis, E., Morris, E., Knutton, S., Booy, F.P., and Frankel, G. (2003). 3D structure of EspA filaments from enteropathogenic Escherichia coli. Molecular Microbiology *49*, 301-308.

Dawson, J.E., and Nicholson, L.K. (2008). Folding kinetics and thermodynamics of Pseudomonas syringae effector protein AvrPto provide insight into translocation via the type III secretion system. Protein Sci *17*, 1109-1119.

Dawson, J.E., Seckute, J., De, S., Schueler, S.A., Oswald, A.B., and Nicholson, L.K. (2009). Elucidation of a pH-folding switch in the Pseudomonas syringae effector protein AvrPto. Proc Natl Acad Sci USA *106*, 8543-8548.

Delaglio, F., Grzesiek, S., Vuister, G.W., Zhu, G., Pfeifer, J., and Bax, A. (1995). NMRPipe: a multidimensional spectral processing system based on UNIX pipes. J Biomol NMR *6*, 277-293.

Dodds, P.N., and Rathjen, J.P. (2010). Plant immunity: towards an integrated view of plant-pathogen interactions. Nat Rev Genet *11*, 539-548.

Doi, T., Kurasawa, M., Higashino, K., Imanishi, T., Mori, T., Naito, M., Takahashi, K., Kawabe, Y., Wada, Y., and Matsumoto, A. (1994). The histidine interruption of an alpha-helical coiled coil allosterically mediates a pH-dependent ligand dissociation from macrophage scavenger receptors. J Biol Chem *269*, 25598-25604.

Feldman, M.F., Müller, S., Wüest, E., and Cornelis, G.R. (2002). SycE allows secretion of YopE-DHFR hybrids by the Yersinia enterocolitica type III Ysc system. Molecular Microbiology *46*, 1183-1197.

Fernández-Recio, J., Vázquez, A., Civera, C., Sevilla, P., and Sancho, J. (1997). The tryptophan/histidine interaction in alpha-helices. Journal of Molecular Biology *267*, 184-197.

Fisher, C., Beglova, N., and Blacklow, S.C. (2006). Structure of an LDLR-RAP complex reveals a general mode for ligand recognition by lipoprotein receptors. Mol Cell *22*, 277-283.

Galán, J.E., and Wolf-Watz, H. (2006). Protein delivery into eukaryotic cells by type III secretion machines. Nature *444*, 567-573.

Garrett, K.A., Dendy, S.P., Frank, E.E., Rouse, M.N., and Travers, S.E. (2006). Climate change effects on plant disease: genomes to ecosystems. Annu Rev Phytopathol *44*, 489-509.

Ghosh, P. (2004). Process of protein transport by the type III secretion system. Microbiol Mol Biol Rev *68*, 771-795.

Glasoe, P., and Long, F. (1960). Use of glass electrodes to measure acidities in deuterium oxide. J Phys Chem-Us *64*, 188-190.

Goddard, T.D., and Kneller, D.G. SPARKY 3. University of California, San Francisco.

Grignon, C., and Sentenac, H. (1991). pH and ionic conditions in the apoplast. Annual Review of Plant Biology *42*, 103-128.

Hauck, P., Thilmony, R., and He, S.Y. (2003). A Pseudomonas syringae type III effector suppresses cell wall-based extracellular defense in susceptible Arabidopsis plants. Proc Natl Acad Sci USA *100*, 8577-8582.

Hoiczyk, E., and Blobel, G. (2001). Polymerization of a single protein of the pathogen Yersinia enterocolitica into needles punctures eukaryotic cells. Proceedings of the National Academy of Sciences of the United States of America *98*, 4669-4674.

Hong-Bo, S., Li-Ye, C., Ming-An, S., Shi-Qing, L., and Ji-Cheng, Y. (2008). Bioengineering plant resistance to abiotic stresses by the global calcium signal system. Biotechnol Adv *26*, 503-510.

Huynh, T.V., Dahlbeck, D., and Staskawicz, B.J. (1989). Bacterial blight of soybean: regulation of a pathogen gene determining host cultivar specificity. Science *245*, 1374-1377.

King, E., Ward, M., and Raney, D. (1954). Two simple media for the demonstration of pyocyanin and fluorescin. J Lab Clin Med *44*, 301-307.

Krishna, M.M.G., Hoang, L., Lin, Y., and Englander, S.W. (2004). Hydrogen exchange methods to study protein folding. Methods *34*, 51-64.

Lee, D., Walsh, J.D., Mikhailenko, I., Yu, P., Migliorini, M., Wu, Y., Krueger, S., Curtis, J.E., Harris, B., Lockett, S., *et al.* (2006). RAP uses a histidine switch to regulate its interaction with LRP in the ER and Golgi. Mol Cell *22*, 423-430.

Losada, L.C., and Hutcheson, S.W. (2005). Type III secretion chaperones of Pseudomonas syringae protect effectors from Lon-associated degradation. Molecular Microbiology *55*, 941-953.

McIlvaine, T. (1921). A buffer solution for colorimetric comparison. Journal of Biological Chemistry *49*, 183-186.

Mills, E., Baruch, K., Charpentier, X., Kobi, S., and Rosenshine, I. (2008). Real-time analysis of effector translocation by the type III secretion system of enteropathogenic Escherichia coli. Cell Host Microbe *3*, 104-113.

Mukaihara, T., and Tamura, N. (2009). Identification of novel Ralstonia solanacearum type III effector proteins through translocation analysis of hrpB-regulated gene products. Microbiology (Reading, Engl) *155*, 2235-2244.

Sambrook, J., Fritsch, E.F., and Maniatis, T. (1989). Molecular Cloning: A Laboratory Manual. Cold Spring Harbor, Laboratory Press, Cold Spring Harbor, NY *3*.

Schechter, L.M., Roberts, K.A., Jamir, Y., Alfano, J.R., and Collmer, A. (2004). Pseudomonas syringae type III secretion system targeting signals and novel effectors studied with a Cya translocation reporter. Journal of Bacteriology *186*, 543-555.

Schechter, L.M., Vencato, M., Jordan, K.L., Schneider, S.E., Schneider, D.J., and Collmer, A. (2006). Multiple approaches to a complete inventory of Pseudomonas syringae pv. tomato DC3000 type III secretion system effector proteins. Mol Plant Microbe Interact *19*, 1180-1192.

Schumann, W. (2007). Thermosensors in eubacteria: role and evolution. J Biosci *32*, 549-557.

Scofield, S., Tobias, C., Rathjen, J., Chang, J., Lavelle, D., Michelmore, R., and Staskawicz, B. (1996). Molecular basis of gene-for-gene specificity in bacterial speck disease of tomato. Science *274*, 2063-2065.

Shen, Y., Lee, Y.-S., Soelaiman, S., Bergson, P., Lu, D., Chen, A., Beckingham, K., Grabarek, Z., Mrksich, M., and Tang, W.-J. (2002). Physiological calcium concentrations regulate calmodulin binding and catalysis of adenylyl cyclase exotoxins. The EMBO Journal *21*, 6721-6732.

Smirnova, A.V., Braun, Y., and Ullrich, M.S. (2008). Site-directed mutagenesis of the temperature-sensing histidine protein kinase CorS from Pseudomonas syringae. FEMS Microbiol Lett *283*, 231-238.

Sory, M.P., and Cornelis, G.R. (1994). Translocation of a hybrid YopE-adenylate cyclase from Yersinia enterocolitica into HeLa cells. Molecular Microbiology *14*, 583-594.

Tang, X., Frederick, R., Zhou, J., Halterman, D., Jia, Y., and Martin, G. (1996). Initiation of Plant Disease Resistance by Physical Interaction of AvrPto and Pto Kinase. Science *274*, 2060-2063.

Törnroth-Horsefield, S., and Neutze, R. (2008). Opening and closing the metabolite gate. Proc Natl Acad Sci USA *105*, 19565-19566.

Van der Biezen, E.A., and Jones, J.D. (1998). Plant disease-resistance proteins and the gene-for-gene concept. Trends Biochem Sci *23*, 454-456.

van der Hoorn, R.A.L., and Kamoun, S. (2008). From Guard to Decoy: a new model for perception of plant pathogen effectors. The Plant Cell *20*, 2009-2017.

van Dijk, K., Fouts, D.E., Rehm, A.H., Hill, A.R., Collmer, A., and Alfano, J.R. (1999). The Avr (effector) proteins HrmA (HopPsyA) and AvrPto are secreted in culture from Pseudomonas syringae pathovars via the Hrp (type III) protein secretion system in a temperature- and pH-sensitive manner. J Bacteriol *181*, 4790-4797.

Wang, Y., Bao, Z., Zhu, Y., and Hua, J. (2009). Analysis of temperature modulation of plant defense against biotrophic microbes. Molecular Plant-Microbe Interactions *22*, 498-506.

Wilharm, G., Dittmann, S., Schmid, A., and Heesemann, J. (2007). On the role of specific chaperones, the specific ATPase, and the proton motive force in type III secretion. Int J Med Microbiol *297*, 27-36.

Wragg, S., and Drickamer, K. (1999). Identification of amino acid residues that determine pH dependence of ligand binding to the asialoglycoprotein receptor during endocytosis. J Biol Chem *274*, 35400-35406.

Wulf, J., Pascuzzi, P.E., Fahmy, A., Martin, G.B., and Nicholson, L.K. (2004). The solution structure of type III effector protein AvrPto reveals conformational and dynamic features important for plant pathogenesis. Structure *12*, 1257-1268.

Xiang, T., Zong, N., Zhang, J., Chen, J., Chen, M., and Zhou, J. (2010). FLS2, but not BAK1, is a target of the Pseudomonas syringae effector AvrPto. Molecular plant-microbe interactions.

Xing, W., Zou, Y., Liu, Q., Liu, J., Luo, X., Huang, Q., Chen, S., Zhu, L., Bi, R., Hao, Q., *et al.* (2007). The structural basis for activation of plant immunity by bacterial effector protein AvrPto. Nature *449*, 243-247.

Yamamoto, T., Chen, H.-C., Guigard, E., Kay, C.M., and Ryan, R.O. (2008). Molecular studies of pH-dependent ligand interactions with the low-density lipoprotein receptor. Biochemistry *47*, 11647-11652.

Yeam, I., Nguyen, H.P., and Martin, G.B. (2010). Phosphorylation of the Pseudomonas syringae effector AvrPto is required for FLS2/BAK1-independent virulence activity and recognition by tobacco. Plant J *61*, 16-24.

Yildiz, O., Vinothkumar, K.R., Goswami, P., and Kühlbrandt, W. (2006). Structure of the monomeric outer-membrane porin OmpG in the open and closed conformation. The EMBO Journal *25*, 3702-3713.

CHAPTER 4

PRELIMINARY INVESTIGATION INTO THE USE OF RATIO-GFP FOR MEASURING THE INTRACELLULAR PH IN *PSEUDOMONAS SYRINGAE*

Introduction

AvrPto is one of about 30 effectors that are exported by the Gram-negative bacterial pathogen *Pseudomonas syringae* pv tomato DC3000 (*Pst*) by direct injection into the host cell cytoplasm through the Type III secretion system (T3SS) machinery. T3SS requires an N-terminal signal sequence for targeting of effectors for translocation, and is physically restricted by the narrow inner diameter of the channel of 2–3 nm (Hoiczyk and Blobel, 2001). While macromolecular constructs that maintain their secondary structure of α-helices may be capable of traversing this channel (Rathinavelan et al., 2010), there is no evidence of a thermodynamically favorable folding intermediate in the AvrPto unfolding process (Chapter 2). We employ AvrPto as a relatively well studied model effector with a known structure in order to study the mechanism of action of the T3SS machinery during bacterial invasion. AvrPto does not have a known chaperone that may maintain the protein in its unfolded form and target it for secretion (Stebbins and Galán, 2001). Another functional advantage of the chaperone/effector complexes is the protection of unfolded effectors from premature degradation. Recent study on the dominant degradation pathway of AvrPto by the Lon protease found that the half-life of AvrPto in wild type *Pst* is 8 min (Losada and Hutcheson, 2005), which is not a rate-limiting process in maintaining the unfolded AvrPto

population in the bacterial cell given the fast truncated AvrPto (TrAvrPto, the folded α-helical core of AvrPto) unfolding (Chapter 3 and (Dawson, 2008)). Since an unfolded AvrPto pool can be maintained in the cell, our evidence points to the unfolded AvrPto population as the source of translocation-competent effector for the delivery via the T3SS into the host cell for the subsequent refolding at neutral host cytoplasm and, ultimately, virulence/avirulence roles.

In order to shift the folded/unfolded AvrPto equilibrium into the state of sufficient unfolded population, we predict that the intracellular *Pst* pH must be maintained at moderately acidic conditions during the active translocation of AvrPto. From our earlier acid denaturation elucidation of TrAvrPto *in vitro*, the unfolded population is observed at and below pH 6 at room temperature (RT) in solution (Chapter 2). In order to fully understand the minimal effector structural requirements *in vivo*, we need a way to determine the intact bacterium cellular pH while in the plant apoplast during infection, when AvrPto export occurs.

Bacteria successfully survive in a wide range of environmental conditions, and sense and respond to extracellular pH changes as required. Bacterial intracellular pH control is tightly regulated against the constant exchange with its variable microenvironment. In general, bacteria adjust to the changes in encountered pH by changing the expression of appropriate genes for adaptation, virulence, and degradation or biosynthetic pathways (Olson, 1993). For example, *Salmonella enterica* expresses T3SS for assembly in acidic vacuoles at pH ~5 and dissociates T3SS in the cytosolic host pH of 7.2 (Yu et al., 2010). Likewise, *Pst* alters its environment by initiating the T3SS assembly and translocation only in the acidic plant apoplast (pH as low as 5) or the

acidic minimal medium *in vitro*, where a drop in solution pH is all that is required to initiate secretion at room temperature (Huynh et al., 1989; van Dijk et al., 1999). Optimum *Pst* intracellular pH requirements for survival and proliferation, more specifically during infection, are not known.

Bacterial intracellular pH values have been measured noninvasively by the use of pH-sensitive fluorophores that change their fluorescence emission maxima as a function of encountered pH. Fluorescent tags can be small molecules introduced into permeabilized cells, or transiently expressed proteins for a constant supply of fluorescent signal. Fluorescence studies reveal protein expression, complex formation, or localization. One well-studied fluorescent protein is the green fluorescent protein (GFP), first isolated from the fluorescent jellyfish *Aequorea victoria* (Southward and Surette, 2002). Other homologs or engineered mutants with altered properties have been widely used in the last two decades to make GFP one of the most common reporter proteins (Chudakov et al., 2005; Kanno et al., 2011; Tsien, 1998). There have been several GFP variants developed with pH sensing ability, generally termed pHluorins (Miesenböck et al., 1998). These GFP mutants are ratiometric either by emission (Miesenböck et al., 1998) or by excitation (Orij et al., 2009). We have used a recent EGFP construct named E^1GFP (Serresi et al., 2009) in our study. E^1GFP is a pHluorin ratiometric by emission, making it experimentally more tractable, and was originally shown to be optimally calibrated for the pH region of 5.5 to 8 (Serresi et al., 2009). The authors measured the cytoplasmic pH changes in the HeLa cells endocytic pathway by internalizing E^1GFP as a C-terminal fusion to the cell-penetrating HIV-Tat protein (Serresi et al., 2009). More recently, E^1GFP was used to visualize dendrimer endocytosis into HeLa cells during increasing vesicular

acidification as a way to determine the pathway of endocytosis of a specific type of dendrimer (Albertazzi et al., 2010). While E^{1}GFP unfolds at pH 5 and below (Serresi et al., 2009), it can report on pH changes in the slightly acidic region, making it an attractive choice for the measurement of *Pst* internal pH.

Here, we report the preliminary application of E^{1}GFP expressed in *Pst* cells by employing the same plasmid construct pCPP5811 with NPTII promoter that we previously used to study AvrPto translocation in *Pst* (Chapter 3). We performed E^{1}GFP calibration by using the purified protein in McIlvaine's buffer at pH 5.2–7.5 and measuring the fluorescence emission of each pH sample. For the *in vivo Pst* measurement, we injected concentrated *Pst* cells expressing E^{1}GFP into domestic tobacco *Nicotiana tabacum* leaves and measured individual *Pst* cell fluorescence emission from a total of 10 cells in the focal plane. Our data suggest an intracellular *Pst* pH of 5.4 ± 0.1; however, a directly applicable calibration curve of E^{1}GFP emission from *Pst* cells using identical experimental setup is needed before this result can be finalized.

Results

E^{1}GFP calibration curve may be utilized for slightly acidic to slightly basic pH measurements. E^{1}GFP was overexpressed and purified from *Escherichia coli* BL21 cells followed by N-terminal His_6 tag cleavage and protein concentration to 80 μM for fluorescence. McIlvaine's buffer was used as described previously (Chapter 2 and 3) and E^{1}GFP samples were prepared by buffer-exchange, equilibration for up to 2 h, and degassing in the quartz cuvette prior to fluorescence measurement. Emission scans scaled to the same curve area are shown in Figure 4.1A.

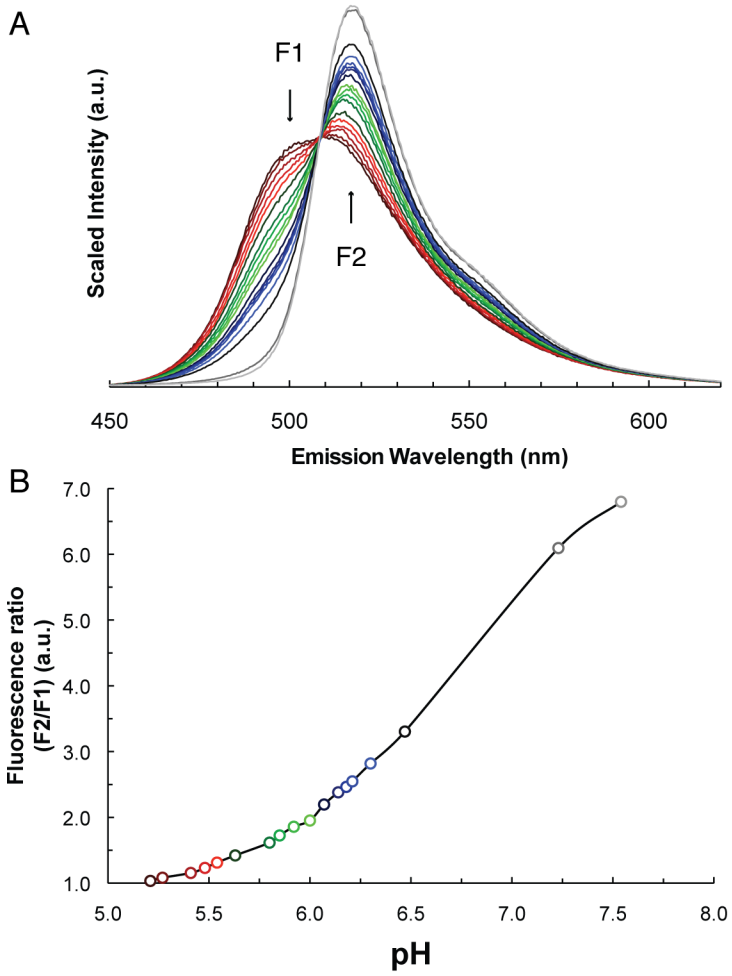

Figure 4.1. Fluorescence emission data for the E^{1}GFP calibration curve calculation. (A) Emission intensity is shown normalized to be of equal total area since the protein solution was kept at constant 80 μM concentration. Arrows indicate the positions of F1 (500 nm region) and F2 (520 nm region) peaks where the emission intensity decreases (F1) and increases (F2) with increasing pH, giving rise to the F2/F1 ratio as the pH measurement. Fluorescence was measured of the E^{1}GFP samples prepared at pH 5.21 (darkest red line), 5.27, 5.41, 5.48, 5.54 (lightest red line), 5.63 (darkest green line), 5.80, 5.85, 5.92, 6.00 (lightest green line), 6.07 (darkest blue line), 6.14, 6.18, 6.21, 6.30 (lightest blue line), 6.47 (black line), 7.23 (dark gray line), and 7.54 (light gray line). E^{1}GFP excitation at 403 nm, emission collected over 415–620 total range in 0.5 nm steps. (B) Calibration curve is obtained by calculating F2/F1 ratio of each E^{1}GFP sample emission shown in (A). Each value is shown color-coded to correspond with the sample data color in (A). Resulting F2/F1 values are joined by a smoothed line to highlight the ratio increase with pH.

Ratio of the emission peaks was chosen in order to optimize the fluorescence changes of the F1 and F2 peak region in the most acidic pH below 6. Empirically, F1 was chosen as 492.5–502.0 nm, and F2 as 512.0–521.5 nm. Each peak range was calculated as the sum of 20 consecutive data points in order to avoid any systematic errors in the measurement of each emission point. The resulting calibration curve is shown in Figure 4.1B. We focused on the F2/F1 change in the acidic range as the final *Pst* intracellular pH measurement is expected to depend on the sensitivity of E^{1}GFP ratiometric properties in that range. However, the most sensitive region with the largest F2/F1 changes occurs in the pH 6.0–7.3 range overall that may not be of benefit in the *Pst* system scenario.

E^{1}GFP emission in* E. coli *confirms the feasibility of E^{1}GFP use in our experiments. For an initial check that E^{1}GFP may be used for cellular measurements with our experimental setup, we checked E^{1}GFP emission in *E. coli* BL21 cells after overexpression of E^{1}GFP for 24 h at 15 °C. Fluorescence emission scan showed a clear E^{1}GFP peak distribution (Figure 4.2), with a resulting F2/F1 ratio of 4.3 that corresponds to a pH of 6.7 (using the Figure 4.1B calibration curve). This is only an approximation, as there was no negative control *E. coli* cells grown in the same way and this measurement was done as a simple check for the E^{1}GFP signal.

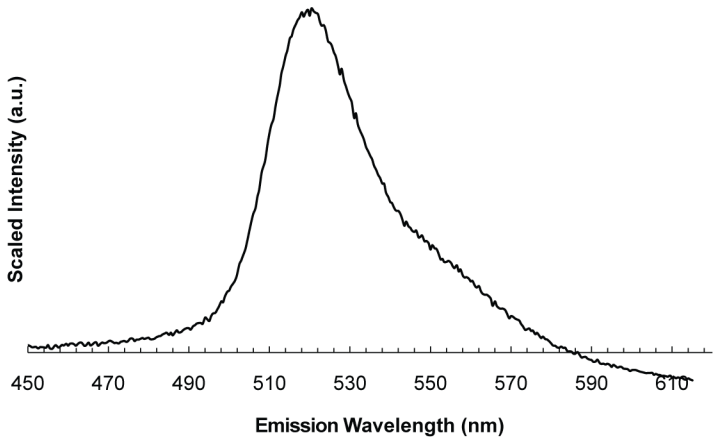

Figure 4.2. Example utility of E[1]GFP emission in *E. coli* cells carrying the protein. E[1]GFP emission spectrum of *E. coli* BL21 cells after overexpressing E[1]GFP for 24 h at 15 °C for subsequent protein purification. The curve is scaled in the same fashion as the data in Figure 4.1 in order to preserve the proportions for visual comparison.

Pst ***cells express E[1]GFP and the intracellular*** **Pst** ***pH in the plant apoplast may be measured***. GFP in general is known to be secretion-incompetent through the T3SS when expressed with an N-terminal signal sequence targeting it for export in a study on *Salmonela enterica* T3SS (Akeda and Galán, 2005). With no loss of signal due to GFP export out of the cell cytoplasm and any resulting extracellular background interference, this is an advantageous system for *Pst* intracellular signal measurement. E[1]GFP was expressed in *Pst* in the same manner as the AvrPto-Cya constructs previously (Chapter 3) and was shown to give rise to GFP fluorescence signal in preliminary images using Zeiss Axioskop 2 fluorescence microscope with the excitation filter at 436 ± 10 nm and emission at 480 ± 20 nm. Under these conditions, E[1]GFP expressing *Pst* cells could be visualized, while the *Pst* wt cells were not visible (data not shown).

E[1]GFP emission scan was measured in *Pst* cells for additional conformation that E[1]GFP is excitable with the expected excitation peak in our cellular system. An overlay of the raw scan data (Figure 4.3A) shows a small autofluorescence peak of WT *Pst* without E[1]GFP, but the resulting difference in signal from cells with E[1]GFP and without (both adjusted to OD_{600} of 0.5) shows a clear peak due to E[1]GFP excitation (Figure 4.3B).

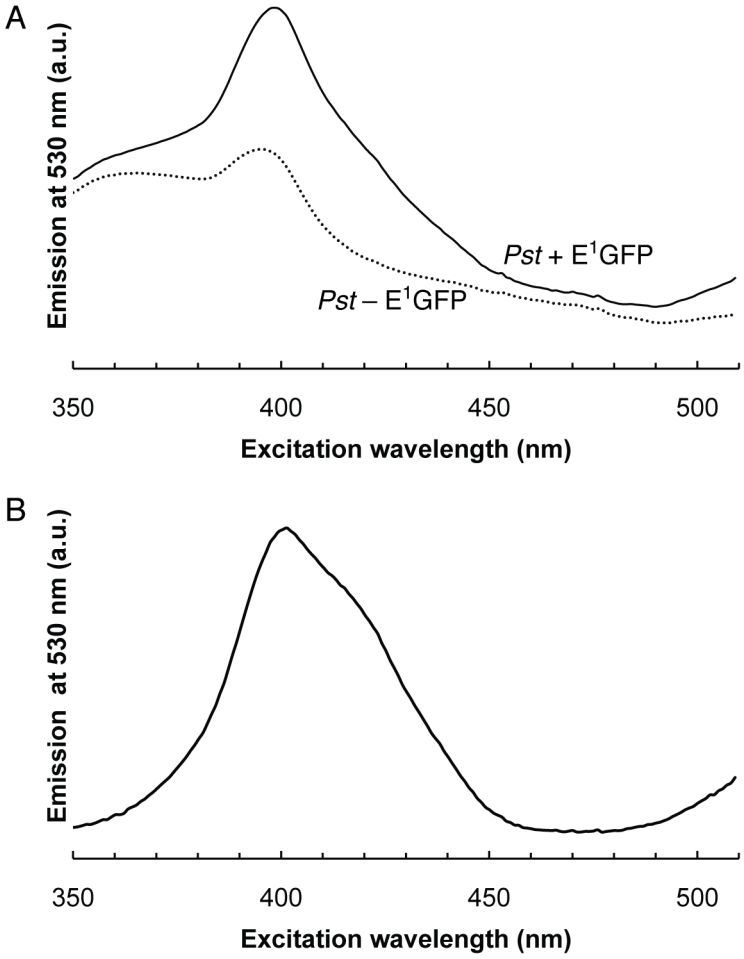

Figure 4.3. E^1GFP excitation peak check in *Pst* grown in KB rich medium at neutral pH. (A) Emission scans of *Pst* cells in solution expressing E^1GFP (OD_{600} 0.5, solid line) and *Pst* WT without E^1GFP (OD_{600} 0.5, dotted line) collected every 1 nm over the excitation wavelength range shown. (B) The difference between the two excitation scans in (A) results in an excitation peak that arises from the E^1GFP signal in *Pst* cells.

We were unable to obtain actual emission scan data from E^{1}GFP *Pst* solution visualized on a cover slide using a confocal Zeiss 710 microscope (excitation 405 nm, emission scan in one pass of 9.75 nm in the range of 473–551 nm). The mobility of cells on the cover slide glass surface resulted in high variability in signal and increasing the bacterial concentration increased the noise levels (data not shown). Further experimentation to immobilize the cells on the slide for intracellular pH measurements in the minimal secretion medium were not attempted at this time. Corresponding measurements in cuvettes using Cary Eclipse spectrophotometer yielded high noise levels and were intractable for emission scan measurements (data not shown).

Preliminary *Pst* intracellular pH measurement was obtained from high density cells (OD_{600} ~ 5) expressing E^{1}GFP injected into *N. tabacum* leaves in a consistent manner as the previous translocation experiments using the *Pst* and *N. tabacum* system (Chapter 3). Zeiss 710 confocal microscope emission scans were performed as described above on the inoculated plant leaf section prepared after at least 1 h of bacterial injection at RT of ~ 20–22 °C. Plants were of 4–5 weeks age and the 4th or 5th leaf was used, as for our previous plant experiments (Chapter 3). An example image of E^{1}GFP signal in *Pst* in plant apoplast is shown Figure 4.4. Emission scans were measured as described above and individual cells that were in focus were analyzed as defined regions over the scanned images. A total of 10 cellular signal peaks from 3 such scans of *Pst* in plant leaf samples were analyzed and the resulting intracellular signal was averaged. These experiments gave rise to the expected pH of 5.4 ± 0.1, which was consistent in the cells measured. Since the cellular focus regions are not expected to have any residual signal from surrounding plant tissue in the focal plane, no additional background correction was done

(confirmed by taking scans of background regions, resulting in no signal). Any unaccounted variability in signal and focus plane deviation is reflected in the standard deviation of the averaged result. For a final value, a larger sample size could be analyzed with a high total number of *Pst* cells scanned. That way, variations in signal possibly arising from (a) the stage of pathogenesis or (b) immediate leaf environment may be reflected in the pH measurements. Due to E^1GFP signal photobleaching after a single-pass scan no additional scans could be done in any one area repeatedly, while the initial collected data did not suffer from the effect.

Discussion

GFP is a versatile reporter protein on cellular trafficking, localization, and more recently, pH measurement of the reporter microenvironment. We have utilized the latter characteristic of a particular construct of a variant of EGFP with two additional mutations, for intracellular pH measurements in *Pst* while inside the plant leaf apoplast, the natural infection environment of this bacterium. We are interested in the pH conditions at that specific time since our data on a model effector AvrPto points to an acidic environment in the bacterial cytosol for efficient unfolded effector translocation for infection. Since AvrPto is not known to interact with a chaperone for 'priming' of AvrPto for T3SS, intracellular bacterial pH could be a determining factor in the ability of AvrPto to be delivered into the host cells.

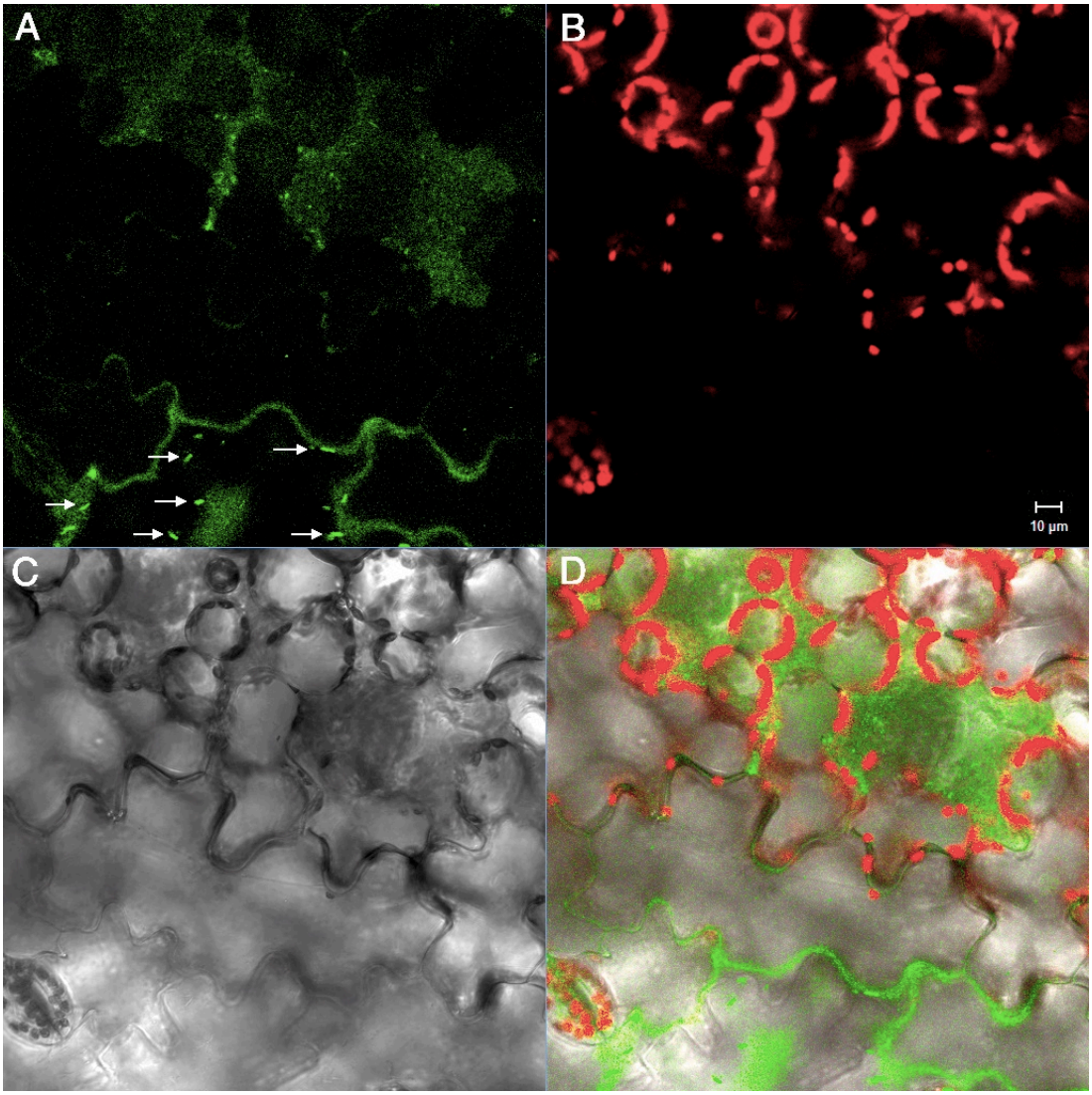

Figure 4.4. E[1]GFP visualization in *Pst* in the apoplast of *N. tabacum* using confocal microscopy. Excitation was set at 405 nm with a 488 nm laser for additional chloroplast visualization. (A) Green-color labeled signal emitted at 473–522 nm for E[1]GFP cells (indicated with white arrows) with low surrounding signal coming from plant cell surfaces (epidermal cell edges seen as green waves, dispersed background from the mesophyll), (B) red-color labeled emission at 598–690 nm for chlorophyll imaging, and (C) broad-field image of the plant tissue. (D) A combined image of (A), (B), and (C) indicating leaf surface epidermal cell edges as well as mesophyll. Embedded E[1]GFP *Pst* cells are shown as green rods typically smaller than 10 µm.

Our preliminary results indicate a possible intracellular *Pst* pH of 5.4 ± 0.1 while in the plant apoplast at the first 1–2 h upon injection. While most cells were seen to be mobile, our previous translocation data indicate initial AvrPto-Cya construct translocation and the resulting cAMP signal appearing within approximately 2 h after leaf inoculation with the highest levels at 22 °C (Figure 3.5). Intracellular pH measurements were performed at RT that was approximately in the same temperature range, and efficient infection can be assumed.

Finalized intracellular pH measurement requires significant optimization of the current preliminary experiment. First, a calibration curve of E^1GFP emission in *Pst* cells needs to be obtained. Cells need to be permealized by ionophores in order to arrest the intracellular pH at each solution value in order to construct a directly comparable calibration curve that can be applied to intact *Pst* cells. Second, a larger sample of in-focus *Pst* cells needs to be scanned and averaged for a true representation of intracellular conditions. It would be of value to separate cells that are freely mobile in plant apoplast versus attached cells with engaged T3SS, if the latter can be imaged without interference from the fluorescence signal originating from the cell walls upon excitation at 405 nm. Lastly, a different pH-sensitive GFP variant may be designed if the pH region of interest is close to the pH of unfolding of E^1GFP at around 5.

While we have focused on the *Pst* intracellular pH as the necessary and sufficient driving force for AvrPto export due to its structural sensitivity to pH, there may be alternative or additional factors impacting T3SS transport. An alternative explanation of the unfolded effector translocation process may be sufficient electrostatic forces in the T3SS channel itself to induce and drive

the unfolding of the channel substrates even at higher intracellular pH where AvrPto is predominantly in the folded form. For example, at pH 7.0-7.5 TrAvrPto is 97% folded (according to the global acid denaturation data fit from Figure 2.2B) while at pH 5.4 it is 73% folded. While a slightly acidic pH would benefit the unfolded form in the bacterium and the folded form in the host, other forces may be involved in AvrPto translocation. In the case of dominating channel electrostatics, the necessary proton motive force (PMF) and ATPase activity provide the energy required for the T3SS translocation function (Wilharm et al., 2007), and additionally for effector unfolding (Rathinavelan et al., 2010). In a recent modeling study on the translocation of the T3S needle protein MxiH traversing the *Shigella flexneri* T3SS, the authors concluded that the protein is exported as a helix-turn-helix structured motif in a screw-like motion through a predominantly electronegative channel interior (Rathinavelan et al., 2010). Since the MxiH surface in such a configuration is negative, there is a significant energy barrier for translocation, and PMF and/or the energy from the specific ATPase would be required. Given the predicted repulsion between protein and channel surfaces the ejection step upon delivery would be energetically favorable. This study hypothesizes that due to the electronegative patches on structured effector surfaces this may be a general mechanism of protein export.

While the electrostatic repulsion model may apply for some of the variety of exported proteins, it doesn't seem to be at work in the case of AvrPto. Since the evidence points to a fully unfolded polypeptide during translocation, the standard pI of 6.5 for WT AvrPto and pI of 6.4 of H87Y AvrPto, calculated from the primary sequence is an accurate measurement. Therefore, at any pH below 6.4, which is a likely case during translocation, the

effective surface of the traversing polypeptide would be positive and not repulsive in the electronegative channel interior. This minor difference in the electrostatics of the WT and H87Y constructs cannot explain the significant differences in the translocated protein levels discussed in Chapter 3. On the other hand, the needle protein MxiH (GI: 18462781) in the original study has a pI of 4.6 and would have to overcome the electronegative channel surface.

Studies on protein transport through nanometer-scale insulated pores typically observe variable results in the current drop due to the loss of channel conductivity during polypeptide passage (Talaga and Li, 2009). This has been attributed to the passage of unfolded proteins (shortest passage times) and the folded proteins that transiently block the channel while unfolding (longest passage times). Due to the linear nature of a translocated polypeptide, it is generally concluded that individual residue local charges are more important than the net charge on a protein. This conclusion would indicate that an electrostatic attraction or repulsion mechanism of effector export would need to be evaluated on the polypeptide sequence scale.

Delay in translocation of folded effectors would negatively impact the efficiency of effector delivery and prevention of initial host defenses. There is evidence of blockage of the secretion channel by impassable substrates in the *Yersinia* T3SS (Sorg et al., 2005). It is reasonable to predict that an available unfolded effector population would be advantageous for the T3S process and would indicate a moderately acidic bacterial cytoplasm in the case of AvrPto unfolding.

In the absence of a chaperone-AvrPto complex, the mechanism of AvrPto recognition and transport through the T3SS is most likely to depend solely on the expression levels, and sequence and structure of AvrPto in the

bacterial cell (Aldridge and Hughes, 2001). While the T3SS-associated ATPase has been shown to interact with chaperones and chaperone-effector complexes through the predicted cytoplasm-facing domain and facilitate effector release and unfolding(Akeda and Galán, 2005; Gauthier and Finlay, 2003), the fate of effectors that act without a chaperone is not known.

In conclusion, our initial results show that *Pst* cytoplasmic pH may be acidic at a low pH of 5.4 ± 0.1 which would optimize the export of effectors with similar structural stability to AvrPto. Effectors are translocated most effectively if their tertiary structures are biased for marginal stability and encode pH-sensing folding switches like the H87 in AvrPto to maintain a sufficient unfolded population 'primed' for secretion without the need for chaperone guidance, and subsequent predominantly folded conformation in the host cell.

Materials and Methods

E^{1}GFP plasmids. WT GFP plasmid in pET-28a(+) (Invitrogen) vector containing Kanamycin resistance cassette and an N-terminal His_6 tag followed by a Tobacco Etch Virus Nuclear Inclusion a (TEV) protease cleavage site of ENLYFQ|G (cut site indicated) was provided by The Protein Facility, Department of Chemistry and Chemical Biology, Cornell University. The following mutations were introduced: F65L, T66S, R81Q, T203Y, and H232L in order to construct an EGFP-based sequence with additional mutations for the final E^{1}GFP according to the originating study (Serresi et al., 2009).

Broad-host range plasmid pCPP5811 containing E[1]GFP sequence was constructed as described in Chapter 3 for the AvrPto sequence insertion by using a Gateway recombination reaction.

Final E[1]GFP sequence of 239 residues in the pET-28a(+) vector (mutation sites from WT GFP underlined):
MVSKGEELFT GVVPILVELD GDVNGHKFSV SGEGEGDATY GKLTLKFICT TGKLPVPWPT LVTTLSYGVQ CFSRYPDHMK QHDFFKSAMP EGYVQERTIF FKDDGNYKTR AEVKFEGDTL VNRIELKGID FKEDGNILGH KLEYNYNSHN VYIMADKQKN GIKVNFKIRH NIEDGSVQLA DHYQQNTPIG DGPVLLPDNH YLSYQSALSK DPNEKRDHMV LLEFVTAAGI TLGMDELYK.

Forward primers used in mutagenesis (mutation sites underlined): F65L: 5′- GTGACCACCCTGTCCTACGGCGTGCAG -3′ (Serresi et al., 2009), R81Q: 5′- CGACCACATGAAGCAGCACGACTTCTTCAAG -3′, T204Y: 5′- CAACCACTACCTGAGCTACCAGTCCGCCCTGAG -3′ (Serresi et al., 2009), H232L: 5′- GCCGGGATCACTCTGGGCATGGACG -3′.

E[1]GFP overexpression and purification. *E. coli* BL21(DE3) cells (Qiagen) containing E[1]GFP in pET-28a(+) vector were grown in Luria Broth (LB) medium with 50 μg/mL kanamycin sulfate in a 10-mL starter culture with 225 rpm shaking overnight, gently pelleted and added to a final 1-L medium with kanamycin and grown to an OD_{600} of 0.6. Culture was transferred to a 15 °C shaker and induced with 0.8 mM isopropyl β-D-1-thiogalactopyranoside (IPTG) for 24 h. Cell sample for initial E[1]GFP fluorescence measurement (Figure 4.2B) was obtained from the culture at that time.

Cells were pelleted and frozen at -20 °C overnight. Lysis was achieved by sonication and the resulting supernatant was obtained and the purified

protein was obtained after ultracentrifugation, loading, washing and elution from a Ni-NTA affinity chromatography column after incubation with the protease at 4 °C, as described previously (Chapter 2).

E[1]GFP calibration curve. Final protein solution was dialyzed into McIlvaine's buffer system at 230 mM ionic strength as used throughout our experiments (Chapters 2-3) at pH 7 and concentrated to 100 μM. Individual E[1]GFP samples for fluorescence experiments to obtain the calibration curve over the pH range of 5.2–7.5 were buffer-exchanged using 500 μL Zeba desalting columns (Thermo Scientific) into appropriate pH buffer.

Fluorescence emission scans were obtained for each pH sample by using a Cary Eclipse Fluorescence Spectrophotometer (Varian Instruments) with excitation set to 403 nm, scanning over 415.0–620.0 nm with 2.5 nm excitation slit width, 30 nm/min scan rate, 1 s averaging time and 0.5 nm data interval. PMT detector voltage was set at 900 V and temperature was controlled with the sample cuvette block at 22 °C.

***E[1]GFP fluorescence experiments in* N. tabacum**. *In planta* experiments followed the procedures outlined in Chapter 3. *Pst* containing E[1]GFP.pCPP5811 plasmid (transformed by electroporation) were grown for a day on KB plates with 10 μg/mL rifampicin (*Pst* resistance) and gentamicin (plasmid resistance), then suspended in 5 mM 2-(*N*-morpholino)ethane-sulfonic acid (MES) buffer at pH 6.5, and inoculated into plant leaves. Four to five weeks old *N. tabacum* plants were provided by Dr. Alan Collmer's lab.

Inoculated leaves were kept enclosed with moist paper towels while in transport to the confocal microscope. An approximately 1-cm^2 section was

excised with a razor blade and sandwiched with a drop of water between a cover slide and a glass slip.

Zeiss confocal 710 microscope was used to visualize the samples and measure the E^1GFP emission with the following settings: excitation at 405 nm, emission scan in one pass of 9.75 nm in the range of 473.0–551.0 nm. Individual *Pst* cell regions were defined by the observed fluorescence emission of rod-shaped bacterium regions and signal brightness was calculated using Zeiss software. Raw emission values were used from the image at F1 signal peak of 492.5–502.25 nm range (497.4 nm midpoint), and the image designated as F2 at 512.0–521.75 nm range (516.9 nm midpoint). Resulting F2/F1 ratios were calculated for a total of 10 well-defined bacteria images from a total of 3 fluorescence emission scans at different leaf areas, and the corresponding individual-cell pH values were averaged in Excel.

BIBLIOGRAPHY

Akeda, Y., and Galán, J.E. (2005). Chaperone release and unfolding of substrates in type III secretion. Nature *437*, 911-915.

Albertazzi, L., Serresi, M., Albanese, A., and Beltram, F. (2010). Dendrimer internalization and intracellular trafficking in living cells. Mol Pharm *7*, 680-688.

Aldridge, P., and Hughes, K.T. (2001). How and when are substrates selected for type III secretion? Trends Microbiol *9*, 209-214.

Chudakov, D.M., Lukyanov, S., and Lukyanov, K.A. (2005). Fluorescent proteins as a toolkit for in vivo imaging. Trends Biotechnol *23*, 605-613.

Dawson, J.E. (2008). Barriers to Translocation Stability, Kinetics, and Acid Denaturation of AvrPto. Thesis (PhD)--Cornell University, August, 2008.

Gauthier, A., and Finlay, B.B. (2003). Translocated intimin receptor and its chaperone interact with ATPase of the type III secretion apparatus of enteropathogenic Escherichia coli. Journal of Bacteriology *185*, 6747-6755.

Hoiczyk, E., and Blobel, G. (2001). Polymerization of a single protein of the pathogen Yersinia enterocolitica into needles punctures eukaryotic cells. Proceedings of the National Academy of Sciences of the United States of America *98*, 4669-4674.

Huynh, T.V., Dahlbeck, D., and Staskawicz, B.J. (1989). Bacterial blight of soybean: regulation of a pathogen gene determining host cultivar specificity. Science *245*, 1374-1377.

Kanno, A., Ozawa, T., and Umezawa, Y. (2011). Detection of Protein-Protein Interactions in Bacteria by GFP-Fragment Reconstitution. Methods Mol Biol *705*, 251-258.

Losada, L.C., and Hutcheson, S.W. (2005). Type III secretion chaperones of Pseudomonas syringae protect effectors from Lon-associated degradation. Molecular Microbiology *55*, 941-953.

Miesenböck, G., De Angelis, D.A., and Rothman, J.E. (1998). Visualizing secretion and synaptic transmission with pH-sensitive green fluorescent proteins. Nature *394*, 192-195.

Olson, E.R. (1993). Influence of pH on bacterial gene expression. Mol Microbiol *8*, 5-14.

Orij, R., Postmus, J., Ter Beek, A., Brul, S., and Smits, G.J. (2009). In vivo measurement of cytosolic and mitochondrial pH using a pH-sensitive GFP derivative in Saccharomyces cerevisiae reveals a relation between intracellular pH and growth. Microbiology (Reading, Engl) *155*, 268-278.

Rathinavelan, T., Zhang, L., Picking, W.L., Weis, D.D., De Guzman, R.N., and Im, W. (2010). A repulsive electrostatic mechanism for protein export through the type III secretion apparatus. Biophys J *98*, 452-461.

Serresi, M., Bizzarri, R., Cardarelli, F., and Beltram, F. (2009). Real-time measurement of endosomal acidification by a novel genetically encoded biosensor. Analytical and bioanalytical chemistry *393*, 1123-1133.

Sorg, J.A., Miller, N.C., Marketon, M.M., and Schneewind, O. (2005). Rejection of impassable substrates by Yersinia type III secretion machines. J Bacteriol *187*, 7090-7102.

Southward, C.M., and Surette, M.G. (2002). The dynamic microbe: green fluorescent protein brings bacteria to light. Mol Microbiol *45*, 1191-1196.

Stebbins, C.E., and Galán, J.E. (2001). Maintenance of an unfolded polypeptide by a cognate chaperone in bacterial type III secretion. Nature *414*, 77-81.

Talaga, D.S., and Li, J. (2009). Single-molecule protein unfolding in solid state nanopores. J Am Chem Soc *131*, 9287-9297.

Tsien, R.Y. (1998). The green fluorescent protein. Annu Rev Biochem *67*, 509-544.

van Dijk, K., Fouts, D.E., Rehm, A.H., Hill, A.R., Collmer, A., and Alfano, J.R. (1999). The Avr (effector) proteins HrmA (HopPsyA) and AvrPto are secreted in culture from Pseudomonas syringae pathovars via the Hrp (type III) protein secretion system in a temperature- and pH-sensitive manner. J Bacteriol *181*, 4790-4797.

Wilharm, G., Dittmann, S., Schmid, A., and Heesemann, J. (2007). On the role of specific chaperones, the specific ATPase, and the proton motive force in type III secretion. Int J Med Microbiol *297*, 27-36.

Yu, X.-J., Mcgourty, K., Liu, M., Unsworth, K.E., and Holden, D.W. (2010). pH Sensing by Intracellular Salmonella Induces Effector Translocation. Science (New York, NY).

CHAPTER 5

BINDING AND INHIBITION OF HUMAN SPERMIDINE SYNTHASE BY DECARBOXYLATED *S*-ADENOSYLHOMOCYSTEINE[*]

Introduction

Polyamines are essential for normal cell growth and development and the polyamine biosynthetic pathway is an important target for the development of therapeutics including cancer chemopreventive agents, cancer therapeutics and agents for treatment of diseases caused by parasitic protozoa such as sleeping sickness, Chagas disease, leishmaniasis and malaria (Barker et al., 2009; Boitz et al., 2009; Casero and Marton, 2007; Gerner and Meyskens, 2004; Heby et al., 2007; Marton and Pegg, 1995; van Brummelen et al., 2008). Spermidine is a major polyamine that serves multiple functions in growth including its role as a precursor of hypusine, which is essential for the activity of the eukaryotic initiation factor elF-5A (Blavid et al., 2009; Chattopadhyay et al., 2008; Park et al., 1997; Park et al., 2010).

Polyamines are formed in eukaryotes and in many, but not all, prokaryotes by the action of aminopropyltransferases. These form a class of enzymes that use decarboxylated *S*-adenosylmethionine (dcAdoMet)[2] as a substrate and transfer the aminopropyl group to an amine acceptor molecule generating 5'-deoxy-5'-methylthioadenosine (MTA) as a byproduct. Some aminopropyltransferases such as human spermidine synthase (SpdS) (which acts upon putrescine) and spermine synthase (SpmS) (acting on spermidine)

[*] Seckute, J.; McCloskey, D. E.; Thomas, H. J.; Secrist, J. A.; Pegg, A. E.; Ealick, S. E. Binding and inhibition of human spermidine synthase by decarboxylated *S*-adenosylhomocysteine. *Manuscript in submission*

are highly specific for their amine acceptors (Ikeguchi et al., 2006; Wu et al., 2007b; Wu et al., 2008), while others such as those from acute thermophiles, which contain a variety of polyamines not found in mammals, are less discriminating (Cacciapuoti et al., 2007; Ikeguchi et al., 2006; Korolev et al., 2002; Ohnuma et al., 2005; Wu et al., 2007b). There are now numerous published structures for aminopropyltransferases including those for SpdS from *Thermotoga maritima* (TmSpdS) (Korolev et al., 2002), *Caenorhabditis elegans* (Dufe et al., 2005), *Plasmodium falciparum* (Dufe et al., 2007), *Helicobacter pylori* (Lu et al., 2007), human hSpdS (Wu et al., 2007b), *Arabidopsis thaliana* (PDB code 2Q41) and *Trypanosoma cruzi* (PDB code 3BWC), aminopropylagmatine/aminopropylagmatine synthases from *Thermus thermophilus* (PDB code 1UIR), *Pyrococcus horikoshii* (PDB code 2ZSU) and *Pyrococcus furiosus* (Cacciapuoti et al., 2007) and SpmS from humans (hSpmS) (Wu et al., 2008).

A general mechanism for aminopropyl transfer has been proposed based on kinetic studies of hSpdS, TmSpdS and hSpmS, their structures bound to substrates and inhibitors, and the results of site-directed mutagenesis of key residues (Korolev et al., 2002; Wu et al., 2007b). This mechanism depends on a conserved Asp (residue 173 in hSpdS) in the active site that interacts with the bound amine substrate to deprotonate the attacking nitrogen of the amine. This interaction is reinforced by additional interactions of this nitrogen with the hydroxyl of a conserved Tyr (residue 79 in hSpdS) and a backbone carbonyl group (Ser174 in hSpdS). These interactions allow the attack on the methylene carbon of the aminopropyl group attached to the sulfonium center of dcAdoMet. Electron transfer to this S atom completes the reaction forming MTA and the polyamine product (Figure 5.1). The positively charged

sulfonium is a critical part of this reaction. The dcAdoMet binding site at the active site of the aminopropyltransferases whose structure is known shows a negatively charged binding pocket with highly conserved residues that interact with the purine base, the 6-NH2- substituent and the ribose hydroxyls of the nucleoside substrate as well as the aminopropyl NH_2 of the sidechain but there are no direct interactions with the S^+. These findings raise the possibility that an analog of dcAdoMet lacking this charge would bind specifically in the active site but would be unable to take part in the displacement reaction.

We have tested this possibility by synthesizing dcSAH and investigating its ability to inhibit hSpdS and hSpmS and determination of the crystal structure of its complex with hSpdS. X-ray diffraction data of the complex shows the binding site occupied with dcSAH in a similar conformation as the previously determined substrate and product complex structures. We did not observe the binding of putrescine upon cocrystallization of hSpdS in the presence of dcSAH and putrescine, suggesting that binding would not be affected by the cellular polyamine concentration. The results suggest that dcSAH is a potentially useful first generation inhibitor that may be used to develop more potent and specific inhibitors of aminopropyltransferases.

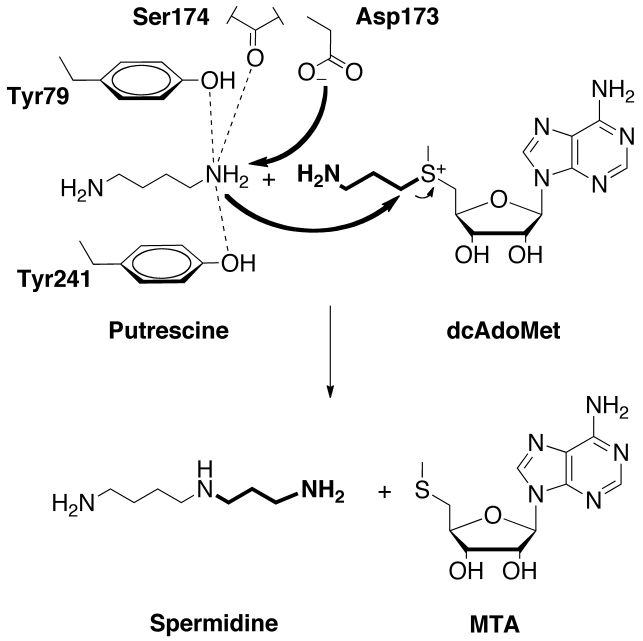

Figure 5.1. Reaction scheme of hSpdS aminopropyl transfer. General putrescine active site amine group interactions are shown. Curved arrows depict the proposed electron transfer steps. The aminopropyl group that is transferred from the dcAdoMet molecule to putrescine to form spermidine is shown in bold. Primary and secondary amine groups are shown in their neutral states for the scheme

Results

Inhibition of aminopropyltransferase activity by dcSAH. As shown in Figure 5.2, dcSAH was a potent dose dependent inhibitor of both hSpdS and hSpmS. The IC_{50} values of 43 μM and 5 μM respectively. In preliminary studies we also tested the dcSAH as an inhibitor of two other aminopropyltransferases the TmSpdS and the PfSpdS. Both of these enzymes were significantly more sensitive than hSpdS with IC_{50} values of 2 μM and 5 μM, respectively.

Crystal Structure of hSpdS/dcSAH complex. The hSpdS structure in complex with dcSAH was determined (Figure 5.3A), and the bound inhibitor was found to be present in both chains of hSpdS (Figure 5.3B). hSpdS is a dimer consisting of an N-terminal β-sheet domain (residues 1–72), a central core domain (residues 73–267), and a C-terminal domain (residues 268–302), as described previously (Wu et al., 2007a). The first 14 residues were disordered in the crystal structure, consistent with previous results.

The dcSAH binding is facilitated by hydrogen bonding with highly conserved active site residues (Figure 5.3B,C) (Wu et al., 2007a). The positively charged amine group of the aminopropyl moiety is positioned in the negatively charged polar binding pocket of D104 (absolutely conserved), D173 (absolutely conserved), and Q80. The ribose ring hydrogen bonds with E124 and an absolutely conserved Q49. The inhibitor is bound in the *S* form, with the N1 of the adenosine moiety interacting with the backbone of G156, N7 weakly hydrogen bonding with the backbone of A181, and N6 coordinated by D155 and the backbone of P180.

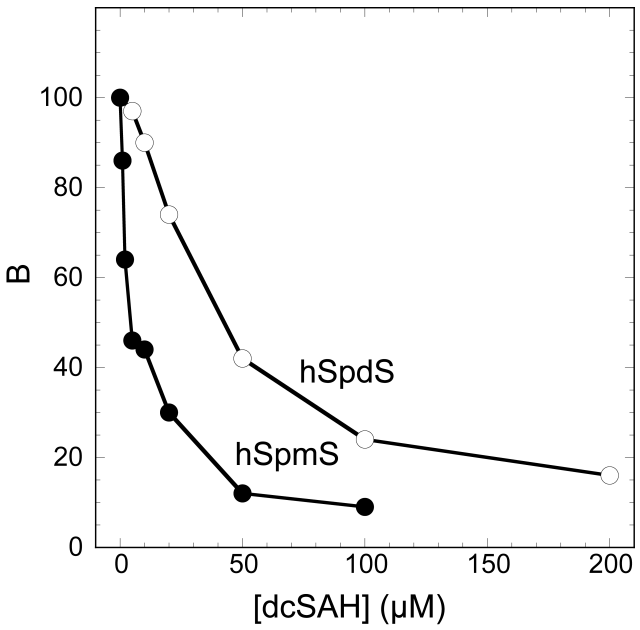

Figure 5.2. Inhibition of hSpdS and hSpmS by dcSAH.

Figure 5.3. Structure of hSpdS in complex with the dcSAH inhibitor. (A) Ribbon diagram of the side and top views of the dimer of hSpdS with dcSAH shown bound in both active sites. N-terminal beta-stranded domain in shown in blue, the core domain in green, and the C-terminal α-helical domain in red. Ligand carbon atoms are colored in dark grey, nitrogen atoms are colored blue, oxygen atoms are colored red, and sulfur atoms are colored yellow. (B) Stereoview of dcSAH showing the $2F_o–F_c$ density around the ligand at the contour level of 1.0 σ. Water molecule that hydrogen bonds with Asp 104 and the ribose 3´-hydroxyl group of ribose is shown as a red sphere. Ligand carbon atoms are shown as light grey, enzyme carbon atoms are shown in green. The rest of the atoms are colored as described above. Hydrogen bonding partners are connected with black dashed lines, with bond distances denoted in Å. (C) Schematic drawing of the active site residues in the ligand binding pocket. Based on the basic crystallization conditions, Asp side chains are shown negatively charged. Hydrogen bond partners are connected with dashed lines, with bond distances in Å.

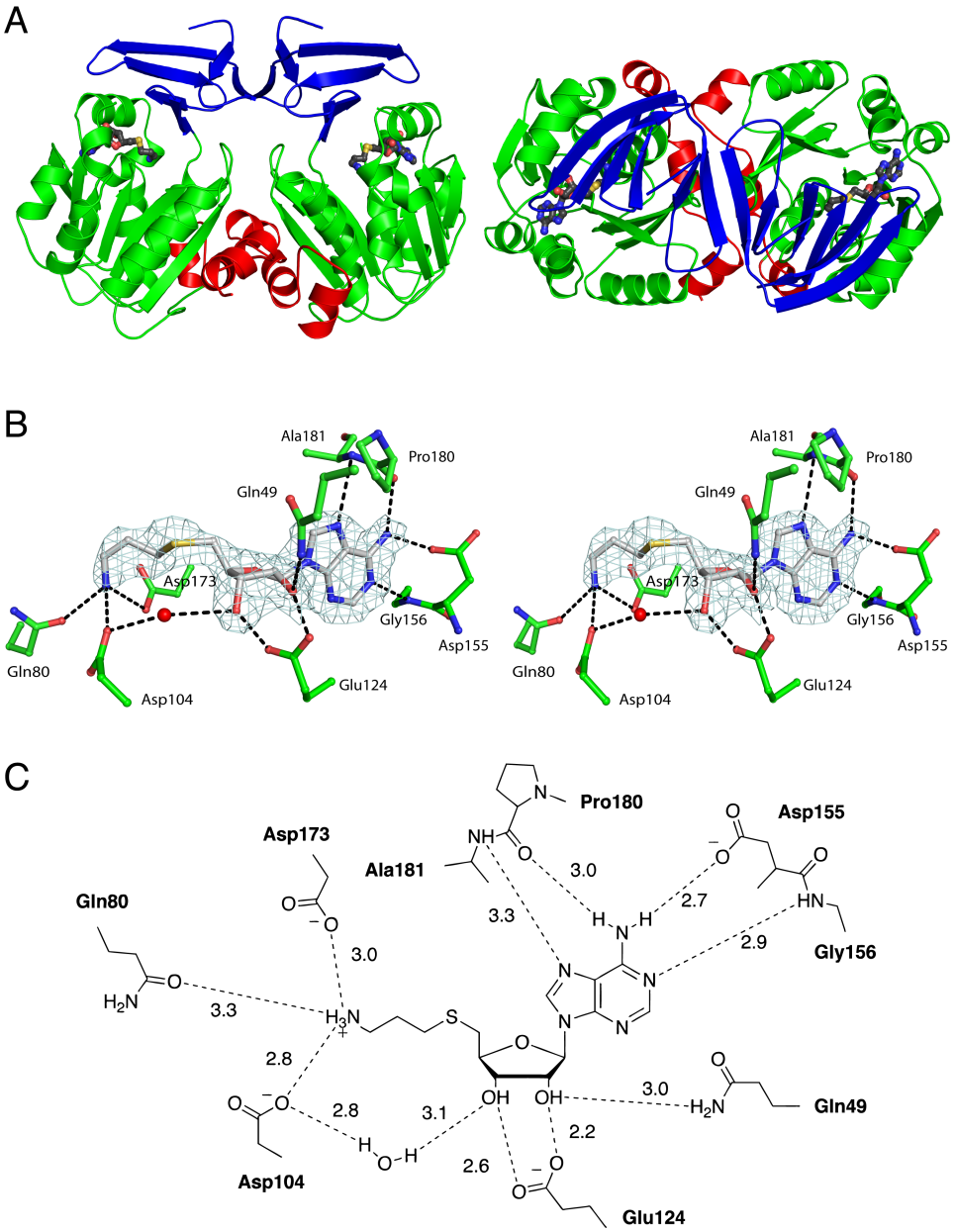
A
B
Ala181
Pro180
Gln49
Asp173
Gly156
Asp155
Gln80
Asp104
Glu124
C
Pro180
Asp155
Asp173
Ala181
Gln80
Gly156
Gln49
Asp104
Glu124

Comparison of the active site positions with previous structures. Position of the adenosyl moiety in hSpdS/dcSAH closely matches the hSpdS/MTA structure, determined previously (PDB ID 2O07). The largest deviation of 2.4 Å was between the sulfur atoms. The amine group of dcSAH is positioned within 0.7 Å of N1 in spermidine in the product complex structure, in excellent agreement with the expected amine coordination (Figure 5.4). The rest of the spermidine/putrescine binding site cavity is occupied by water molecules, which were consistent between the two chains of the hSpdS/dcSAH dimer.

The gatekeeping loop (residues 174–182) that envelops the active site is known to become ordered only upon ligand binding (Wu et al., 2007a). In the hSpdS/dcSAH complex structure the gatekeeping loop is only partially ordered, with residues 175–178 absent in chain A and residues 176–178 absent in chain B. Weak partial density was observed, but the loop structure could not be fully determined.

Putrescine Binding Site is Occupied by Water Molecules. No putrescine binding was observed in hSpdS/dcSAH complex structure (Figure 5.4). Superposition with the known hSpdS/MTA/putrescine complex (PDB ID 2O06) shows a water molecule occupying the N2 binding pocket of putrescine (difference of 0.8 Å). A second water molecule is hydrogen bonded to the side chains of Gln70 and Gln206, which are found pointing towards the putrescine binding cavity with an average of 1.0 Å deviation compared to the putrescine complex structure (PDB code 2O06, Figure 5.4).

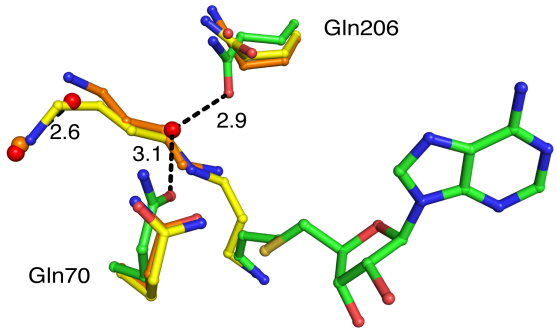

Figure 5.4. Putrescine binding site is occupied by water molecules in the hSpdS/dcSAH complex. Superposition with known hSpdS/putrescine/MTA and hSpdS/spermidine/MTA structures is shown. Putrescine molecule (PDB ID 2O06) carbon atoms with corresponding protein side chain carbon atoms and a structural water molecule in the active site are drawn in orange. Spermidine molecule (PDB ID 2O07) carbon atoms are shown in yellow. This superposition was made against the hSpdS/dcSAH complex with carbon atoms drawn in green and active site water molecules in red. Hydrogen bonding network of the structural water molecules in the putrescine binding site is shown as dashed lines, with designated bond distances in Å.

Discussion

Typically, SpdS is known to be a homodimer, and our findings agree with the expected oligomerization state (Ikeguchi et al., 2006). He, we report a complex structure of hSpdS with a novel inhibitor dcSAH that is bound to both monomers of hSpdS in the crystal lattice. Electron density in the putrescine binging site suggested only the presence of water molecules at the charged amine coordination sites, even at the conditions of 5 mM putrescine in the crystallization buffer. Binding of dcSAH in the active site is consistent with previously determined substrate, product, or inhibitor SpdS structures underlying a conserved mechanism of binding and catalysis. The gate keeping loop on one side of the active site that is typically ordered around an occupied active site and disordered in apo structures is found mostly disordered in our determined structure with weak partial density in the connecting region. Given the conserved position of dcSAH in the dcAdoMet binding site, the reason for the observed disorder in the gate-keeping loop is unclear.

Inhibitor binding was tested for SpdS from several species. IC_{50} values ranged from 2 μM in TmSpdS, 5 μM in PfSpdS, to 43 μM in hSpdS. The dcSAH is also effective in hSpmS inhibition with an IC_{50} of 5 μM. This distribution of activity places hSpdS as the weakest binding partner for dcSAH of the constructs tested. Additionally, due to close structural similarity to dcAdoMet, it is not surprising that we observed significant inhibition of hSpmS as well.

The necessity of polyamines in cellular development and viability make SpdS inhibition an important study for therapeutic purposes. The only source of higher polyamines like spermidine or spermine in eukaryotes requires the function of SpdS; therefore, there have been several inhibitors developed for

this enzyme. The strongest inhibitor to date is a transition-state mimic adenosylspermidine [3-(*R,S*)-(5′-deoxy-5′-carbaadenos-6′yl)-spermidine], with an IC_{50} of ~14 nM (Lakanen et al., 1995). While adenosylspermidine, like several other inhibitors, is not exclusive to SpdS and also inhibits SpmS, these families of structures exemplify the model of action of aminopropyltransferases, as well as direct the drug design efforts.

Our determined structure of hSpdS with a novel inhibitor dcSAH adds a new class of possible inhibitors for SpdS by using a reactant mimic. The simple yet effective change to design an inactive dcAdoMet-like small molecule for SpdS binding requires a single change at the reactive sulfonium center by the removal of the positive charge in the absence of sulfur-coordinated methyl. The structure presented here determines the dcSAH position in the active site and enables further efforts of inhibitor improvement while using hSpdS/dcSAH complex structure as the starting point in inhibitor design and optimization.

Materials and Methods

Synthesis of dcSAH. To approximately 250 mL of liquid ammonia in a dry ice bath was added 1.12 g (5.14 mmol) of 3-benzylthio-1-aminopropane hydrochloride (Jamieson, 1963). This solution was stirred while metallic sodium was added until the blue color persisted for about 10 min. After the color dispelled, 5'-*O*-*p*-toluenesulfonyladenosine (2.43 g, 5.75 mmol) was added slowly and the solution was stirred for about 10 min. Then the solution was kept sufficiently cool to allow the ammonia to slowly evaporate over a period of hours. The residue was taken up in water, brought to approximately

pH 2, and then washed with $CHCl_3$. The aqueous layer was applied to a column of Dowex 50W-X4 (NH_4^+ form, 50-100 mesh), and eluted with a gradient of aqueous NH_4OH beginning at 1 N and ending with 10 N. Product fractions were combined, evaporated to dryness, taken up in 1 N H_2SO_4, and filtered. Dilution with two volumes of ethanol resulted in the formation of the desired product as a white solid, which was filtered off and dried, yielding 2.09 g (90%) of dcSAH, m.p. 178-180 °C (dec), lit m.p. 180-183 °C. Microanalytical data confirmed a composition of dcSAH·H_2SO_4·0.9 H_2O.

Overexpression and Purification of hSpdS. hSpdS was overexpressed in *Escherichia coli* BL21(DE3) containing the pET-28a(+) (Novagen), which encodes an N-terminal His_6 tag followed by a TEV protease cleavage site. Cells were grown in LB medium with 100 mg/mL Kanamycin with agitation and induced at OD_{600} = 0.6 with 1 mM isopropyl-1-tio-β-D-thiogalactoside (IPTG) at 15 °C. Cells were harvested after 20 – 24 hours with centrifugation at 8000×*g* for 15 min, frozen overnight at -80 °C and resuspended in the lysis buffer (50 mM Tris-HCl pH 8.0, 100 mM sodium chloride, 5% v/v glycerol, 0.1 mM phenylmethylsulphonyl fluoride, and 2.5 mM putrescine). Cells were lysed using a French pressure cell, the lysate was cleared by centrifugation, and the cell supernatant was purified using a Ni-NTA affinity chromatography column (Qiagen) in the buffer above with 10 mM imidazole, eluting the desired protein with 250 mM immidazole. The His_6 tag was cleaved overnight via dialysis in the presence of TEV protease against the buffer of 20 mM Tris-HCl pH 8.0, 100 mM sodium chloride, 5 mM calcium chloride, 2.5 mM magnesium chloride, 5 mM β-mercaptoethanol, 1% v/v glycerol. Cleaved protein sample was eluted through a Ni-NTA affinity column and further purified using a Superdex 75 size-exclusion column (GE Healthcare)

equilibrated in 20 mM Tris-HCl pH 8.0, 50 mM sodium chloride. Final protein sample was desalted using a HiPrep 26/10 desalting column (GE Healthcare) into the final buffer of 20 mM Tris-Hcl pH 8.0 and concentrated to 14 mg/mL in a 10 kDa cutoff microcon concentrator (Amicon). The protein was judged to be greater than 95% pure by SDS-PAGE gel analysis (data not shown). The yield of the purified protein was 10 mg/L.

Crystallization Conditions. Crystallization was carried out using the hanging drop vapor diffusion method at 22 °C, each drop containing 1.5 μL reservoir solution and 1.5 μL protein solution. Initial conditions were obtained from the sparse matrix screens (Hampton Research, Emerald Biostructures). Optimized crystals grew in 100 mM Tris-HCl pH 8.4, 200 mM sodium sulfate, and 20% w/v polyethylene glycol 3350. To obtain the ligand-complexed structure, 5 mM putrescine and 5 mM dcSAH were added to the protein solution and left to equilibrate for up to 6 h on ice prior to crystallization. Resulting plate-like crystals were cryoprotected with 10% v/v glycerol and flash frozen in liquid nitrogen for X-ray intensity measurements.

Data Collection and Processing. The X-ray diffraction data were collected at the NE-CAT 24-ID-C beamline at the Advanced Photon Souce (APS). Data were collected over 1 – 360° range with a 1 s exposure time and a 0.5° oscillation range using an ADSC Quantum 315 detector at 0.97918 Å and crystal to detector distance of 250 mm. The data were indexed, integrated and scaled using the HKL2000 program suite (Otwinowski and Minor, 1997). The data collection statistics are summarized in Table 5.1.

Table 5.1. Data collection statistics for hSpdS complex with dcSAH**.** Values in parenthesis are for the highest resolution shell.
$R_{sym}=\Sigma\Sigma_i | I_i - \langle I \rangle | / \Sigma \langle I \rangle$, where $\langle I \rangle$ is the mean intensity of the N reflections with intensities I_i and common indices *h,k,l*.

	hSpdS/dcSAH
Wavelength (Å)	0.97918
Space group	P 1 2_1 1
a (Å)	58.18
b (Å)	60.82
c (Å)	87.02
β (°)	108.05
Resolution (Å)	40.56–2.00
Total reflections	89877
Unique reflections	34600 (2376)
Redundancy	2.6 (1.4)
% completeness	89.3 (61.8)
I/σ	9.12 (2.79)
R_{sym}	11.9 (23.4)
Matthews coefficient ($Å^3$/Da)	2.15
Solvent content (%)	42.4

Structure Determination and Refinement. hSpdS/dcSAH structure was determined and refined using the published structure of hSpdS (PDB ID 2O07) at the same space group as the starting model, upon removal of the water molecules and the bound product complex. The model building was carried out using the program COOT 0.6 (Emsley and Cowtan, 2004). Refinement process involved rounds of simulated annealing, energy minimization, B-factor refinement, calculation of difference Fourier maps and manual model optimization using the program PHENIX release 1.5-2 (Adams et al., 2002). Difference F_o-F_c Fourier map was used to identify the ligands. dcSAH was successfully positioned in both chains present in the asymmetric unit; however, no density was seen for the putrescine molecule, and the putrescine binding site was occupied by water molecules. The final refinement statistics are given in Table 5.2.

Table 5.2. Refinement statistics for the hSpdS/dcSAH complex.

[a] R-factor = $\Sigma_{hkl} | |F_{obs}| - k|F_{cal}| | / \Sigma_{hkl} |F_{obs}|$, where F_{obs} and F_{cal} are observed and calculated structure factors, respectively.

[b] R-free is the sum is extended over a subset of reflections (5%) that were excluded from all stages of refinement.

[c] Glu 208 residue in both chains of the dimer is in the disallowed region of the Ramachandran plot.

	hSpdS/dcSAH
Resolution (Å)	40.56 – 2.00
R-factor[a]	0.211
R-free[b]	0.259
Number of non-H atoms	
Protein	4407
Ligand	46
Water	407
B-factors	
Protein (Å^2)	18.1
Ligand (Å^2)	24.5
Water (Å^2)	28.3
R.m.s deviations	
Bond lengths (Å)	0.007
Bond angles (Å)	1.1
Dihedrals	17.0
Ramachandran plot	
Most favored region (%)	90.1
Additional favored region (%)	9.5
Generously allowed region (%)	0
Disallowed region (%)[c]	0.4

Purification of hSpmS and TmSpdS. Recombinant hSpmS and TmSpdS were produced and purified as previously described (Korolev et al., 2002; Wu et al., 2008).

Assay of aminopropyltransferase activity. Activity was measured by following the production of [^{35}S]MTA from [^{35}S]dcAdoMet in 100 mM sodium phosphate buffer (pH 7.5), in the presence of spermidine or spermine as the amine acceptor (Wiest and Pegg, 1998). Reactions were run in triplicate for 30 min with an amount of enzyme that gave a linear rate of MTA production at 37 °C and concentrations of inhibitor that gave from 10 to 90% inhibition. The IC_{50} values were derived from plots of the residual activity against inhibitor concentration.

Achowledgements

Synthesis of dcSAH was performed in the laboratory of Dr. John A. Secrist at the Southern Research Institute at Birmingham, AL. X-ray diffraction data was collected at the Advanced Photon Source facility of the Argonne National Laboratory in Chicago, IL. Binding studies of dcSAH to hSpdS, hSpmS, and TmSpdS were carried out in the laboratories of Dr. Anthony E. Pegg and Dr. Diane E McCloskey at the Departments of Cellular and Molecular Physiology and Pharmacology at Milton S. Hershey Medical Center at the Pennsylvania State University in Hershey, PA. Manuscript was prepared as a joint effort of all involved coauthors. This work was supported, in whole or in part, by the National Cancer Institute, Bethesda, MD grant PO1 CA-94000.

BIBLIOGRAPHY

Adams, P.D., Grosse-Kunstleve, R.W., Hung, L.W., Ioerger, T.R., McCoy, A.J., Moriarty, N.W., Read, R.J., Sacchettini, J.C., Sauter, N.K., and Terwilliger, T.C. (2002). PHENIX: building new software for automated crystallographic structure determination. Acta Crystallographica Section D-Biological Crystallography *58*, 1948-1954.

Barker, R.H., Jr., Liu, H., Hirth, B., Celatka, C.A., Fitzpatrick, R., Xiang, Y., Willert, E.K., Phillips, M.A., Kaiser, M., Bacchi, C.J., *et al.* (2009). Novel S-adenosylmethionine decarboxylase inhibitors for the treatment of human African trypanosomiasis. Antimicrob Agents Chemother *53*, 2052-2058.

Blavid, R., Kusch, P., Hauber, J., Eschweiler, U., Sarite, S.R., Specht, S., Deininger, S., Hoerauf, A., and Kaiser, A. (2009). Down-regulation of hypusine biosynthesis in plasmodium by inhibition of S-adenosyl-methionine-decarboxylase. Amino Acids.

Boitz, J.M., Yates, P.A., Kline, C., Gaur, U., Wilson, M.E., Ullman, B., and Roberts, S.C. (2009). *Leishmania donovani* ornithine decarboxylase is indispensable for parasite survival in the mammalian host. Infect Immun *77*, 756-763.

Cacciapuoti, G., Porcelli, M., Moretti, M.A., Sorrentino, F., Concilio, L., Zappia, V., Liu, Z.J., Tempel, W., Schubot, F., Rose, J.P., *et al.* (2007). The first agmatine/cadaverine aminopropyl transferase: biochemical and structural characterization of an enzyme involved in polyamine biosynthesis in the hyperthermophilic archaeon Pyrococcus furiosus. J Bacteriol *189*, 6057-6067.

Casero, R.A., Jr., and Marton, L.J. (2007). Targeting polyamine metabolism and function in cancer and other hyperproliferative diseases. Nat Rev Drug Discov *6*, 373-390.

Chattopadhyay, M.K., Park, M.H., and Tabor, H. (2008). Hypusine modification for growth is the major function of spermidine in *Saccharomyces cerevisiae* polyamine auxotrophs grown in limiting spermidine. Proc Natl Acad Sci U S A *105*, 6554-6559.

Dufe, V.T., Luersen, K., Eschbach, M.L., Haider, N., Karlberg, T., Walter, R.D., and Al-Karadaghi, S. (2005). Cloning, expression, characterisation and three-dimensional structure determination of *Caenorhabditis elegans* spermidine synthase. FEBS Lett *579*, 6037-6043.

Dufe, V.T., Qiu, W., Muller, I.B., Hui, R., Walter, R.D., and Al-Karadaghi, S. (2007). Crystal structure of *Plasmodium falciparum* spermidine synthase in complex with the substrate decarboxylated S-adenosylmethionine and the potent Inhibitors 4MCHA and AdoDATO. J Mol Biol *373*, 167-177.

Emsley, P., and Cowtan, K. (2004). Coot: model-building tools for molecular graphics. Acta Crystallographica Section D-Biological Crystallography *60*, 2126-2132.

Gerner, E.W., and Meyskens, F.L. (2004). Polyamines and cancer: Old molecules, new understanding. Nature Reviews Cancer *4*, 781-792.

Heby, O., Persson, L., and Rentala, M. (2007). Targeting the polyamine biosynthetic enzymes: a promising approach to therapy of African sleeping sickness, Chagas' disease, and leishmaniasis. Amino Acids *33*, 359-366.

Ikeguchi, Y., Bewley, M., and Pegg, A.E. (2006). Aminopropyltransferases: function, structure and genetics. J Biochem *139*, 1-9.

Jamieson, G.A. (1963). The synthesis of 5'-deoxy-5'-S-(3-methylthiopropylamine)sulfoniumadenosine ("decarboxylated S-adenosylmethionine"). Journal of Organic Chemistry *28*, 2397-2400.

Korolev, S., Ikeguchi, Y., Skarina, T., Beasley, S., Arrowsmith, C., Edwards, A., Joachimiak, A., Pegg, A.E., and Savchenko, A. (2002). The crystal structure of spermidine synthase with a multisubstrate adduct inhibitor. Nature Struct Biol *9*, 27-31.

Lakanen, J.R., Pegg, A.E., and Coward, J.K. (1995). Synthesis and biochemical evaluation of adenosylspermidine, a nucleoside-polyamine adduct inhibitor of spermidine synthase. J Med Chem *38*, 2714-2727.

Lu, P.K., Tsai, J.Y., Chien, H.Y., Huang, H., Chu, C.H., and Sun, Y.J. (2007). Crystal structure of *Helicobacter pylori* spermidine synthase: a Rossmann-like fold with a distinct active site. Proteins *67*, 743-754.

Marton, L.J., and Pegg, A.E. (1995). Polyamines as targets for therapeutic intervention. Annu Rev Pharm *35*, 55-91.

Ohnuma, M., Terui, Y., Tamakoshi, M., Mitome, H., Niitsu, M., Samejima, K., Kawashima, E., and Oshima, T. (2005). N^1-Aminopropylagmatine: A new polyamine produced as a key intermediate in polyamine biosynthesis of an extreme thermophile, *Thermus thermophilus*. J Biol Chem *280*, 30073-30082.

Otwinowski, Z., and Minor, W. (1997). Processing of X-ray diffraction data collected in oscillation mode. Macromolecular Crystallography, Pt A *276*, 307-326.

Park, M.H., Lee, Y.B., and Joe, Y.A. (1997). Hypusine is essential for eukaryotic cell proliferation. Biological Signals *6*, 115-123.

Park, M.H., Nishimura, K., Zanelli, C.F., and Valentini, S.R. (2010). Functional significance of eIF5A and its hypusine modification in eukaryotes. Amino Acids *in press*.

van Brummelen, A.C., Olszewski, K.L., Wilinski, D., Llinas, M., Louw, A.I., and Birkholtz, L.M. (2008). Co-inhibition of *Plasmodium falciparum S*-adenosylmethionine decarboxylase/ornithine decarboxylase reveals perturbation-specific compensatory mechanisms by transcriptome, proteome and metabolome analyses. J Biol Chem *7*, 4635-4646.

Wiest, L., and Pegg, A.E. (1998). Assay of spermidine and spermine synthase. In Methods in Molecular Biology 79 Polyamine Protocols, D.M.L. Morgan, ed. (Totowa, New Jersey, Humana Press), pp. 51-58.

Wu, H., Min, J., Ikeguchi, Y., Zeng, H., Dong, A., Loppnau, P., Pegg, A.E., and Plotnikov, A.N. (2007a). Structure and Mechanism of Spermidine Synthases. Biochemistry *46*, 8331-8339.

Wu, H., Min, J., Ikeguchi, Y., Zeng, H., Dong, A., Loppnau, P., Pegg, A.E., and Plotnikov, A.N. (2007b). Structure and mechanism of spermidine synthases. Biochemistry *46*, 8331-8339.

Wu, H., Min, J., Zeng, H., McCloskey, D.E., Ikeguchi, Y., Loppnau, P., Michael, A.J., Pegg, A.E., and Plotnikov, A.N. (2008). Crystal structure of human spermine synthase: implications of substrate binding and catalytic mechanism. J Biol Chem *283*, 16135-16146.